BEAM-BEAM COUNTERS AND CHARGED PARTICLE MULTIPLICITY IN THE BRAHMS EXPERIMENT AT RHIC

By

Yury Blyakhman

A dissertation submitted in partial fulfillment
of the requirements for the degree of
Doctor of Philosophy
Department of Physics
New York University
May, 2001

Dissertation Advisor

© Yury Blyakhman

All Rights Reserved, 2001

"The April Thesis."

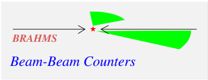

DEDICATION

To my girls. Анечке и Данечке посвящается.

ACKNOWLEDGMENT

This thesis results from the collaborative effort of a large group of people, all of whom contributed to its completion in many different ways. It is time to name them all.

I would like to thank my advisor, Burton Budick, who first introduced me to the field of the experimental high energy physics in general, and relativistic heavy ion collisions in particular. It was his knowledge, advice and encouragement, that made this work possible. I feel very fortunate to have worked with him during the last four years.

Certainly this thesis would not have been possible without the endless and generous help of the BRAHMS spokesperson Flemming Videbæk. He amazingly never ran out of patience, answering zillions of my "small questions". My great thanks to the Heavy Ion Research Group leader, Chellis Chasman for always trying to help and to provide me with at least two possible solutions to any big problem, or even small trouble, I had in my research. I would like to thank Dana Beavis, J.H.Lee and Ramiro Debbe for many fruitful discussions. It was great to work with and near them. My thanks to Betty McBreen and Konstantin Olchansky for helping me with my different computer needs and answering endless number of my questions. I would like to thank all members of the BRAHMS collaboration, not only for their great work, which made possible this thesis, but for supporting me in my research as well. Thanks to Ian Bearden, Jens Jørgen Gaardhøje, Kris Hagel, Y.K. Lee, Michael Murray, Fouad Rami, Steve Sanders and many others.

Over the last few years at BNL I was sharing my office with Hiro Ito. We had some good discussions, which helped me in my work. And for the last six years I was sharing my NYU office with my good friend Dmitry Rakhlin. Our talks and jokes helped me a lot to finally get to my Ph.D. degree.

I will always be grateful to my parents and my sister who supported me from the other side of the ocean throughout all these years of my studies. It meant a lot to me and my home will always be there.

It is a general rule to save the best for last, so I would like to thank my wife Anna and my daughter, "The Little Beauty", Daniella for their support and endless patience. They have accepted very stoically all these last seven years of me being a "permanent student". There are no words to express all my love and appreciation.

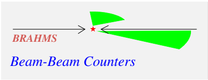

PREFACE

The Relativistic Heavy Ion Collisions are considered to be the only method to condense and to heat up a nuclear matter in the laboratory conditions. Regular nuclear matter consists of quarks and gluons, confined to each other inside hadrons (protons and neutrons) by the Strong Nuclear Force. It is believed, that high temperature and/or high density can break this confinement and cause a phase transition into a new form of matter, called the Quark Gluon Plasma (QGP). This new matter is of the great interest, since it is believed to have existed for the few microseconds after the Big Bang.

The Relativistic Heavy Ion Collider (RHIC), presently operating at the Brookhaven National Lab, is trying to observe the creation of the QGP in the collisions of two beams of gold nuclei, colliding with energies of $100A\ GeV$. BRAHMS is one of the four detectors, operating at RHIC and trying to explore such a phenomenon. The Beam-Beam Counters is one of the global detectors at BRAHMS and are designed to characterize collisions from the global perspective; to form a level0 trigger and to identify the space-time location of the collision vertex. The Beam-Beam Counters are a set of Cherenkov radiators attached to fast photomultiplier tubes. They are designed to detect charged particles, and, thus, to characterize the collision through the charged particle production.

The Beam-Beam Counters design and operation will be discussed here along with the charged particle multiplicity in the relativistic heavy ion collisions at RHIC.

TABLE OF CONTENTS

LIST OF FIGURES

LIST OF TABLES

LIST OF APPENDICES

ABBREVIATIONS

ADC:	Analog to Digital Converter
AGS:	Alternating Gradient Synchrotron
BBC:	Beam-Beam Counters
BFS:	Back Forward Spectrometer
BRAHMS:	Broad RAnge Hadron Magnetic Spectrometer
CAMAC:	Computer Automated Measurement And Control
CERN:	European Organization for Nuclear Research (Switzerland)
CFD:	Constant Fraction Discriminator
DAQ:	Data Acquisition System
FEH:	Fast Electronics Hut
FFS:	Front Forward Spectrometer
GEANT:	GEometry ANd Tracking
HIJING:	Heavy Ion Jet INteraction Generator
IR:	Interaction Region
LA:	Left Array
LHC:	Large Hadron Collider (project at CERN)
LED:	Light Emmiting Diode
MALU:	MAjority Logic Unit
MIP:	Minimum Ionizing Particle
PHENIX:	Pioneering High Energy Nuclear Interaction Experiment
PID:	Particle IDentification
pQCD:	perturbative Quantum Chromo-Dynamics
QCD:	Quantum Chromo-Dynamics
QGP:	Quark-Gluon Plasma
RA:	Right Array
RHIC:	Relativistic Heavy Ion Collider
RICH:	Ring Imaging Cherenkov Detector
STAR:	Solenoidal Tracker At RHIC
TDC:	Time to Digital Converter
TOFW:	Time-Of-Flight Wall
TPC:	Time Projecting Chamber
UVT:	Ultra-Violet Transmitting
ZDC:	Zero Degree Calorimeter

CHAPTER 1

INTRODUCTION

"By the summer of 1987, we should have the first solid data on ... the quark-gluon plasma (QGP)".

L.Van Hove [1]

The physics of Relativistic Heavy-Ion Collisions can be considered as one of the youngest areas in Modern Physics. Research in this area combines and brings together aspects of several different fields, such as:

- Nuclear Physics;
- Particle Physics;
- High Energy Physics;
- Thermodynamics;
- Hydrodynamics;
- Statistical Physics and
- Plasma Physics.

Starting from the late 1970s nuclear physicists began converting several existing accelerators for use with colliding heavy ions. The reason for that was straightforward:

Relativistic Heavy Ion collisions are the only means to compress and heat up nuclear matter in the laboratory.

Compressing the matter by $5-20$ times, or increasing its energy density up to a few GeV/fm^3 should be sufficient for the phase transition from the ordinary nuclear matter into the new form, which is believed to have existed a few microseconds after the Big Bang. This new form is usually called the Quark-Gluon Plasma (QGP). The requirements on the temperature and the density of the nuclear matter for the QGP creation are shown in **Fig. 1.1**.

The Relativistic Heavy Ion Collider (RHIC) presently operating at Brookhaven National Laboratory (BNL) is designed to collide beams of heavy ions with energies

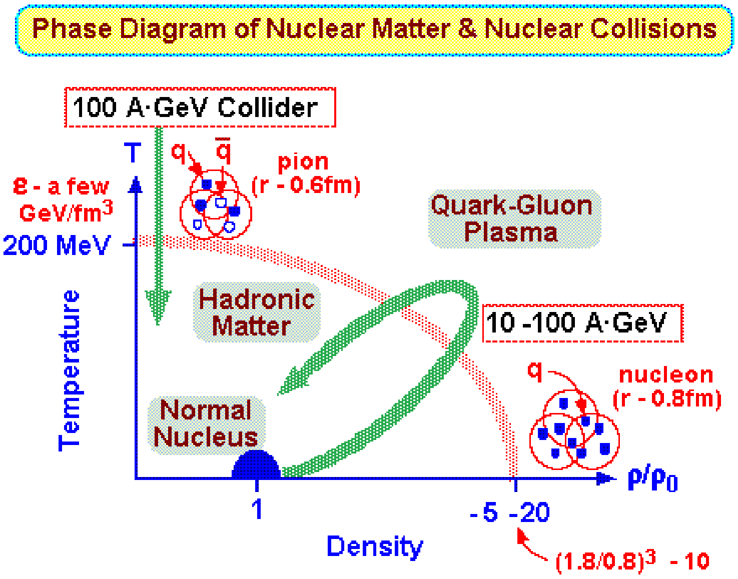

Figure 1.1: Phase diagram of hadronic matter.

of about $100 GeV-per-nucleon$ in order to try to recreate the QGP in the lab. The Broad RAnge Hadron Magnetic Spectrometer (BRAHMS) is one of the detectors searching for this new form of matter consisting of a deconfined soup of elementary bricks of nature: quarks and gluons.

In the next 3 sections of this chapter I will give a very brief introduction to the idea of the quark-gluon plasma, define kinematic variables central to my analysis and describe the main goals of this thesis in regard to the detection of the QGP.

1.1 New Phase of Matter.

Quantum ChromoDynamics (QCD) describes hadrons as particles built from groups of quarks (2 or 3) confined together with the help of gluons[1]. However, it is believed, that by heating and compressing nuclear matter through collisions at high energies, it is possible to break this confinement and to cause a phase transition from normal nuclear matter to the quark-gluon plasma. This state of matter is still not understood completely, but one scenario is believed to occur: quarks and gluons will no longer be confined, but will be free to move throughout the excited volume. Matter is believed to have existed in this form for the few microseconds after the Big Bang, so the main question now is whether this state can be created and detected in the laboratory.

RHIC energies of $100A\ GeV$ bring it into the region of "*ultra-relativistic heavy ion reactions*" by some classifications [2]. The most optimistic theoretical estimates

[1] A brief introduction to the presently known elementary particles and interactions between them can be found in **Appendix A**

expect QGP to form at about $10A\ GeV$. Two alternative possible collision regions are expected to be formed at these energies:

- "*Stopping region*" where baryons originally contained in the projectile and the target are fully or partially stopped by each other, forming a baryon rich matter in the middle of the reaction zone, and

- "*Transparent region*" where initial target and projectile baryons are far apart in the phase space and can not be slowed down completely by the collision process. The two colliding nuclei lose about half of their energies. This lost energy is deposited in the vicinity of the center of mass and is carried away mainly by pions. Collisions are inelastic and energy deposition is linearly dependent on the number of colliding nuclei. This explains the use of heavy ions.

The latter scenario of high energy density and low baryon density is of greater interest since it corresponds more closely to the situation in the early universe before hadrons were formed.

In a strongly interacting system of quarks and gluons, the system's configuration can be described by quark and gluon fields at all space-time points. A nice description of such a system can be given by the *space-time lattice* concept [3]. A set of quark fields is considered to be located at the lattice sites with gluon fields existing on the links between lattice sites. The gluon field is usually substituted for by a function of it, the so called "*link variable*", which describes the gluon field at the link of the lattice. The energy of such a system is minimized when the four link variables in a square of the lattice are correlated in the abstract color space, associated with the quark and gluon fields. Entropy, on the other hand, has a tendency to disrupt this correlation due to the thermal motion.

At low temperature the tendency of the link variables to correlate overwhelms the disruption due to the entropy. Because of that, interaction between quark and antiquark turns out to be attractive and thus the quarks are confined and the system is a condensate of quarks, antiquarks and gluons. Increasing the temperature may disrupt correlations very much and the ground state of the system will restore itself to the state of the deconfined quarks and gluons. A Quark-Gluon Plasma may be formed.

This formation process in a relativistic heavy ion collision can be described in the following stages:

1. Interpenetration of the colliding nuclei.
2. Formation of a hot and dense phase of the quark-gluon plasma.
3. Expansion of a hot hadron gas phase, formed by cooling and condensing of the initial phase.
4. Cessation of hadron scattering, because gas is cool and dilute enough, that hadrons no longer collide with each other.
5. "*Sweet Phase*": hadrons reach the detectors [4].

Many different models were created over the last 20 years to describe the scenario of such processes and their outcome. **Sec. 2.2** will be devoted to the brief description and comparison of several models.

For our immediate purposes we have to note, that during the Summer'2000 RHIC was not yet operating at its design energies and was colliding two beams of Gold (Au) nuclei each with an energy $\mathcal{E} = 65A\ GeV$. One of the most important properties of such a collision, as will be shown later in this text, is that the probability for the colliding nuclei to lose some reasonable fraction of their energy is rather large. Since most of this lost energy is used in particle production, it should be possible to characterize a collision by the production of particles. That is where the Beam-Beam Counters, as the main object of this thesis, are expected to play an important role.

1.2 Kinematic Variables.

Here I shall introduce kinematic variables, which are used to describe relativistic heavy-ion collisions, as well as many other high-energy reactions. These variables are very convenient for their simple Lorentz transformation properties and are used in our analysis.

$\{t, x, y, z\}$ – space-time coordinates of a point x: $x^{\mu} = \{x^o, x^1, x^2, x^3\} = \{t, \vec{x}\}$;

p_t and p_z – momentum components: $p^{\mu} = (p^o, \vec{p}) = (\mathcal{E}, \vec{p}_t, p_z)$

s – center-of-mass energy squared;

y – rapidity variable;

η – pseudorapidity variable,

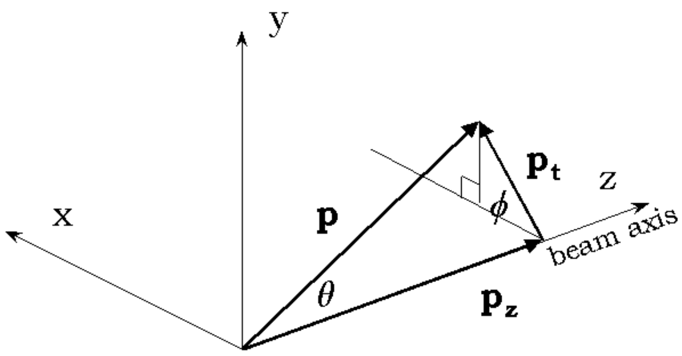

Figure 1.2: Coordinate system definition.

Direction along the incident beam is usually designated as a z (longitudinal) axis, as in **Fig. 1.2**. And, as usual, covariant vector x_μ is related to the contravariant vector x^μ as

$$x_\mu = g_{\mu\nu} x^\mu = (t, -x, -y, -z)$$

with the space-time metric tensor $g_{\mu\nu}$ in the form [5]

$$g_{\mu\nu} = \begin{pmatrix} 1 & 0 & 0 & 0 \\ 0 & -1 & 0 & 0 \\ 0 & 0 & -1 & 0 \\ 0 & 0 & 0 & -1 \end{pmatrix}$$

In high–energy processes with the production of a huge number of particles, it is very complicated to follow the event completely, so it's best to focus one's attention only on one particle and consider the rest of them as a bulk mass. Such a reaction could be taken as: $B + A \Longrightarrow C + anything$ and is called "*inclusive reaction*". Here A and B would be the colliding particles, and C - detected particle. Then for the center of mass energy squared s one can write:

$$s = (p_A + p_B)^2 = 2E_{CM}^2, \qquad \begin{cases} p_A = (\mathcal{E}, -\vec{p}) \\ p_B = (\mathcal{E}, \vec{p}) \end{cases} \Longrightarrow \sqrt{s} = 2\mathcal{E},$$

So, if RHIC has two colliding beams, each with $\mathcal{E} = 65A\ GeV$, that would make $\sqrt{s} = 130A\ GeV$, or $\sqrt{s_{NN}} = 130GeV$.

Rapidity.

The physical meaning of the rapidity variable can be described as follows [6]: if one can find a reference system moving with the z axis parallel to p_z in which C has only transverse momentum, then, in terms of energy-momentum components p_o and p_z (see above), the rapidity of a particle will be defined as

$$y = \frac{1}{2} \ln \left(\frac{p_o + p_z}{p_o - p_z} \right). \tag{1.1}$$

After some simple math, one can relate the energy of the particle p_o and it's longitudinal momentum p_z with rapidity:

$$p_o = m_t \cosh y \tag{1.2}$$

$$p_z = m_t \sinh y, \tag{1.3}$$

where m_t is a *transverse mass* of C:

$$m_t^2 = m_o^2 + \vec{p}_t^{\,2}, \tag{1.4}$$

m_o is the rest mass of the particle.

Let me show why the rapidity is considered to be such a good kinematic variable in high-energy physics. For a particle moving with velocity β in the positive z direction one can write (assuming, as usual, units with $\hbar = c = 1$):

$$\left.\begin{array}{l} p_z = \gamma\beta m_o \\ \\ p_o = \gamma m_o \end{array}\right\} \Longrightarrow \; y_\beta = \frac{1}{2}\ln\left(\frac{1+\beta}{1-\beta}\right),$$

where y_β is a rapidity of a particle traveling with a velocity β in the positive z direction. Or just

$$y_\beta = \tanh^{-1}\beta \tag{1.5}$$

Fig. 1.3 shows the graph of rapidity *vs.* β. This rapidity is independent of the mass of the particle and for non-relativistic cases of small β we shall have

$$y_\beta = \beta + O(\beta^3) \text{ – longitudinal velocity of a particle.}$$

Now let's find the relation between the rapidity y of a particle in a laboratory frame $\mathcal{K}$ and the rapidity y' in a moving frame $\mathcal{K}'$, which moves with velocity β

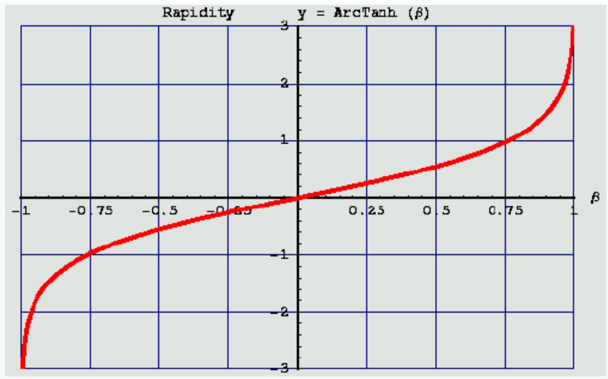

Figure 1.3: Rapidity y as a function of particle's β.

with respect to $\mathcal{K}$.

$$\left.\begin{aligned} y' &= \tfrac{1}{2}\ln\left(\tfrac{p'_o+p'_z}{p'_o-p'_z}\right) \\ p'_o &= \gamma(p_o-\beta p_z) \\ p'_z &= \gamma(p_z-\beta p_o) \end{aligned}\right\} \Longrightarrow y' = \frac{1}{2}\ln\left[\frac{\gamma(1-\beta)(p_o+p_z)}{\gamma(1+\beta)(p_o-p_z)}\right] \equiv y - y_\beta. \tag{1.6}$$

We just showed, that under a Lorenz transformation the rapidity of the particle in a moving and in the lab frames of references are related through simple addition or subtraction. That is why the rapidity of a particle is often treated as a relativistic measure of the particle's velocity.

Pseudorapidity.

As one can see, rapidity is a useful variable, but it is necessary to know both energy and longitudinal momentum of a particle, in order to find it. At the same time, the easiest thing to measure in many experiments would be the angle of the

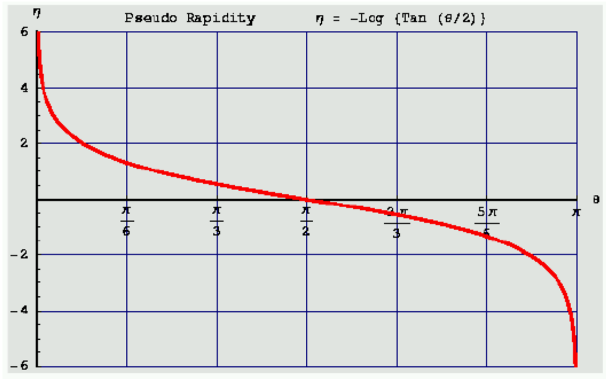

Figure 1.4: Pseudorapidity η as a function of angle θ.

detected particle relative to the beam axis. In this case it is much more convenient to use the "*pseudorapidity*" variable η to characterize the detected particle. It is defined as:

$$\eta = -\log \tan \left(\frac{\theta}{2}\right), \tag{1.7}$$

where θ is the angle between the particle momentum $\vec{p}$ and the beam axis. **Fig. 1.4** shows the graph of pseudorapidity *vs.* angle θ

In terms of momentum the pseudorapidity is:

$$\eta = \frac{1}{2} \ln \left(\frac{|\vec{p}| + p_z}{|\vec{p}| - p_z}\right). \tag{1.8}$$

and again, one can easily get the following:

$$
\begin{aligned}
|\vec{p}| &= p_t \cosh \eta \\
p_z &= p_t \sinh \eta
\end{aligned}
$$

One can easily see, that for the case of large momentum, when $|\vec{p}| \simeq p_o$ the pseudo-rapidity coincides with rapidity variable.

1.3 BRAHMS experiment at RHIC.

One of the purposes of the Relativistic Heavy Ion Collider at Brookhaven National Laboratory is to try and observe the creation of the quark-gluon plasma in the collisions of two beams of gold nuclei, colliding with the energies up to and including $100A\ GeV$. The Broad RAnge Hadron Magnetic Spectrometer (BRAHMS) is one of the detectors to explore such phenomena.

BRAHMS is designed to characterize collisions with a wide range of rapidity and transverse momentum [7]. Here, at BRAHMS, we will try to investigate the QGP phase transition through study of the transverse momentum $< p_t >$ dependence on centrality, and the strange particle production via K^+ and K^- in different reaction regions. These goals are achieved by operating in the pseudorapidity interval $0 \leq \eta \leq 4$, or $2^o \leq \theta_{lab} \leq 90^o$. Different experimental conditions lead to the construction of two different spectrometers: a Forward Spectrometer and a Midrapidity Spectrometer. **Sec. 3.2** will have a detailed description of the BRAHMS experiment at RHIC.

The Beam-Beam Counters are a set of detectors designed to characterize relativistic heavy ion collisions at BRAHMS from a global perspective. I will show in this thesis how the design of the Beam-Beam Counters enables us to probe the nature of the relativistic heavy ion collision, and to look for some signatures of the quark-gluon plasma formation.

Another very important purpose of the Beam-Beam Counters is to provide a level0 trigger, or a `START` signal for the experiment. Technical details of the Beam-Beam Counters functioning in this manner will be discussed in the experimental section of this thesis. It will include the description of the design, initial computer simulation and later performance and data acquisition of the Beam-Beam Counters as one of the global detectors in the BRAHMS experiment at RHIC.

1.4 Thesis Goals.

As mentioned above, it should be possible to characterize high energy heavy ion collisions through the particles' production mechanism. Among different signatures of the quark-gluon plasma formation, only two (related to the charged particles production) are of the most direct interest to us here:

- The value of the energy density in the collision region and
- Total number of charged particles produced in a collision.

It will be shown how a shape of the charged particle's space density distribution, as measured by our detector, has a direct relation to the total number of charged particles produced and thus to a possible formation of the QGP. It was experimentally shown in reference [8], that in nucleon-nucleon collisions about $80-90\%$ of the produced particles are pions; the rest are primarily kaons.

> *Multiplicity of the collision* : total number of particles, produced in a collision.

Since most of the detection methods are only sensitive to the ionizing particles, it makes more sense to talk about the total number of charged particles, produced in a collision, or *charged multiplicity*. The produced particles have a distribution in their momentum. This means, that the longitudinal momentum distribution of the particles can be linked to their rapidity distribution y. For highly energetic particles their rapidity distribution is almost identical to their pseudorapidity distribution η, as was shown in the previous section. But we are required to measure only one kinematic variable of a particle (say, angle θ) in order to get it's pseudorapidity value, compared to two required variables for the rapidity. For this reason in most high-energy experiments the pseudorapidity of the particle is the measured quantity and collisions are characterized by the particle's pseudorapidity distribution. BRAHMS is not an exception in this matter.

Certain unique properties of the Beam-Beam Counters allow them to measure the charged multiplicities over a quite wide range of pseudorapidity. Their physical characteristics restrict the solid angle coverage to $1^o \leq \theta \leq 7^o$, but the wide range of the collision vertices allowed us to extend the pseudorapidity coverage to the range $1.85 \leq |\eta| \leq 4.70$. This places the Beam-Beam Counters in a unique position, as the only Cherenkov counters in all the RHIC experiments, covering this particular pseudorapidity range.

In this manner,

- The charged particle multiplicity *vs.* pseudorapidity ($dN_{ch}/d\eta$ *vs.* η) distribution, measured by our detector will be linked to the number of the produced charged particles per one nucleon participating in the collision.
- This distribution will be compared to the different theoretical models of the relativistic heavy ion collisions.
- Different centrality cuts (impact parameter of the collision) will be considered.
- It will be shown how the Beam-Beam Counters served as a level 0 trigger for the whole BRAHMS experiment.
- It will be demonstrated, how the space-time location of the collision vertex can be determined by the Beam-Beam Counters with the designed precision.
- And how the collision instant t_o is used by the BRAHMS time-of-flight detectors for the particle identification.

CHAPTER 2
CHARGED PARTICLES PRODUCTION

"*The origin of the universe:*
First, there was nothing. Then it exploded".
/Bumper sticker/

And we have done it again!

Without properly resolving one of the biggest *idée fixe* of alchemy and of mankind in general, namely, the discovery of the "Philosopher's Stone" to turn things into gold, scientists are now on another quest. What people are currently trying to do can be called "*Anti-Alchemy*"

> **Anti-Alchemy** : the science to transform Gold into something completely new, colorful, strange and charming, topless and bottomless, completely unknown and practically useless, named the Quark-Gluon Plasma (partially from [9]).

So, let me follow this trend and in the first section of this chapter I will try to give an overview of the theoretical approaches and the expectations of the Quark-Gluon Plasma phase transition. I will discuss the background of the subject and will try to show the development of one of the QGP global signatures, namely charged particle distributions. This signature is most closely related to the subject of my thesis.

The next section I will dedicate to the comparison of different scenarios of the phase transition, which leads to different structures for the charged particle distributions. I will show the Beam-Beam Counters simulated response to different models and use it later, in **Ch. 6** for comparison with our experimental result.

A general overview of the experimental history of heavy-ion physics is beyond the scope of this thesis. The field is too vast, so in the last section of this chapter I will only show some of the RHIC results, which are of direct relevance to the topic of this thesis. As of April 2001, there are only three published papers ([10], [11] and [12]) from other RHIC experiments PHOBOS, STAR and PHENIX, based on the results of the Summer' 2000 run.

2.1 Quark-Gluon Plasma.

In this section I would like to discuss some general aspects of the QGP formation in relation to the topic of this thesis. I will give several brief definitions and say a few words about the phase transitions in relativistic heavy-ion collisions in particular.

2.1.1 Main aspects.

"*Quantum Chromodynamics*" (QCD) is a gauge theory, which describes strongly interacting matter through the interaction of quarks by exchange of the gluons [13]. This theory gives us a few interesting results. Namely,

1. For *short distances* or *large momenta* q, the effective coupling constant $\alpha_s(q^2)$ decreases logarithmically. which means, that quarks and gluons are weakly

coupled;

2. For *large distances* or *small momenta* the effective coupling becomes strong. This gives us:

   quark confinement : quarks do not occur isolated in nature, but only in hadronic bound states creating mesons or baryons

   and

   chiral symmetry breaking : quarks confined in hadrons demonstrate dynamically generated masses sometimes of several hundreds MeV.

3. For low energies, the QCD vacuum is characterized by nonzero expectation values of certain operators, which describe nonperturbative physical properties of the QCD vacuum.

As the temperature goes up, the interactions between quarks occur closer and closer to each other, while the long range interactions become dynamically screened. It was shown, that $\alpha_s(T)$ falls logarithmically with increasing temperature [14]. It follows, that at high temperature nuclear matter will show neither confinement, nor symmetry breaking.

Another good model describing quark confinement is called the "*Bag Model*" and essentially treats quarks as massless particles inside a bag of a finite dimension [15]. Confinement in this model is achieved by balancing the inward directed "*bag* *pressure*" B with the stress from the kinetic energy of the quarks. Gauss's Law and gluon confinement within the bag makes the matter inside the bag colorless. With the increase of the inside pressure, the bag pressure gives way and confinement ends with the creation of a new phase of matter of free quarks and gluons.

How can one increase the kinetic energy inside?

1. Increase the temperature, as was mentioned earlier, or

2. Increase the baryon number density within the bag

2.1.2 QGP in Relativistic Heavy Ion Collisions.

Every word in this heading implies increasing particles' density, temperature and energy in general in a very small region of space, hence, trying to create the quark-gluon plasma. Colliding nuclear matter loses about 1/2 of it's energy in the collision process. This energy is deposited in the vicinity of the center of mass providing a region with very high energy density which is directly related to QGP formation. **Fig. 2.1**. shows center-of-mass frame characterization of the head-on

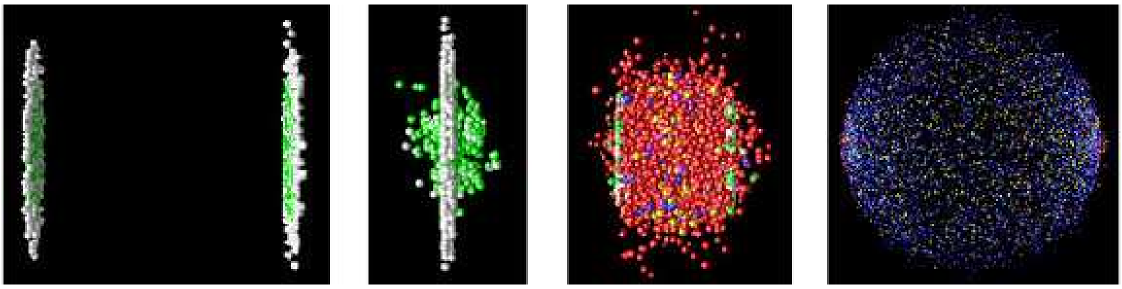

Figure 2.1: General view of the collision.

collision of two equal nuclei, where they can be described by the collision of two thin Lorentz contracted disks.

Two possible collision scenarios are available (regions created in these collisions were mentioned in **Sec 1.1**):

1. **Full Stopping**, as described on **Fig. 2.2**:
   - Happens for collisions at $\sqrt{s} \simeq 10A\ GeV$.
   - Is described by, so called, Landau model.
   - Baryons, freed from the colliding nuclei are completely stopped by each other, forming a baryon-rich region in the middle:

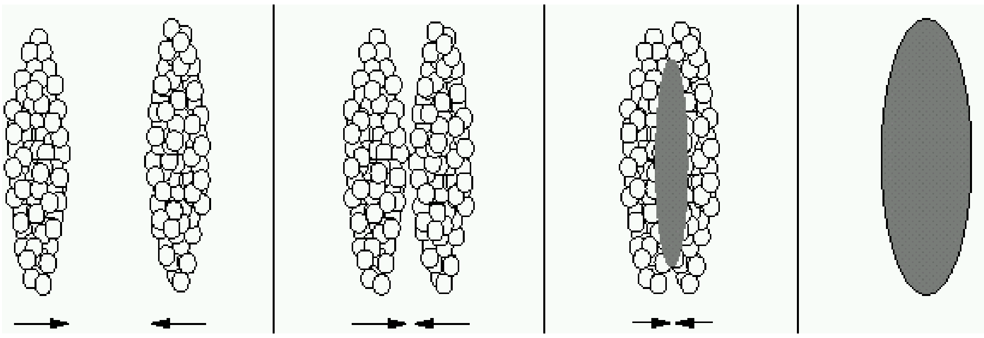

Figure 2.2: Full Stopping in the collision by Landau.

2. **Transparency**, as described on **Fig. 2.3**:
   - Happens for collisions at $\sqrt{s} \geq 100A\ GeV$.
   - Is described by, so called, Bjorken model.
   - Baryons, freed from the colliding nuclei fly through each other, losing some energy, forming a baryon-free region in the middle.

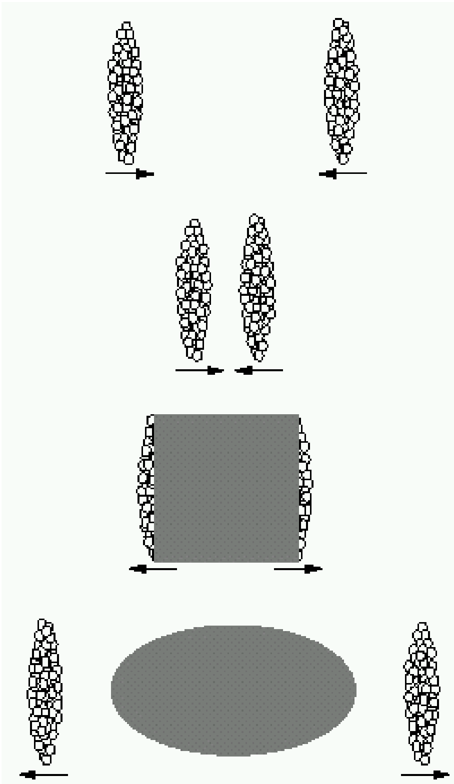

Figure 2.3: Transparency in the collision by Bjorken.

For example, at RHIC a central $^{197}A +^{197}A$ collision with CM energy $\sqrt{s} = 200A\ GeV$ will give a total energy $E_{tot} = 40TeV$. This value implies an initial energy density at the moment of maximum nuclear overlap of the order of $\varepsilon \simeq 250GeV/fm^3$. Comparing that with the widely accepted deconfinement energy range of $\varepsilon_{crit} = 1 - 10GeV/fm^3$, one can see these kind of collisions being in the pure QGP phase. The energy loss is accompanied by the production of a large number of particles (mostly pions, because of the baryon-free area in the middle). Thus, the number of particles produced is directly related to the amount of energy

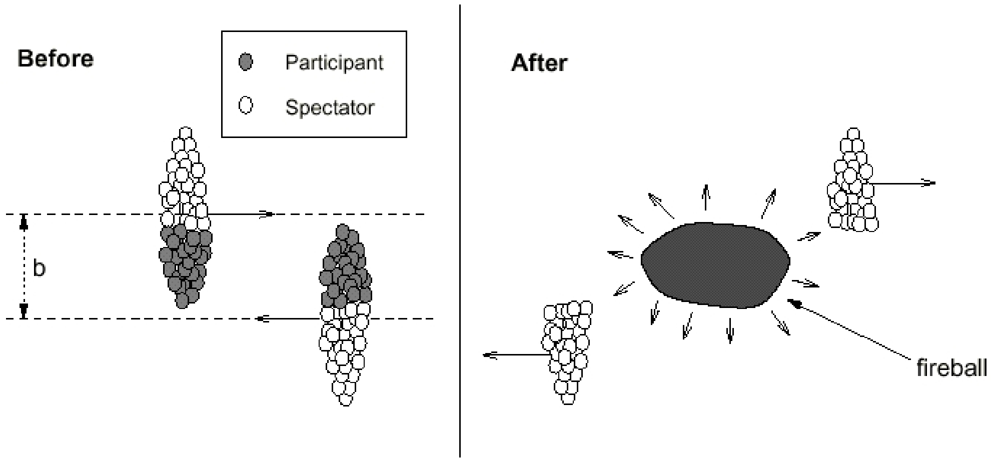

Figure 2.4: The participant-spectator approach to the heavy-ion collisions.

deposited in the vicinity of the center of mass. The Beam-Beam Counters, again, are designed to register charged particles, so, hopefully should be able to give some hints about the QGP phase transition.

The, so called, "*participant-spectator*" model describes heavy-ion collisions using the distance between paths of the two colliding nuclei, the impact parameter b, as a definition of a separation distance between not-interacting parts of the nuclei, as shown on **Fig. 2.4**. During the collision, only the participants interact, while the spectators keep flying in the original direction.

The space-time scenario of these events could be described as illustrated on **Fig. 2.5** [5]. Some definitions first. Any reaction of a kind $A + B = C + X$ where we are interested in the production of C, can take place with the scattering of the constituent b of B and a of A. The constituents a and b are called "*partons*". So,

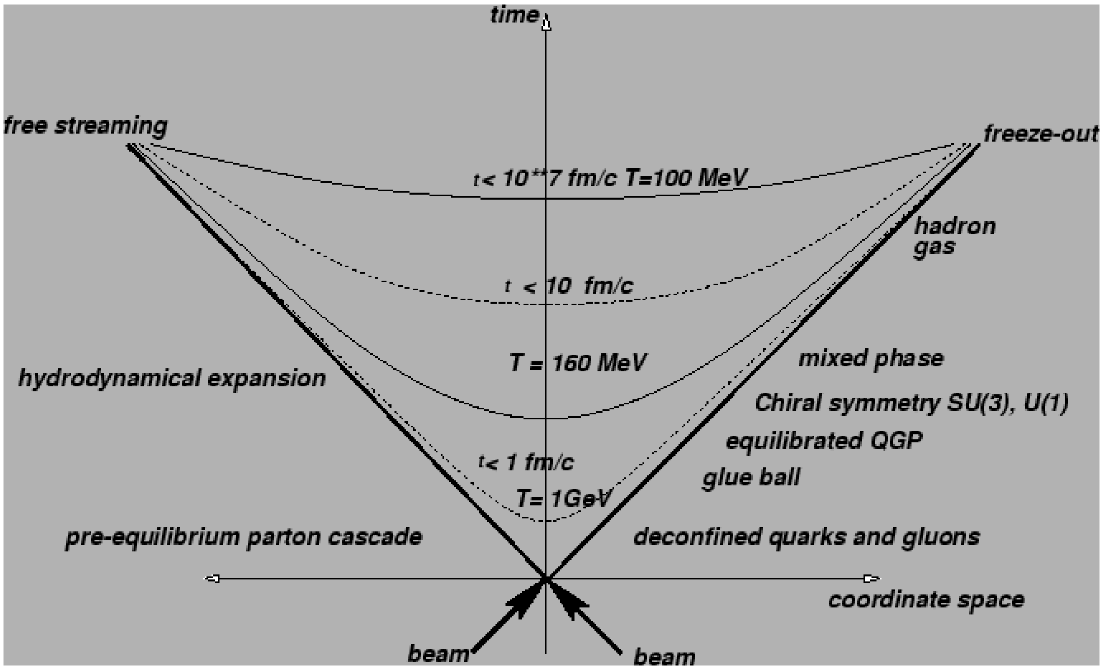

Figure 2.5: The space-time picture of a nucleus-nucleus collision [5].

after the first instant of nuclear contact, the partons of the colliding nuclei will begin to interact with each other in the region between the two receding disks [16]. The excited partons rescatter and emit new particles evolving towards a thermalized quark-gluon plasma state. Initially, the plasma may not be in thermal equilibrium, but subsequent equilibration should bring it there at $t \sim 1 fm/c$. After that we expect plasma to behave according to the laws of hydrodynamics. Plasma expands, its temperature goes down and hadronization starts to occur with lots of hadrons streaming out of the collision region. Thus, the energy deposited in the collision region will manifest itself in the form of produced hadrons, which means that this energy can be estimated through the hadrons' characteristics.

2.1.3 Formation signatures.

Identifying the formation of the quark-gluon plasma is one of the major goals of all RHIC experiments. Ideally, we must show that some features of the data cannot be present without a quark-gluon plasma. There exist many different signatures and observables of its formation. Let me summarize some of them in **Table 2.1** [4]. Searching for many of them is an objective of all RHIC experiments. Charged particle distributions resulting from the collision can serve as another characteristic of possible QGP formation.

The best quantity to describe the produced particles could be their *rapidity distribution* or *rapidity density*, dN/dy as a function of the particle's rapidity y, where N is a number of produced charged particles. Using definitions of **Sec. 1.2**

Signature	Process Probed	Experimental Observable
Charm enhancement	Charm and anti-charm quarks creation due to the high energy	Energetic single and pair of leptons
Suppression of J/ψ	Screening of charm-anticharm pair interaction by the high number of the surrounding quarks	Decreased probability for J/ψ production
Strangeness enhancement	Production of additional strange quarks by the plasma	More mesons and baryons containing strange quarks
Jet energy loss	Nature of the matter encountered by a quark on its way out of the system	Fewer high-energy jets of particles
Fluctuations in hadron distributions	Bubbles of plasma	Structure in the spatial distribution of hadrons

Table 2.1: Predicted signatures of quark-gluon plasma formation.

with **Eq. (1.2)** and **Eq. (1.3)** for longitudinal momentum p_z and particle energy p_o, one can write the particle's velocity v_z as related to the particle's coordinate z and time t after flying out of the origin $(0, 0)$:

$$\frac{z}{t} = v_z = \frac{p_z}{p_o} = \tanh y$$

With proper time τ defined as

$$\tau = \sqrt{t^2 - z^2},$$

one can easily derive the following equations:

$$\begin{aligned} z &= \tau \sinh y \qquad (2.1) \\ t &= \tau \cosh y \\ y &= \frac{1}{2} \ln \frac{t+z}{t-z} \end{aligned}$$

Eq. (2.1) shows, that rapidity variable is related to the particle's spatial coordinate, which means, that the rapidity distribution dN/dy can be transcribed as a spatial distribution from which the initial energy can be derived.

dN_{ch}/dy at midrapidity.

Now let's consider a longitudinal element of length Δz at $z = 0$ as in the middle of the second picture in **Fig. 2.1**. The transverse overlapping area will be called $\mathcal{A}$, then number density in volume $\mathcal{A}\Delta z$ at $z = 0$ and $\tau = \tau_o$ (time of the QGP formation and equilibration) will be written as:

$$\begin{aligned} \frac{\Delta N}{\mathcal{A}\Delta z} = \frac{1}{\mathcal{A}}\frac{dN}{dy}\frac{dy}{dz}\bigg|_{y=0} &= \\ &= \frac{1}{\mathcal{A}}\frac{dN}{dy}\frac{1}{\tau_o \cosh y}\bigg|_{y=0} \end{aligned}$$

But the particle's energy is given by **Eq. (1.2)** as $m_T \cosh y$, thus the initial energy density would be:

$$\epsilon_o = m_T \cosh y \, \frac{\Delta N}{\mathcal{A}\Delta z}$$

After averaging over the area $\mathcal{A}$ and proper time τ_o it is:

$$\epsilon_o = \frac{m_T}{\tau_o \mathcal{A}}\frac{dN}{dy}\bigg|_{y=0} \tag{2.2}$$

This important result, which connects the initial energy density to the rapidity density and describes the relationship of my thesis to the discovery of the Quark-Gluon Plasma, was originally derived by Bjorken [17].

dN_{ch}/dy and entropy.

Another connection between the charged particle multiplicity and phase transition to the Quark-gluon Plasma was described in reference [18]. It discusses the possibility that transverse momentum p_t *vs.* n correlation could provide a signal for the deconfinement transition of hadronic matter. Here n is the multiplicity in the small rapidity region:

$$n = \int_{-yo}^{y_o} (dn/dy)\, dy$$

The results from the CERN $p\bar{p}$ collider are used as an example and reference [18] follows the general concepts of Landau's hydrodynamical model [19]. In this model dn/dy reflects the entropy and p_t spectrum reflects the temperature and the transverse expansion of the central region of the hadron matter. Most of the entropy is presumed to be created in the early thermalization stage of the collision.

The central multiplicity $n \sim \sigma V$, where V is the volume of the expanding hadron matter and σ its average entropy density. Larger n means larger σ and/or V at some fixed time instant, but in phase transition dn/dy increases while temperature remains constant. This leads to the flat region in the p_t *vs.* dn/dy distribution. The results from the $p\bar{p}$ collider show, that higher n indicates hotter hadronic matter. Thus, it is argued, that the anomaly in the p_t *vs.* dn/dy dependence may signal the phase transition to the QGP.

Figure 2.6 shows an example of the expected p_t *vs.* dn/dy dependence. This signature of the QGP formation is related to the charged particle multiplicity distribution and might be easier to measure in the experiment, than many other signals of the possible phase transition.

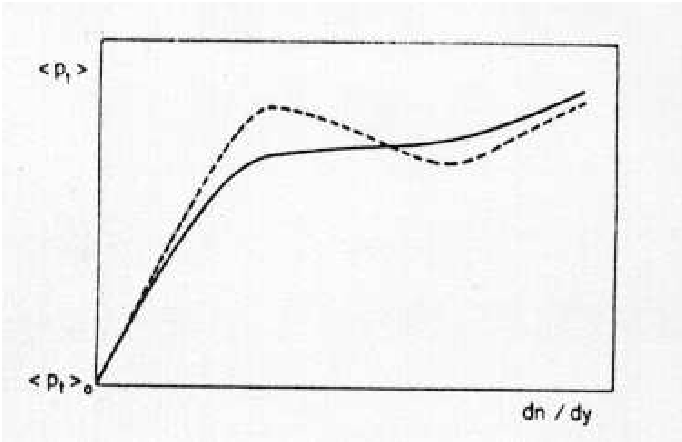

Figure 2.6: Expected structure in the $< p_t >$ *vs.* dn/dy correlation resulting from the QGP phase transition (solid line), and sharper structure expected for a given impact parameter (dashed line) [18].

Final remarks.

A few qualifications have to be made in this connection:

1. The Beam-Beam Counters can only detect charged particles, but with the assumption made in **Sec. 1.4**, that most of the hadrons produced are pions, and with another assumption of equal numbers of π^+, π^- and π^o being produced, we can conclude, that $dN/dy = (3/2)dN_{ch}/dy$.

2. **Sec. 1.2** mentioned, that in real experiments people measure pseudorapidity distributions, rather than rapidity, hence, we can convert $dN_{ch}/d\eta$ distribution, measured by the Beam-Beam Counters to the expected dN_{ch}/dy values, or just use the fact, that these distributions are almost identical in the high pseudorapidity regions ($|\eta| > 2.0$).

3. And the most important issue: all the derivations above concern the energy densities at midrapidity region ($y = 0$), but the Beam-Beam Counters range is far from the midrapidity. They measure $dN_{ch}/d\eta$ at $1.85 \leq |\eta| \leq 4.70$. How can we relate these measurements to the QGP formation? This will be accomplished through the various models of heavy ion collisions. Although their main point of interest is the value of $dN/dy|_{y=0}$, every model carries with it a distribution of $dN_{ch}/d\eta$ over the whole range of pseudorapidity η. In other words, knowing $dN_{ch}/d\eta$ distribution in any region contributes to the choice of the correct model and to an understanding of the mechanism of the phase transition.

Now, as we introduced some definitions and agreed on the possibility of the QGP creation in the relativistic heavy ion collisions, let me present a discussion of the different models, describing such a collision. All of these models attempt to pursue two major goals:

1. To describe all processes during a collision, and as a result,

2. To predict possible experimental results, so experimentalists know what are they looking for.

Thus, our next section describes several mechanisms of the charged particle production through the collision models.

2.2 Genesis Scenarios.

"*It is a capital mistake to theorize before one has data.*"

/A. Conan Doyle, Scandal in Bohemia/

A large number of different models and methods have been developed in order to recognize new physics due to the formation of the QGP in heavy ion collisions. So called "*event generators*", or "*Monte-Carlo codes*" (MC codes) have been introduced. These codes by definition provide randomly generated "events", characterized by a certain number of particles of different types with given momenta [20]. The reality is, that Monte-Carlo codes are absolutely necessary to understand experimental data and to provide a link, connecting these data to the theoretical model. The relation between the code and the model can be described as follows: the model is defined by a set of equations and the computer code serves as a technical means to solve these equations.

At the same time, one has to understand, that these equations, that form the basis of the MC code can never be derived from first principles. Rather an effective theory, based on the "true" theory will be used. All that plus the fact, that many aspects of multi-particle production are still not clear, results in these different event generators giving quite contradictory results. In this section I will cover briefly the main aspects of several models and show their predictions for the new phase formation and charged particle multiplicity distributions, as the QGP's signature which is of the most interest to us.

2.2.1 Terminology.

Qualitatively energy deposition and particle production mechanisms in ultrarelativistic heavy ion collisions can be divided in two categories as in [21] and references therein.

- "*Semihard*" particle production is based on perturbative QCD (pQCD). The semihard gluons, quarks and antiquarks are produced in parton-parton collisions and they have transverse momenta $p_t \geq p_o \sim 1 \ldots 3GeV$. The particles coming from these semihard partons are often referred to as "*minijets*".

- In the "*soft*" particle production region, below the momentum transfer scale $\sim 1 - 2GeV$ we can not rely on pQCD anymore and have to use different modeling for soft particle production. In heavy-ion collisions it can be done by several methods.

- Effect of quarks and antiquarks in the small y region is usually called "*nuclear shadowing effect*" based on the parton model.

- It is expected, that in high energy heavy ion collisions the region with high density will extend in the transverse region to a size, comparable to the size of the nucleus. This means, that transverse jets will have to travel through this region for some distance. "*Jet quenching*" may result from energy loss in this region, providing a good probe of the system's properties [22].

Unfortunately there does not exist a single formalism able to account for a complete nucleus-nucleus collision. The reaction has to be divided in different stages, as described in **Fig. 2.5**. Different event generators address different stages of the collision. Now let me describe the main models and event generators, which we used in our research as Monte-Carlo simulations.

2.2.2 FRITIOF7.02.

One of the oldest models still in vogue is called FRITIOF. It was first described in reference [23]. The bulk of the particles in this model are assumed to be produced at the low values of the transverse momentum p_t, thus strong interaction are non-perturbative and can not be understood in terms of QCD. A collision between two hadrons is modeled by many momentum transfers. After the momentum exchange, a hadron is treated as a longitudinally excited object, referred to as a string state, emitting gluonic radiation in a color dipole approach. In hadron-nucleus or nucleus-nucleus interactions each hadron can suffer several collisions with further excitation during each of them. The final hadronization happens independently along the special string fragmentation model. The hadronization takes place outside the nuclei and thus no internuclear cascading is considered. Collisions with nuclei are assumed to involve only independent collisions between the constituent nucleons, and there is no space-time dependence [24, 25].

Shown in **Fig. 2.7** are the $dN_{ch}/d\eta$ *vs.* η distributions calculated by the FRITIOF model in central ($b \leq 2fm$) and semi-peripheral ($4fm \leq b \leq 6fm$) $Au + Au$ collisions at Summer' 2000 RHIC energies of $\sqrt{s} = 130A\ GeV$.

We are in a little bit better position now, since it has been established, that FRITIOF7.02 event generator output in $dN_{ch}/d\eta$ spectrum has in it of the order of

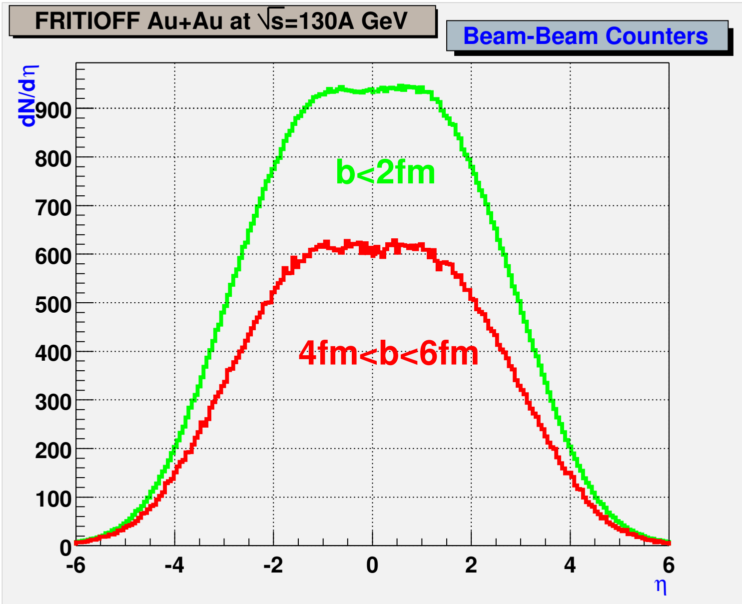

Figure 2.7: The prediction of the charged particles pseudorapidity distribution by the FRITIOF7.02 model at different impact parameters in the $Au + Au$ collisions at $\sqrt{s} = 130A\ GeV$.

twice the number charged particles generated in central collisions, than is believed should be there (predicted by the most event-generators below). But nevertheless it is still possible to use semi-peripheral ($4fm \leq b \leq 6fm$) collisions as a good approximation for the real-life central events.

2.2.3 HIJING.

HIJING : Heavy Ion Jet INteraction Generator.

Multiple minijet production becomes more important in the case of the relativistic heavy ion collisions. Particle production due to minijets had to be investigated in order to recognize new physics of quark-gluon plasma formation. The HIJING model incorporates pQCD approach to multiple jet processes. These processes are combined together with a FRITIOF-type model for soft interactions, described above. A special parameterized parton distribution function inside a nucleus had to be used to take into account parton shadowing. Jet quenching is incorporated in the model by an assumed energy loss dE/dz of partons traversing the produced dense matter. FRITIOF jet fragmentation model is used for the hadronization [26].

Reference [22] describes main features included in this model as follows:

1. Soft beam jets are modeled by diquark-quark strings with gluon kinks as in FRITIOF, discussed above. The collision is decomposed into binary collisions involving excited or "*wounded*" nucleons with a $q - q\bar{q}$ configuration, which slowly decays. The major difference here is, that subsequent collisions of partons are considered to be essentially different from the first one. They involve sea partons instead of the valence ones.

2. Multiple minijet production is included with enhancement of semihard and soft background.

3. Nuclear geometry is used to calculate the impact parameter dependence of different processes with introduction of the impact-parameter-dependent parton structure function.

4. In FRITIOF model multiple interactions can lead only to excitations of greater mass strings. HIJING allows for string-string interactions to deexcite as well

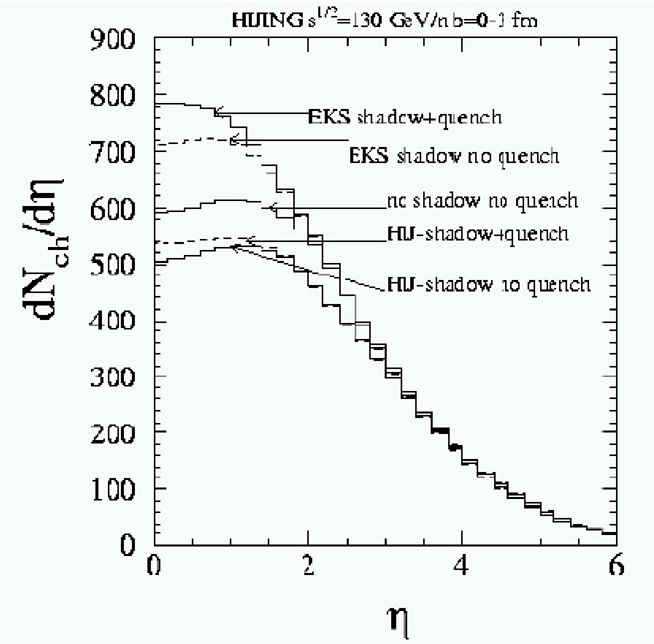

Figure 2.8: The prediction of the pseudorapidity distribution by different ingredients of the HIJING model for charged particles in central $Au + Au$ collisions at $\sqrt{s} = 130A\ GeV$ [27].

as excite further the strings within the kinematic limits [22].

Now, coming back, we are interested in a particular prediction of these models, namely, the pseudorapidity distributions of charged particles. Shown in **Fig. 2.8** are the $dN_{ch}/d\eta$ *vs.* η distributions calculated by the HIJING model in central $(b \leq 3\ fm)$ $Au + Au$ collisions at $\sqrt{s} = 130A\ GeV$ for different mechanisms of particle production included in the model.

As one can easily see, all these different mechanisms, produce large differences in the mid-rapidity region $(\eta \sim 0)$. We can spend a lot of time discussing influence of each of the assumptions of HIJING on different values of $dN_{ch}/d\eta|_{\eta=0}$, but fortu-

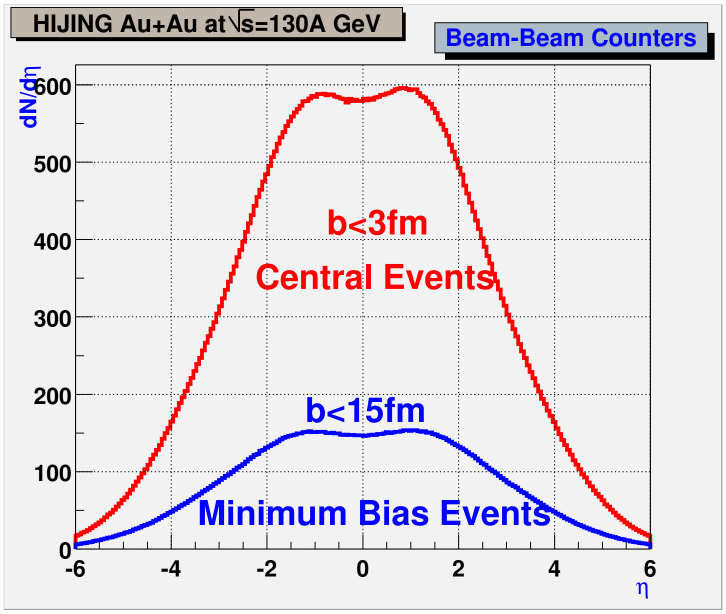

Figure 2.9: HIJING charged particles multiplicity distribution for central $Au+Au$ collisions at $\sqrt{s} = 130A\ GeV$. "Jet quenching" and "nuclear shadowing" is turned on.

nately, there is no significant difference in the Beam-Beam Counters coverage region of $1.85 \leq |\eta| \leq 4.70$. To summarize this section let me show **Fig. 2.9** with the final charged particle distribution, produced by the HIJING model for the case of "*Central*" ($b \leq 3fm$) and "*Minimum Bias*" ($b \leq 15fm$) events with "jet quenching" and "nuclear shadowing" turned on.

2.2.4 RQMD and others.

As it was mentioned earlier, we are in a good position here, having results at hand and knowing already which models are realistic and which are not. In this section I would like to do a very short overview of some other models which do not give as good a prediction for our case of high energy $Au + Au$ collisions.

RQMD.

RQMD : Relativistic Quantum Molecular Dynamics

The idea behind this model was to develop some scenario for transport in nucleus-nucleus reactions starting with the state before overlap to the final state with no more interactions (freeze-out) [28]. It uses a semiclassical microscopic approach and combines classical propagations with stochastic interactions. Elementary collisions excite strings and resonances into the fragmentation and decay with particle creation. Overlapping strings do not fragment independently, but form "*ropes*", chromoelctric flux tubes whose sources are charge states in higher dimensional representation of color SU_3. "*These ropes can be viewed as a model of locally deconfined quark matter, which is dominated by longitudinal excitations and therefore of relevance for the preequilibrium stage in nucleus-nucleus collision*"[28]

Skipping to the part which concerns us the most, let me show **Fig. 2.10**, which demonstrates the rapidity distributions for negatively charged hadrons, calculated in different RQMD modes. This model and all it's variations are of no importance to us for two reasons:

1. as one can easily see, the major difference between the models occur at the midrapidity region, where Beam-Beam Counters have no coverage;

2. all collective effects leave no tracks in the fragmentation region ($|y| \geq 2$).

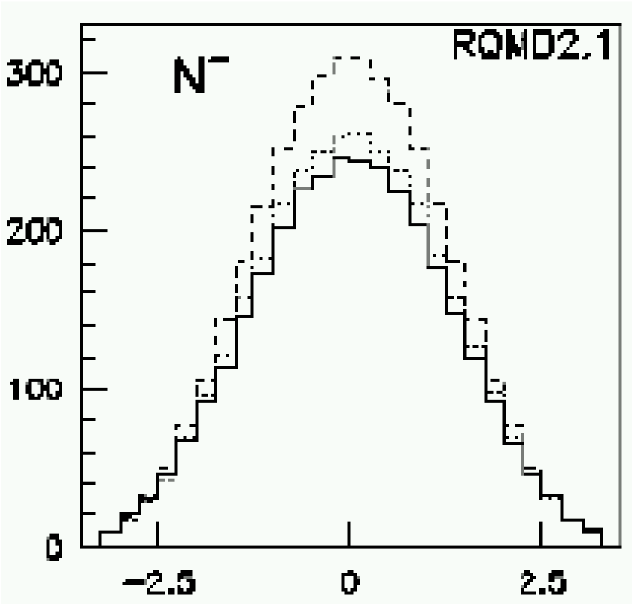

Figure 2.10: Rapidity distribution of negatively charged hadrons in Pb ($160A\ GeV$) on Pb central collisions, calculated in three different modes of RQMD 2.1 [28].

Last argument can be explained by the fact, that rope fields influence mainly particle multiplicities at rapidities which are covered by many strings.

Last comment on **Fig. 2.10** would be, that recalculation of this distribution into the distribution over the pseudorapidity would affect again only midrapidity region, and in order to get all charged particles, one just has to double the numbers on the vertical axis.

UrQMD.

UrQMD : Ultra-relativistic Quantum Molecular Dynamics.

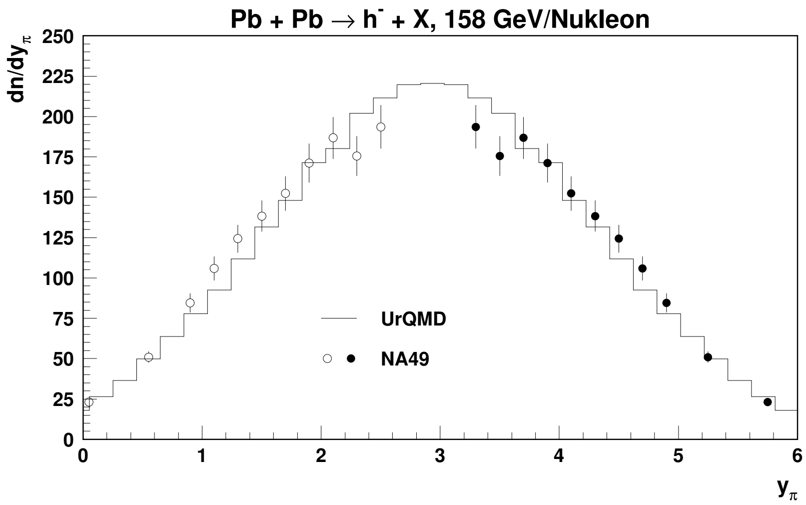

Figure 2.11: Rapidity distribution of negatively charged hadrons for $Pb + Pb$ collisions at the SPS ($160A\ GeV$) [29].

This is yet another microscopic model, now based on a phase space description of the reaction [29]. Heavy ion collision implies high excitation energies and many different species of hadrons. Big mass makes them unstable and wide resonances make it impossible to define quasi particle states. Therefore UrQMD model replaces resonances by continuous string excitations for higher energies.

And, again, we should be interested in the predictions of charged particles distribution as given by this model. **Fig. 2.11** shows $(dN_{negatively\ charged\ hadrons})/dy$ *vs.* y distribution by UrQMD model. It is given in the frame of the particles. **Eq. 1.6** immediately tells us to shift vertical axis by 3 units of rapidity to the right in order to get familiar CM reference frame picture. The main feature of this graph is again relatively small charged densities in the y region, which interests us the most.

Parton Cascade Model.

This model is based on the microscopic dynamics of parton cascades within the renormalization group improved perturbative QCD [16]. It considers fast hadrons as a coherent cloud of partons with life times much larger than the typical interaction times with another particle. Each parton is characterized by its type, the fraction x of the initial hadron energy and its transverse momentum p_t. At any instant an individual parton can initiate a space-like cascade with a finite life-time by branching into a number of partons with smaller x. If one considers this branching as a fluctuation in a coherent wave function of a hadron, then a collision with another particle will act to destroy this coherence. Then, if one of the partons is kicked out by the collision, others can not reassemble back and can now initiate a time-like cascade by emitting further partons.

Up to now, only PCM and HIJING (as compared to other models) use pertubative QCD minijet production to describe dynamics, which makes it even more interesting to compare the two models' predictions of the charged particles distributions in pseudorapidity. **Fig. 2.12** shows the comparison between the two models for central collisions at RHIC planned energies. As one can easily see, the two models roughly agree in general shape of the distribution, but differ in two most important characteristics: central rapidity density value and absolute magnitude of the particle production are different by almost factor of 2!

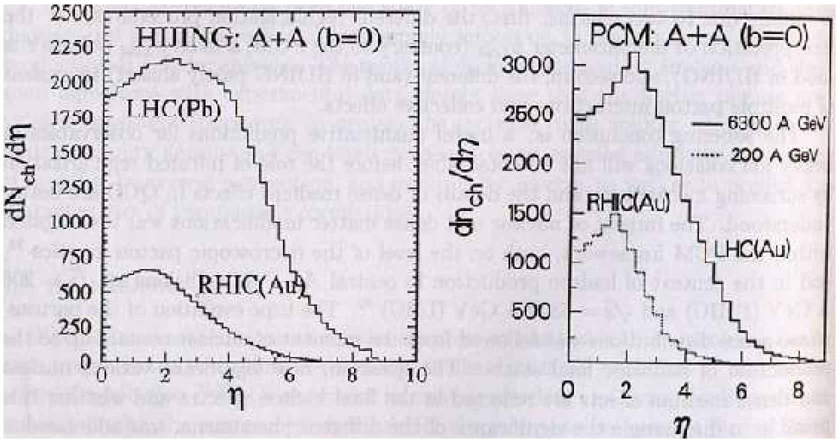

Figure 2.12: Comparison between predictions of HIJING and the PCM for the pseudorapidity spectra of charged hadrons produced in RHIC $Au + Au$ central collisions at $\sqrt{s} = 200A\ GeV$ [16].

Charged particles pseudorapidity distributions extracted by the Beam-Beam Counters will make a big contribution to determining the shape of this distribution, to validating the model, and to determining the absolute magnitude of the particle production.

2.3 First Experimental Results.

As it was mentioned earlier, it is rather complicated to do any kind of experimental overview in this area. The reason for that is the unique position of RHIC among other high energy physics heavy ion collision experiments. There is no collider experiment even close to RHIC's energy range. That is why I can only say a few words, based on the first few published results and the few talks, presented on the "Quark Matter 2001" conference.

2.3.1 Published results.

PHOBOS.

The first published result based on the $Au + Au$ collisions at RHIC appeared in August 2000 on behalf of the PHOBOS collaboration [10]. It reports values of the charged multiplicities at the midrapidity region for two different energies: $\sqrt{s} = 56$ and $130A\ GeV$ of central $Au + Au$ collisions. The numbers reported are:

- for $\sqrt{s} = 56A\ GeV$:

$$\left.\frac{dN_{ch}}{d\eta}\right|_{|\eta|<1} = 408 \pm 12 \pm 30$$

- for $\sqrt{s} = 130A\ GeV$:

$$\left.\frac{dN_{ch}}{d\eta}\right|_{|\eta|<1} = 555 \pm 12 \pm 35$$

Compared to the values obtained from the **Figs 2.7** $-$ **2.12** one can easily see the agreement between the numbers in the midrapidity region with the HIJING model represented by **Fig. 2.9**. Unfortunately, at BRAHMS, we did not acquire enough data at the low energies of $\sqrt{s} = 56A\ GeV$ to produce any analysis. That it why I will be comparing our results only to the results obtained at $\sqrt{s} = 130A\ GeV$ collisions of $Au + Au$. **Fig. 2.13** presents a famous first result from RHIC and shows the normalized charged particles multiplicity density by the participant pair (the number of participants were obtained from different sources) [10].

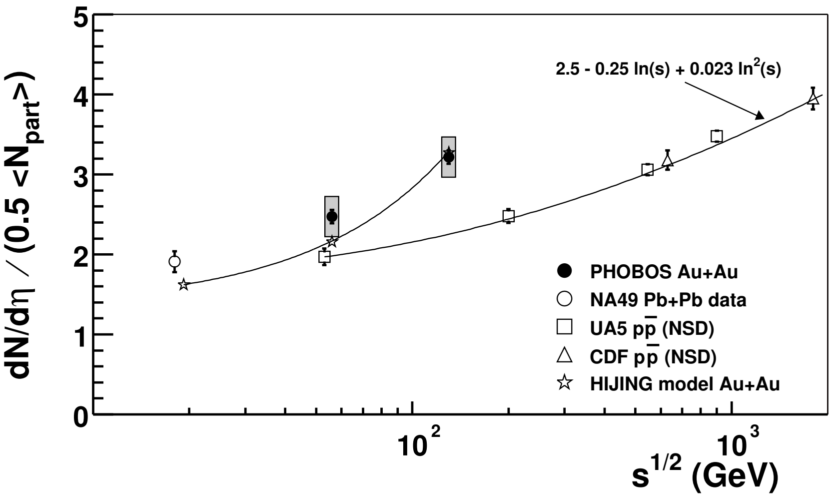

Figure 2.13: Measured pseudorapidity density normalized per participant for central $Au + Au$ collisions [10].

PHENIX.

Another paper, presenting results on the charged particle multiplicities at RHIC was published by the PHENIX collaboration [12]. Results on the $dN_{ch}/d\eta$ at midrapidity region, presented by PHENIX agrees in general with the earlier PHOBOS result. That is why I will skip this part of the paper, instead I would like to say a few words on the mechanism for determining the centrality of the collision event. Similar to the BRAHMS experiment, PHENIX employs

- a set of "*Zero Degree Calorimeters*" (ZDC), capable of measuring the energy of the neutrons, produced in the collision. The number of neutrons is expected to be very small for very peripheral and very central collision, and

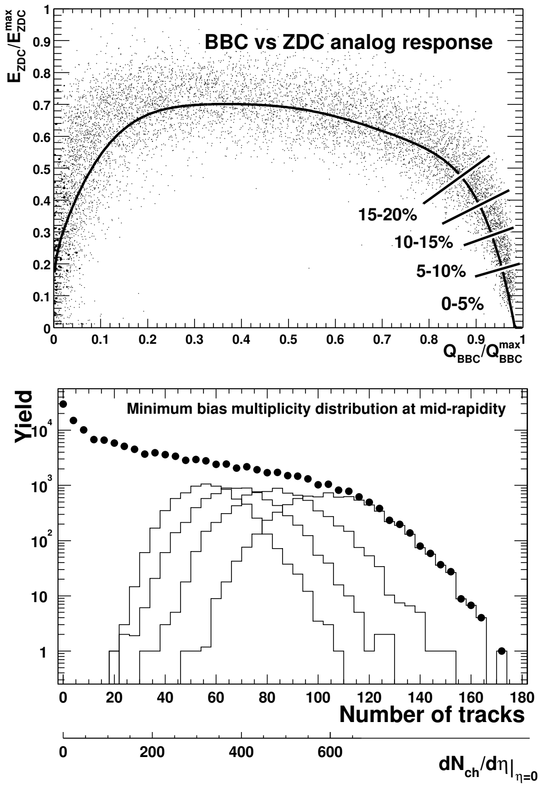

Figure 2.14: PHENIX centrality measure [12].

- a set of the Beam-Beam Counters (BBC), capable of counting the number of charged particles created in the same collision. By the model this number is directly proportional to the number of participants in the collision.

Thus, correlation of these two measurements can serve as a centrality defining mechanism. Exactly the same method was used by us in determining the centrality for the collisions at BRAHMS for the purpose of the Beam-Beam Counters analysis. **Fig. 2.14** shows PHENIX BBC *vs.* ZDC analog response, which was used to make an event selection based on the centrality of the collision. Different cuts are shown.

> *No full charged particle multiplicity distributions were officially published for the wide range of pseudorapidity. We hope to pioneer in this area.*

2.3.2 "Quark Matter 2001".

This section will show some results, presented at the annual meeting "Quark Matter 2001" this January at State University of New York at Stony Brook. it is very complicated to describe talks, which carry the label "*preliminary*" on them, so I will only say a few words about the results related to this thesis.

$dN_{ch}/d\eta$ distributions.

"Measuring the charged particles multiplicity distribution for a wide range of pseudorapidity" is one of the objectives of the PHOBOS collaboration, that is why results presented by them was of the greatest importance to us. **Fig. 2.15** shows this distribution for several centrality cuts.

Respecting the preliminary status of the result, I don't want to draw any conclusions from it or to do any comparisons with the models. We will use it as a reference, once we arrive at our final result.

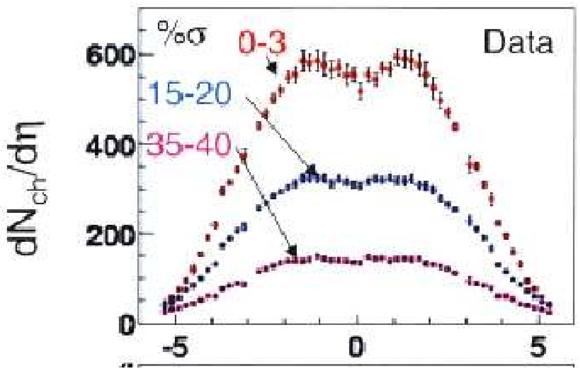

Figure 2.15: Charged particles multiplicity density for different centrality cuts. Preliminary by the PHOBOS collaboration [30].

Centrality definition.

Another interesting result, I would like to mention here, was presented by the PHENIX collaboration [31]. Compared to the one, mentioned in **Sec. 2.3.1**, it demonstrates again the validity of using ZDC total energy signal *vs.* Beam-Beam Counters total multiplicity as a centrality definition. **Fig. 2.16** shows ZDC *vs.*

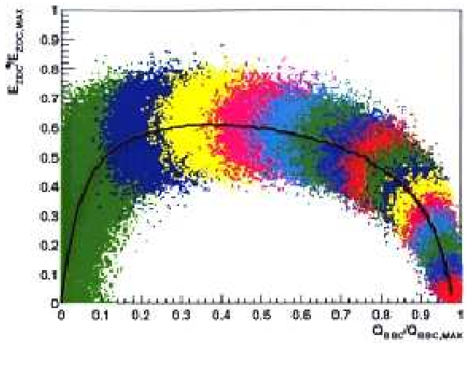

Figure 2.16: ZDC *vs.* BBC simulated centrality definition by the PHENIX collaboration [31].

BBC dependence for the Monte-Carlo simulations. This is the method, which will be used by us later in this text to identify the centrality of the collisions.

Conclusion.

For the conclusion of this section I should just say, that

> *the subject of this thesis is an open field and we hope that our results, described later, will shed some light on the complicated subject of charged particle production in a high energy heavy ion collision.*

CHAPTER 3
EXPERIMENTAL OVERVIEW

This chapter is devoted to the description of the experiment and consists of three major parts. The first of them gives a brief overview of the Relativistic Heavy Ion Collider. The second one describes the BRAHMS detector, as one of the four detectors taking physics data during heavy-ion collisions at RHIC. And the third and the last one is related to the hardware part of the BRAHMS experiment related to the Beam-Beam Counters. It will describe electronics, trigger details and data acquisition, used to extract the physical data to be analyzed in **Ch. 6**.

3.1 RHIC at BNL.

The Relativistic Heavy Ion Collider (RHIC) was designed and built at Brookhaven National Laboratory to study collisions of heavy ion beams (*e.g.* beams of the nuclei of gold atoms) at energies which range up to $200 GeV$ [32]. This kind of center-of-mass energies exceed by an order of magnitude the capabilities of all other existing accelerators. The collider consists of two concentric rings of superconducting magnets located inside the ring tunnel of $\sim 3.8km$ circumference. The layout of the tunnel and the configuration of the magnet lattice allows the two rings to intersect at six locations along the circumference where the counterrotating beams collide with each other. A chain of several accelerators, namely: Tandem Van de Graaf, Booster Synchrotron and Alternating Gradient Synchrotron (AGS) are used to preaccelerate ions for injection into the collider.

Bending and focusing of the ion beams is achieved by the collider ring magnets. The magnets are cooled to a temperature of $< 4.6K$ by circulating liquid helium. In order to avoid beam loss and radiation background, a vacuum of about $7\times10^{-10}mbar$ is required in the warm beam tube sections of the insertion regions. An important choice in the RHIC design was the utilization of short bunches colliding head-on to enhance the luminosity while keeping the average current and stored beam energy low.

> $Luminosity$: measure of sensitivity and gives directly the number of events per second for a cross section of $1cm^2$, as

$$\frac{N_{events}}{second} = \sigma \times Luminosity \quad [33].$$

Formation of the bunches occurs prior to injection. I will skip the part describing the actual accelerating and ion creation and just show **Fig. 3.1**, which illustrates all that.

It is designed to inject 120 bunches into each collider ring in bunch-to-bucket fashion. Present operational results project a gold intensity of $1 \times 10^9 ions/bunch$ or a total of $6 \times 10^{10} ions$ in the 57 bunches in each ring. **Table 3.1** summarizes the major RHIC performance parameters.

Four of the beam intersection regions mentioned above are occupied by the detectors. One of these detectors is called BRAHMS.

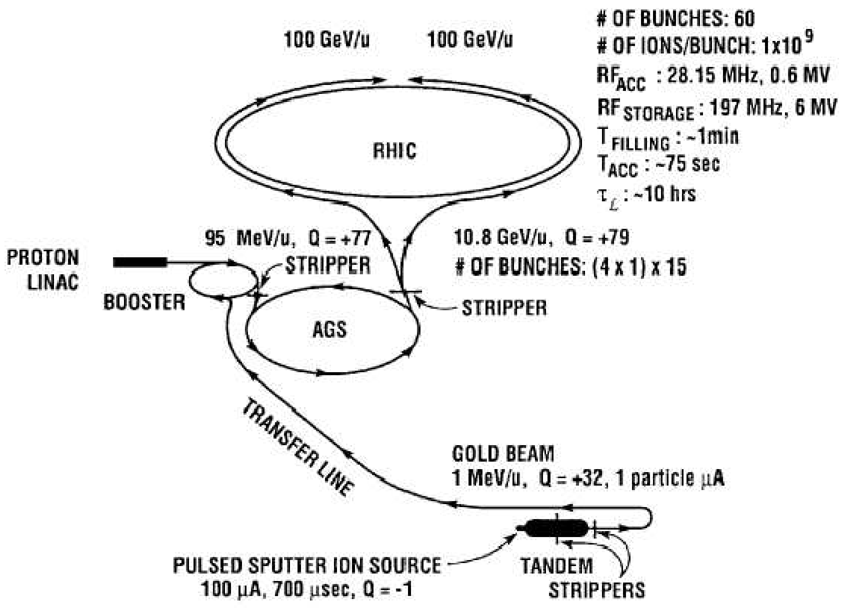

Figure 3.1: RHIC acceleration scenario for gold [32].

No. Intersection Regions	6
No. Bunches/ring	60
Bunch Spacing ($nsec$)	213
Collision Angle	0
Free Space at Crossing Point (m)	± 9
No. Particles/Bunch	1×10^9
Top Energy (GeV/u)	100
Emittance, initial (mm.mrad)	10
Collision Diamond Length (cm rms)	18
β^* (m)	2
Luminosity, average ($cm^{-2} \times sec^{-1}$)	$\sim 2 \times 10^{26}$
Lifetime (h)	~ 10

Table 3.1: RHIC performance characteristics [32].

3.2 BRAHMS at RHIC.

J. BRAHMS stands for Broad RAnge Hadronic Magnetic Spectrometer. Brief description of it's major parts and components forms this section of my thesis.

3.2.1 BRAHMS Overview.

Now let me try to connect all Heavy Ion Collisions theory, outlined in **Ch. 2**, with a real BRAHMS experiment, which is designed in general to measure charged hadrons over a wide range of rapidity and transverse momentum for all available beams and energies at RHIC [7]. As was mentioned already in a previous part, the creation of the baryon-poor, high-temperature plasma depends on attaining collision energies far above the stopping regime. The colliding nuclei will pass through each other and the baryon-rich regions will be close to the original nuclei in rapidity. The most basic information available for understanding of what is happening in a heavy ion collision will come from the momentum spectra and multiplicities as a function of transverse momentum, p_t and rapidity, y. One of the goals of our experiment is to measure these quantities in regions where they are most sensitive to model predictions.

BRAHMS is designed to operate in the pseudorapidity interval $0 \leq \eta \leq 4$ ($2^o \leq \theta_{lab} \leq 90^o$). Different experimental conditions lead to the creation of two different spectrometers: Forward Spectrometer and Midrapidity Spectrometer. Forward Spectrometer is divided into two arms called “*Front Forward Spectrometer*” (FFS) and ‘*Back Forward Spectrometer*” (BFS). Both parts can move independent of each other and forward rapidity coverage limits were selected based on the criteria, that measurements should extend over a sufficiently wide range of rapidity. Such design leads to a unique geometric acceptance of BRAHMS, as shown on **Fig. 3.2**. Both spectrometers are shown on **Fig. 3.3**, and now let me describe them in more detail.

Forward Spectrometer.

It covers angles from 2.3^o to 30^o degrees and consists of

- Four dipole magnets $D1 - D4$ for sweeping and analyzing primary particles emerging from the reaction;
- Two tracking detectors $T1$ and $T2$ – small time projection chambers (TPC's), providing good $3d$ track recognition (reconstruction of a particle track through the spectrometer) and rejection of background;
- The tracking detectors $T3$ - $T5$ are conventional drift chambers. The positions of tracks are determined locally to better than $0.3mm$ and their direction to better than $0.5mrad$;
- Two time-of-flight hodoscopes $H1$ and $H2$ are responsible for the lower momentum part of the particle identification. $H1$ provides 4σ separation of π and K to momenta of $3.3GeV$ and K/p to momenta of $5.7GeV$. $H2$ allows 4σ

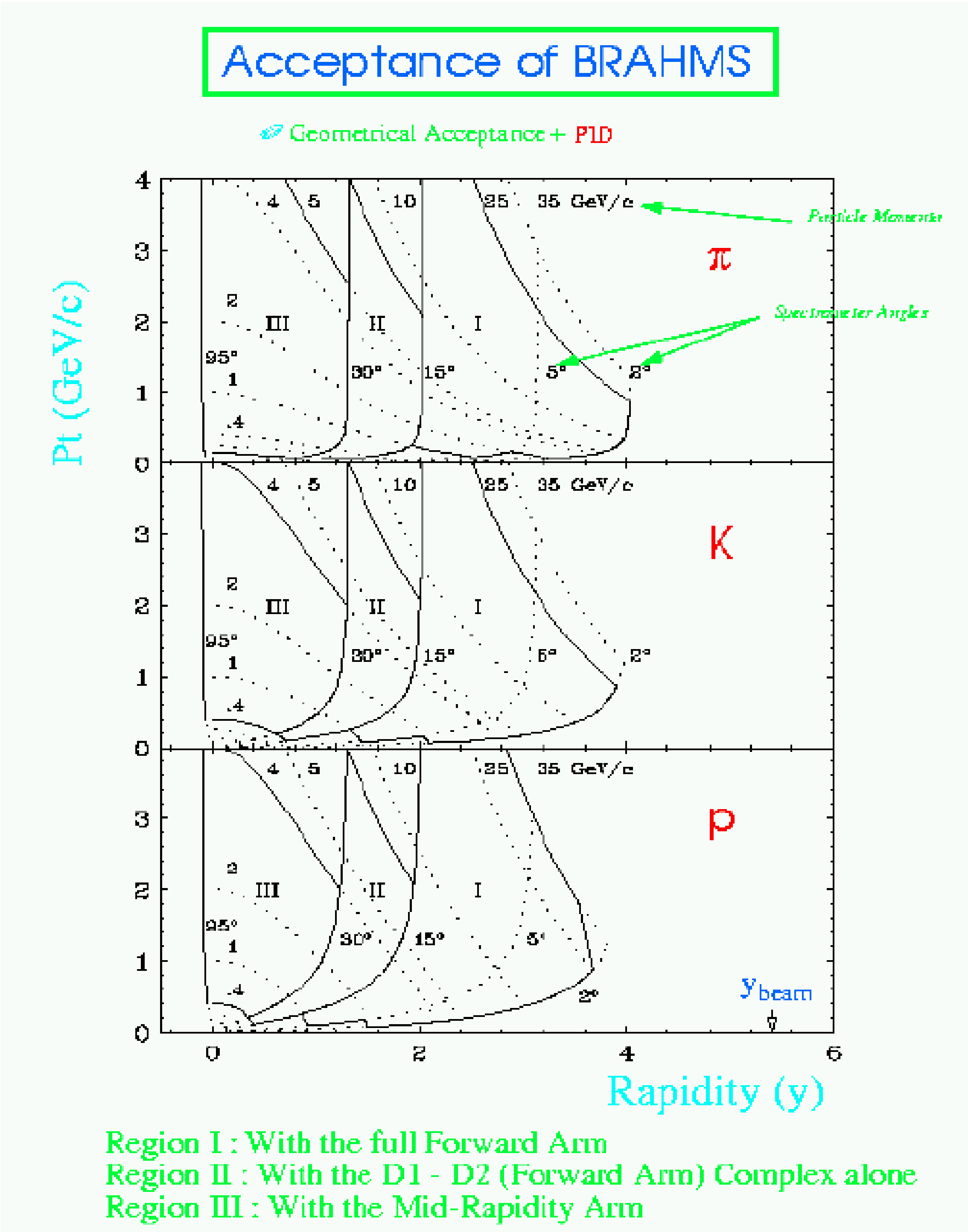

Figure 3.2: BRAHMS geometric acceptance of hadrons as a function of rapidity and transverse momentum.

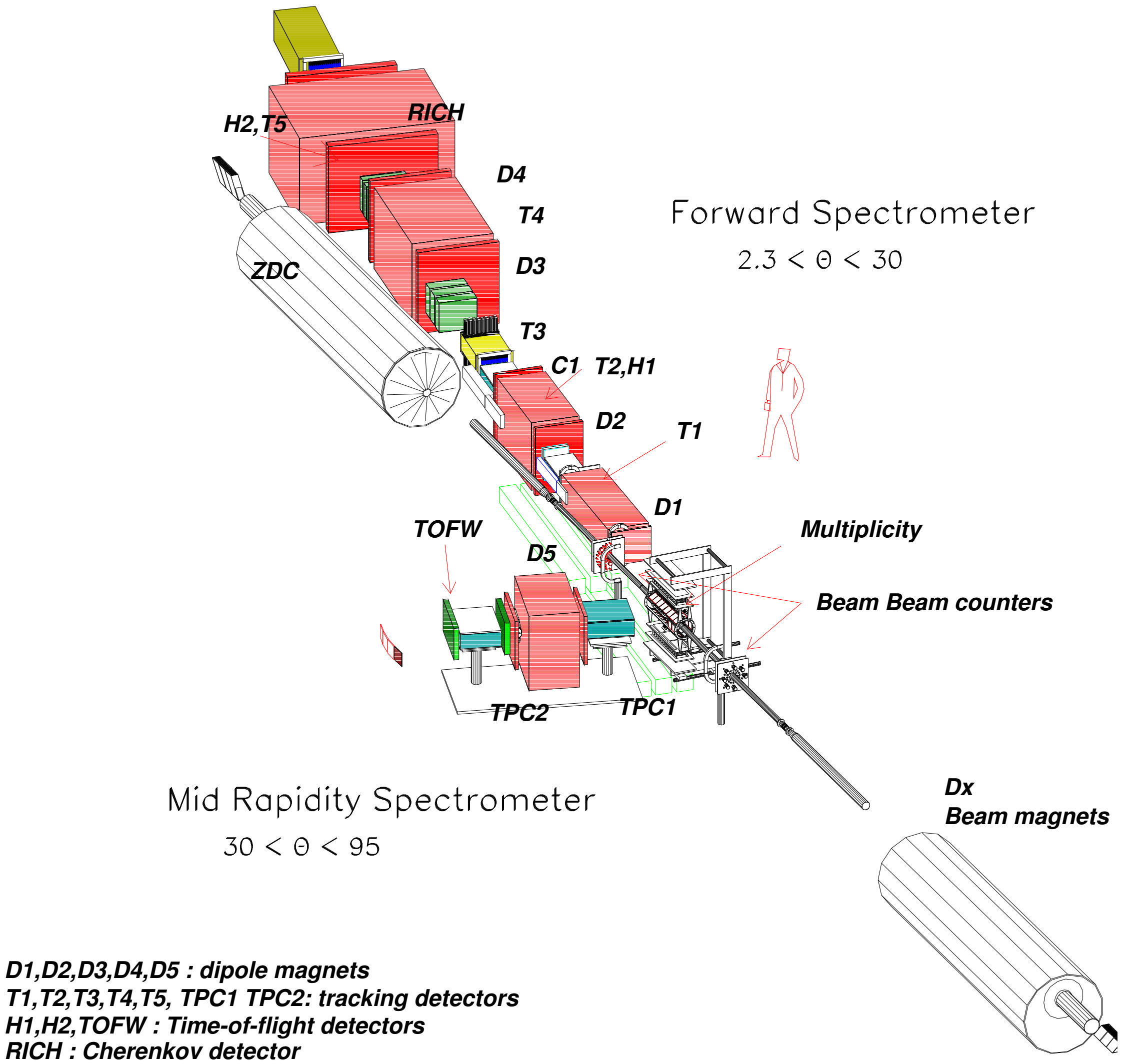

Figure 3.3: *BRAHMS*: Broad RAnge Hadron Magnetic Spectrometer. Top view of all detectors and magnets used in the experiment.

separation of π/K to momenta of $5.8 GeV$ and K/p to momenta of $8.5 GeV$. Their time resolution is $\sigma \leq 75 psec$;

- Cherenkov tank $C1$ and ring-imaging Cherenkov detector $RICH$ will provide high momentum particle identification. $C1$ extends the particle identification behind $H1$ to $9.0 GeV$ and $RICH$ allows $K/\pi/p$ separation up to ~ 25. $RICH$ is also able to produce radius measurements with an accuracy of $\Delta r/r \simeq 2\%$.

Midrapidity Spectrometer.

It covers angles from 30^o to 90^o degrees and consists of

- Two time projection chambers $TPM1$ and $TPM2$. $TPM1$ provides tracking in front of the magnet to distinguish original particles from the decayed ones and determines the vertex with a precision of $1mm$;
- Magnet $D5$ between them;
- Time Of Flight Wall ($TOFW$) will measure time of flight with a time resolution of $\sigma \leq 75 psec$.

The most detailed technical description of the BRAHMS experiment can be found in reference [34].

Global Detectors.

They are responsible for providing global trigger to the experiment, and more than other parts of BRAHMS, are related to this thesis. Let me be more detailed in their description. The global detectors are:

- **Multiplicity Array** or Centrality Detector, made of two layers of detectors along the beam pipe and are designed to provide a multiplicity of each event and to measure the centrality on an event-per-event basis. This detector also measures charged particles multiplicity distributions ($dN_{ch}/d\eta$) in the midrapidity region of $|\eta| \leq 2.2$. These measurements, together with the Beam-Beam Counters result for $1.85 \leq |\eta| \leq 4.70$, will make a complete picture of the charged particles multiplicity distribution for different impact parameters of the collision.

  This detector is made of two parts. One of them consists of a plastic scintillating tiles and the other one of silicon strips mounted in a two layer structure as shown on **Fig. 3.4**.

- **Zero Degree Calorimeters** (ZDC) are a common device for all RHIC experiments and, as follows from their name, will be located far away from the interaction point almost at 0^o, as shown on **Fig. 3.5**. They are designed to measure emitted "*spectators*" neutrons from the collision and by measuring their energy can determine impact parameter of the collision. Thus, ZDC energy measurements in correlation with, say Beam-Beam Counters total number of hits can serve as a good centrality measure. This will be discussed in more details in **Sec. 5.3.1**.

  ZDC consist of 3 modules. Each module consists of several layers of tungsten plates followed by a ribbon of PMMA fibers. The plates are tilted 45^o to

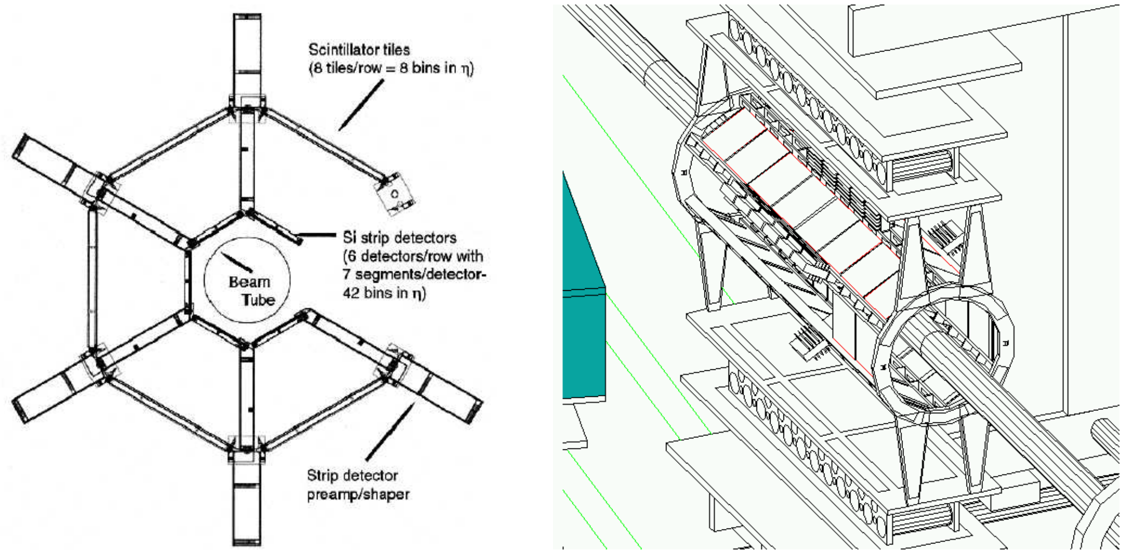

Figure 3.4: BRAHMS Multiplicity Array.

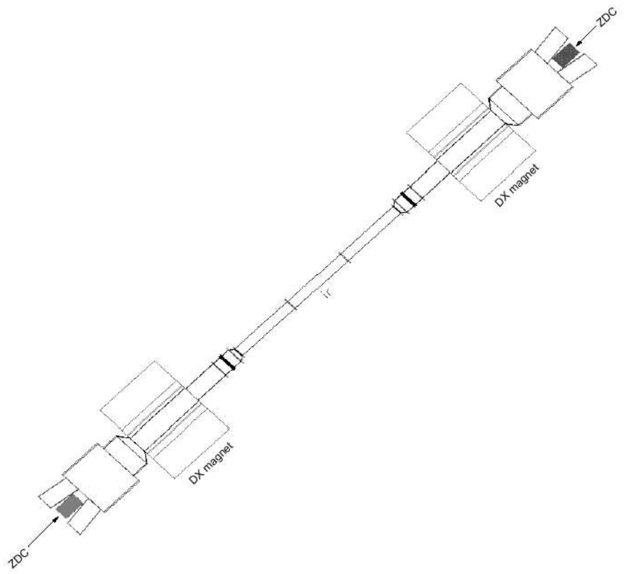

Figure 3.5: BRAHMS ZDCs.

the beam. The time resolution of the ZDC is about 115$psec$, meaning, that calorimeters should be able to locate z_o position of the interaction with the resolution of 2.2cm calculated as:

$$\delta z_o = \frac{\delta t_o}{\sqrt{2}} \cdot c \;\Rightarrow\; \delta z_o \simeq 2.2cm,$$

where $\sqrt{2}$ factor is due to the two arrays of the ZDC on both sides of the collision vertex. In addition to that, they are used to monitor luminosity in heavy-ion collisions [35].

- Beam-Beam Counters:

3.2.2 BBC at BRAHMS.

As it was mentioned in **Ch. 1**, the Beam-Beam Counters will be employed to characterize collisions from a global perspective; form a level0 trigger; permit a rapid estimate for the collision point (vertex location) with better resolution than the ZDC, and serve as a first probe of charged multiplicity. The collision instant t_o determined by the Beam-Beam Counters will be used for the particle ID by the other BRAHMS detectors. The lowest level trigger (level0) is formed by requiring the coincidence between signals from the RHIC clock and from the Beam-Beam Counters. The full arrays, located at 219cm backwards and forwards of the beam vertex can provide a start–time for the time–of–flight counters and to determine the vertex position to roughly 1cm.

Fig. 3.6 shows the actual view of the two Beam-Beam Counters arrays. The

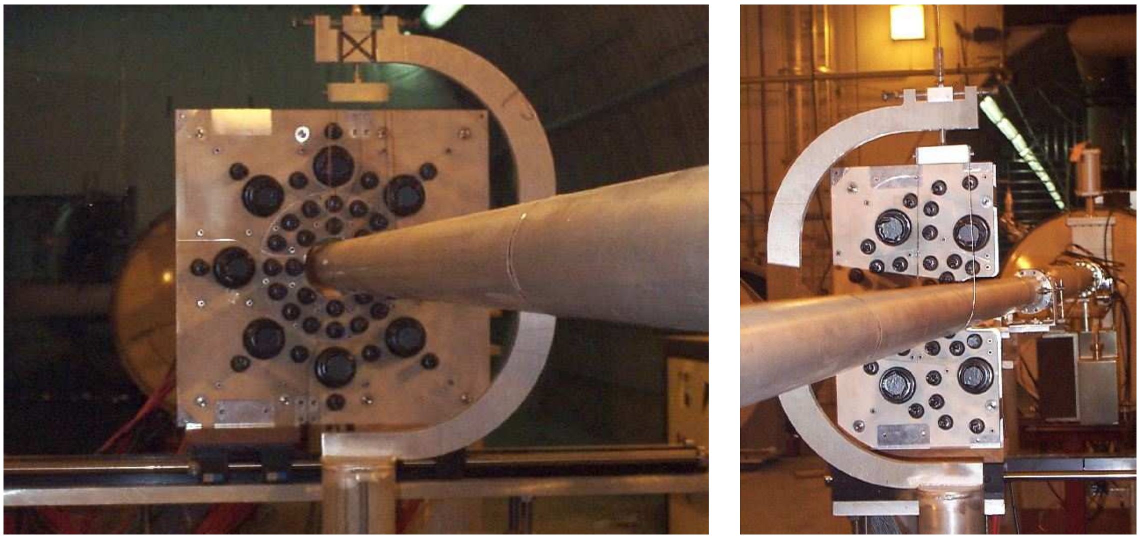

Figure 3.6: Actual view of the Beam-Beam Counters arrays. Left Array and Right Array.

Right Array has reduced azimuthal coverage because of the magnet D1. It is partially compensated by higher spatial density of modules in the Right Array. Each detector consists of Cherenkov radiators, glued to a photomultiplier tube. Phototubes diameters are $19mm$ or $51mm$ with $4cm$ long or $3cm$ long radiators respectively. The radiator length was chosen, such that a $\beta = 1$ charged particle will have a timing resolution of $50psec$ and by energy response, that will facilitate a multiplicity measurement. Also, several counters in both arrays are located at the same distance from the beam-pipe, which should provide better precision and might help in case of any malfunction diagnostics. A more detailed description of the design criteria will be given in **Ch. 4**.

3.3 Beam-Beam Counters Hardware.

Let me follow the parts of our detector one by one and say a few words about each.

3.3.1 Photomultiplier basics.

As it was mentioned already, the Beam-Beam Counters are a set of phototubes with Cherenkov radiators in front. So, in order to describe the work of such a device we should first say a few words about Cherenkov radiation.

Cherenkov Radiation.

Cherenkov Radiation is a characteristic electromagnetic radiation, which is emitted by a charged particle, traversing a medium with a refractive index n with a velocity v exceeding the velocity of light c/n in that medium[2].

The origin of the Cherenkov radiation can be explained by the polarization of the medium atoms along charged particle's track, so they become electric dipoles.

[2]

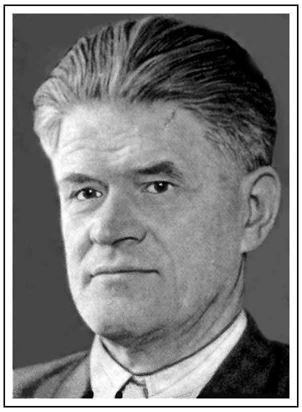

Figure 3.7: Cherenkov

It was discovered in 1934 by P.A.Cherenkov, who was a graduate student of a prominent Russian physicist S.I.Vavilov. Professor Vavilov did not quite believe in a possibility of such discovery, so he made it a routine project for his graduate student. One of the anecdotes says, that Cherenkov had to eat tons of carrots to improve his sight and finally, blue light was detected in a bottle of water subjected to radioactive bombardment. Experiment had to be done in a dark room, so Cherenkov could detect this light. He received his Nobel Prize in 1958 for his discovery (effect was explained in 1937 by Frank and Tamm, who were co-recipients of the Noble Prize). Anybody could have been in his shoes; his adviser was never mentioned. This discovery became one of the famous scientific anecdotes of all times and became a main encouragement for graduate students to work hard.

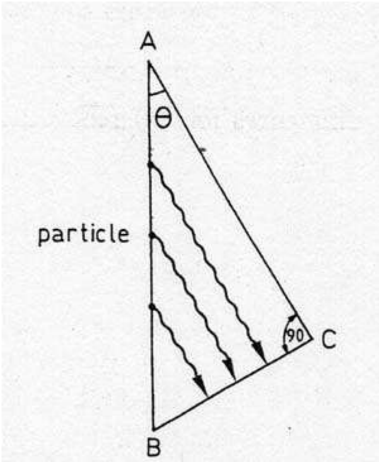

Figure 3.8: Cherenkov angle.

Dipole's field variation leads to the radiation emission. And if $v > c/n$, then dipole field integrated over the particle's path doesn't vanish anymore, and non-zero total dipole moment emits radiation. Let me follow reference [36] and write some simple formulae, as shown on **Fig. 3.8**. Particle travels distance $AB = t\beta c$; photon travels $AC = t \cdot c/n$. Therefore for the angle between the emitted Cherenkov photons and the track of a charged particle:

$$\cos\theta_c = \frac{c}{n\beta c} = \frac{1}{n\beta}$$

We can use reference [37] and write down the intensity of the Cherenkov light. For the number of quanta radiated per unit length with frequency between ν and $\nu + d\nu$

we will have:

$$dN = \frac{2\pi e^2}{\hbar c}\left(1 - \frac{1}{n^2\beta^2}\right)\frac{d\nu}{c} = \frac{2\pi e^2}{\hbar c}\sin^2\theta\frac{d\nu}{c} \tag{3.1}$$

So, for the visible light limits, **Eq. (3.1)** gives us approximately $750\sin^2\theta$ photons per centimeter. In our case, we have a radiator made of lucite, which has $n \simeq 1.5$, so, we should have around 400 photons per centimeter, or 1200 photons for the $3cm$ radiator. And the particles are moving there with the speed of light, which makes the device very fast. Thus, transparent Cherenkov radiators, coupled with optical devices and photomultipliers, make useful velocity selectors for high–energy particles.

Photomultiplier and Dark Current.

So charged particles go through the Cherenkov radiator and create light. The light then enters the photomultiplier and "*liberates electrons from an alkali-metal photocathode via the photoelectric effect. A negative high voltage is applied to the photo-cathode. The photoelectrons are focussed by an electric field onto the first dynode, which is part of the multiplication system. The anode is normally at ground potential. The voltage between the photocathode and anode is subdivided by a chain of resistors. This voltage divider supplies further dynodes between the photocathode and anode so that the applied negative high voltage is subdivided linearly*" [36] (**Fig. 3.9**).

However, even when a photomultiplier is operating without any external source

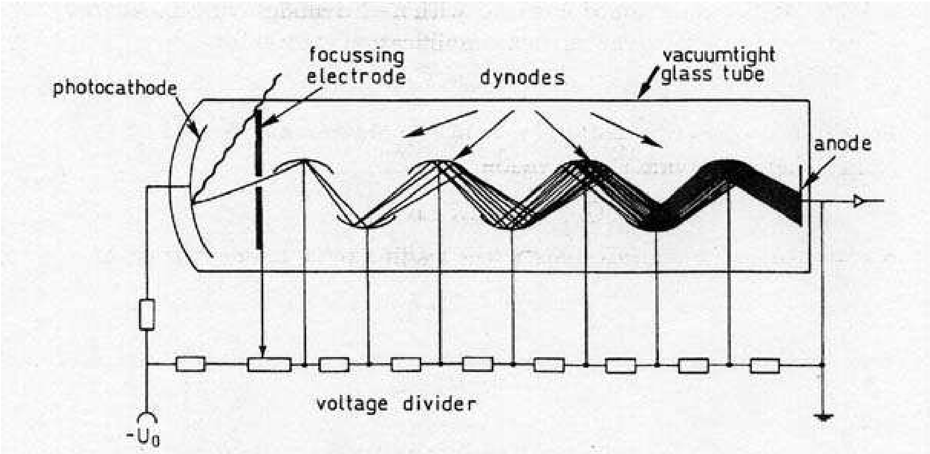

Figure 3.9: Working principle of a photomultiplier. The electrode system is mounted in an evacuated glass tube. The photomultiplier is shielded by a metal cylinder against stray magnetic fields [36].

acting on it, a small residual anode current is found to still exist, the so-called "*dark current*". Reference [38] categorizes the causes of a dark as follows:

1. Thermionic emission of electrons.
2. Ionization of residual gases.
3. Glass scintillation.
4. Ohmic leakage.
5. Field emission

The dark current imposes a limit on the magnitude of the signal (genuine light flux) which can be measured by a tube. For a zero level trigger it is very important to us to distinguish real signals from spontaneous noise fluctuations in a photocathode. Clearly methods to remove or substantially reduce this dark count are needed. The "*coincidence*" requirement is a powerful method to reduce accidental counts from the dark current. Only coincidence of the two phototubes in the Left and Right Arrays will be counted as a signal. Another method, complimentary to the coincidence, is to use a discriminator for a timing signal. This method requires some special equipment, which is discussed in the next section.

3.3.2 Main electronics.

In this section I would like to say a few words about the electronics, used to support the Beam-Beam Counters performance in our experiment.

Discriminators.

We have to distinguish between analog signals with variable pulse hights, coming from the phototube, and digital signals with well-defined amplitude. Analog signals carry not only pulse-height information, but also some information based on their shape, *i.e.* time structure. Because of a standard shape of a digital signal, it is much easier and faster to process them, than to process analog signals. Thus it is very convenient to use a discriminator and convert an analog signal into digital. [39]:

> *Discriminator* : a device, which gives an output pulse of a standard shape for every input pulse which exceeds a voltage threshold of our choice.

The value of this threshold usually varies from $10-20mV$ to $1V$. In other words, it not only converts an analog signal into digital one, but also determines which analog signal is worth converting. In our experiment we would like to detect any signal, which is just above the noise level, so we have set the threshold at the level approximately corresponding to 10% of the signal created by 1 Minimum Ionizing Particle ($\sim 100-150mV$). The output pulse is rectangular in shape and of fixed height and width. The only information this pulse is carrying, is that the desired feature (crossing the threshold by the investigated pulse) has occurred. Mainly discriminators are used in rate counting and providing input for coincidence and timing circuits. Timing here means arrival time measurements with respect to the other signal or some start signal.

Accurate timing involves a correction for "*walk*" or "*slewing*": the output pulse from the discriminator appears at or just after the time instant when the input pulse crosses the threshold. Thus the appearance time "*walks*" with respect to the beginning of the pulse when the pulse height changes. In **Fig. 3.10** pulse B crosses threshold X later than the larger pulse C, showing walk due to the pulse height. It means, that some more complicated criteria has to be used in our discriminators for timing purposes and we might not be able to discriminate signals based on a leading-edge crossing. This problem could be overcome by requiring that a constant fraction of the signal must exceed a preselected value (constant fraction discriminators). A whole subsection of this thesis is devoted to our studies of the Constant Fraction Discriminators, but first, let me just say a couple of sentences about Converters:

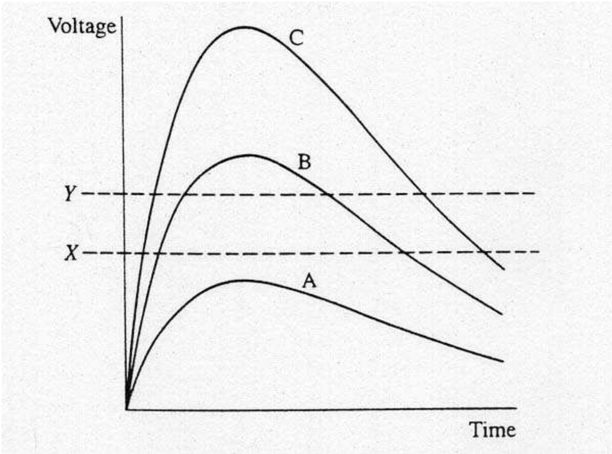

Figure 3.10: Selection of pulses according to their height on a discriminator.

Converters and Logic Units.

As we already agreed above, it is much more convenient to work with digital signals, than with an analog signal. Thus the fundamental interface between analog and digital electronics are circuits which convert the analog information into an equivalent digital form: analog-to-digital converters (ADC) and time-to-digital converters (TDC). Logic units have to be used in trigger formation in order to do event selection. The particular electronic units used for the Beam-Beam Counters will be discussed in more detail in **Sec. 3.3.4**.

3.3.3 Constant Fraction Discriminator.

A triggering process could become a problem if our timing device is not able to separate two pulses from consecutive incoming particles. So, we have spent some effort trying to choose the timing device by the property of its handling two pulses,

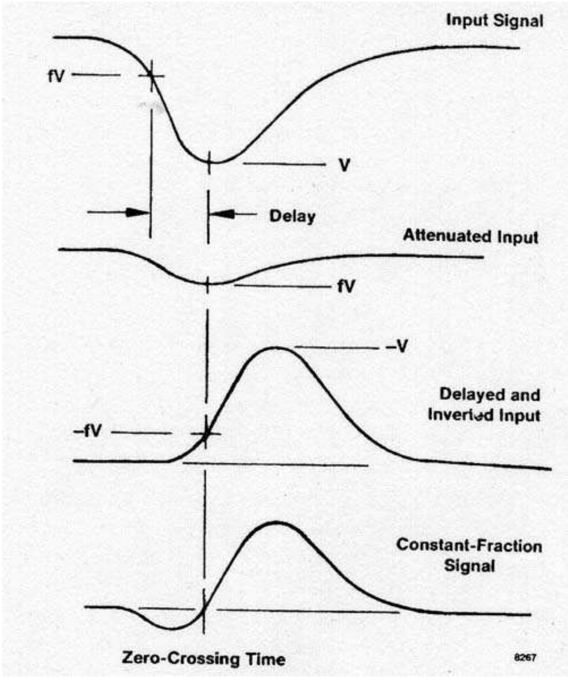

Figure 3.11: Formation of the CFD Signal

which are apart from each other in time by the order of *pico-seconds*.

Historically, fast timing discriminators were designed to work with negative pulses from the photomultiplier tube. Constant Fraction Discriminator (CFD) represents a circuit that would always trigger at the optimum fraction of the pulse height [40]. It functions by splitting the pulse into two parts. One part is attenuated to a fraction f of the original amplitude, and the other part is delayed and inverted. These two signals are subsequently added to form the constant fraction timing signal as in **Fig. 3.11**.

The delay is chosen to make the optimum fraction point on the leading edge of the delayed pulse line up with the peak amplitude of the attenuated pulse. Consequently, adding the two signals yields a bipolar signal with a zero crossing that corresponds to the original point of optimum fraction on the delayed signal. The CFD incorporates a timing discriminator that triggers on the zero–crossing, thus, providing a time marker at the optimum fraction of pulse height. Since the time of zero-crossing is independent of pulse amplitude, the constant fraction discriminator delivers virtually zero walk.

Logic pulses can be counted in a counter/time or in a multichannel scaler. The maximum permissible counting rate is restricted by the pulse–pair resolving time of the system, and discriminator just measures the arrival time of detected events. The question is how is it going to handle two events coming almost one after another? And that was studied in some small experiment, described below:

Trombone Experiment.

The performance of the Constant–Fraction Discriminator was analyzed using the following technique. A standard β–source was used as a signal for the small phototube. Then, we used a set of separate delays and a coaxial cable of variable length, called a "*trombone*". The "trombone" can introduce various small delay into the system, by varying its length. The input signal was split in two. One served as a `START` the other one, significantly delayed (not by a trombone!), served as a `STOP`. The one, which served as a `STOP` was made out of two signals (see **Fig. 3.12**), one of them was delayed by "trombone". The question was, how the CFD will treat two pulses, if they are separated just by the extremely small time of trombone, typically – *pico-seconds.*

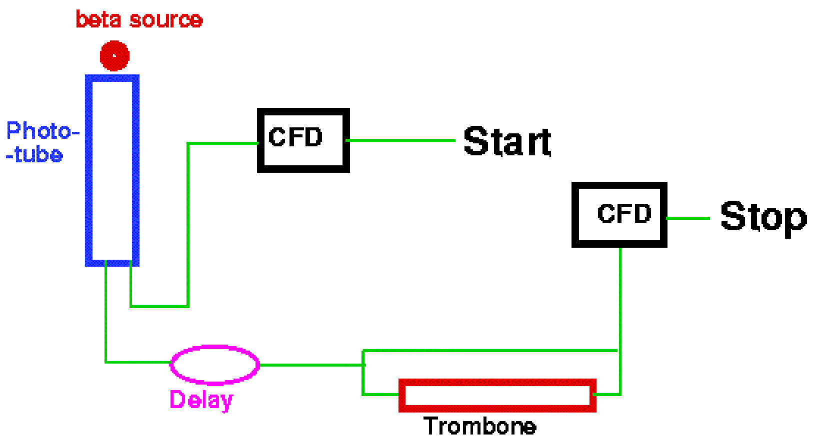

Figure 3.12: Using “Trombone” in CFD.

The experimental results of the CFD behavior for different trombone delays is shown in **Fig. 3.13** as a `STOP` time in *nano-seconds* dependence on the trombone delay time in *pico-seconds*. Straight lines represent the case, when stop signal is delayed by the big constant delay, and stars mark the CFD behavior. As you can see, it's behavior is far from ideal in the case of two pulses coming few picoseconds apart from each other. In ideal case our experimental curve should follow straight lines with a sharp jump from one to another at the intersection point. Will the CFD be able to separate these two pulses? In order to answer that question we tried to look more deeply into the theory of a CFD.

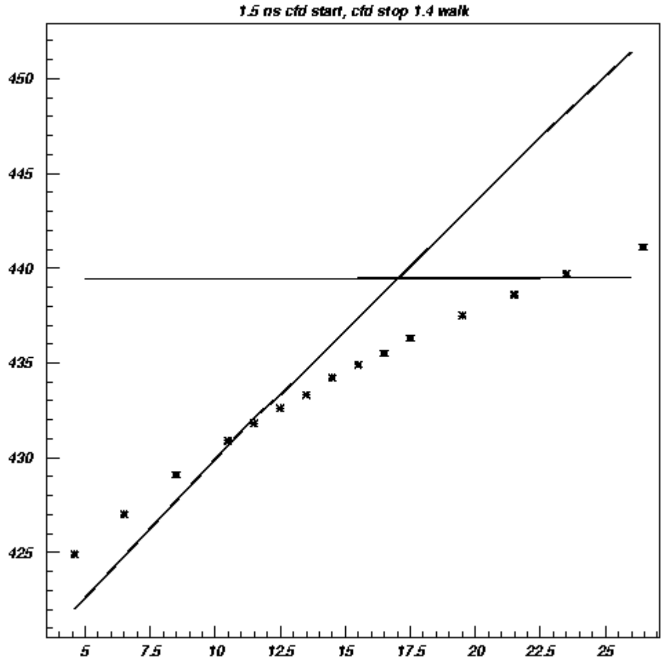

Figure 3.13: Experimental picture of CFD behavior.

Theoretical approach.

For theoretical analysis we chose an input signal with a form

$$P_1(t) = -t^6 e^{-3t}. \tag{3.2}$$

These specific numbers were chosen because they give a signal with characteristics almost identical to those of the small detector, which were used in the actual

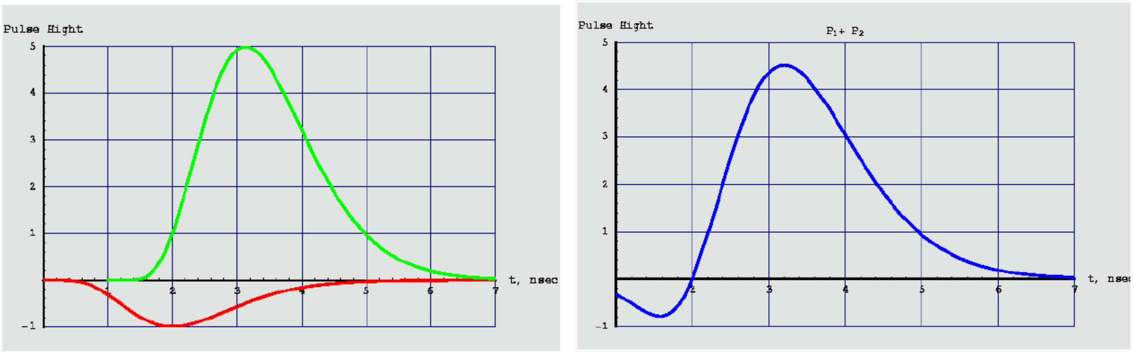

Figure 3.14: Theoretical pulses P_1 and P_2, as they go into the CFD.

experiment. We invert, amplify and delay the original impulse:

$$P_2(t) = 5(t - \Delta)^6 e^{-3(t-\Delta)},$$

where Δ is the delay. We add $P_1(t)$ and $P_2(t)$ and look for zero–crossing:

$$P_1(t) + P_2(t) = 0$$

Regarding the choice of Δ, the CFD manual recommends using a delay of a 20% of the inverted pulse height. **Fig. 3.14** shows both pulses and the sum of them for the delay $\Delta = 1.13nsec$, which gives a clear zero crossing at a time of $t = 2.0nsec$.

In the next step we look for two pulses, delayed with respect to each other. This is accomplished by keeping the original pulse $P_1(t)$, and adding the second pulse delayed by $-1.2nsec$. We then repeat the addition, incrementing the actual value of the delay. This simulates a second pulse going through the first one with very small steps. **Fig. 3.15** shows results of these studies as a dependence of the

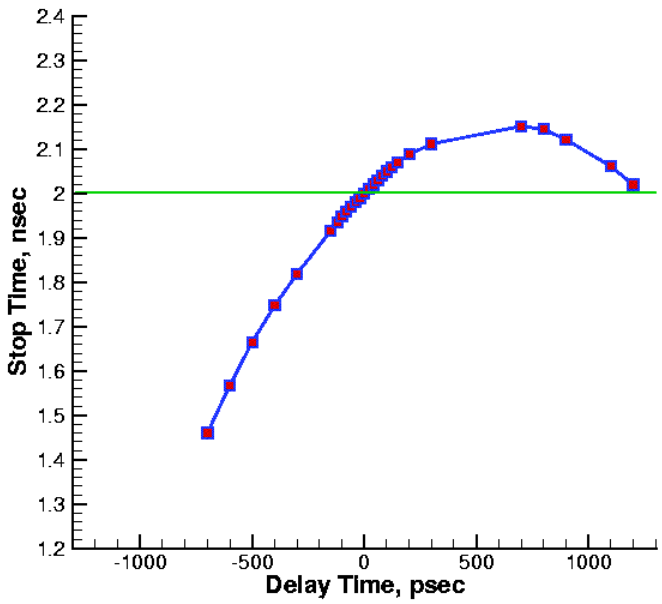

Figure 3.15: Theoretical picture of CFD behavior.

`STOP` time on the delay time Δ.

A comparison of **Fig. 3.15** with **Fig. 3.13** leads to the conclusion, that the CFD is not capable of providing us with a good timing for the experiment, since the experimental behavior is so far from the theoretical predictions. This conclusion was the basis for the decision to use "*leading edge*" discriminators.

Now let me return to the main story and describe how the Beam-Beam Counters are cabled on the experimental floor and what electronics is used for the data acquisition.

3.3.4 Principal Cabling Scheme.

AppendixB has a very detailed cabling description, with the actual electronic module numbers, including the cable and channel numbers used. The scheme of the Beam-Beam Counters cabling and electronics used is shown in **Fig. 3.16**. Now, let

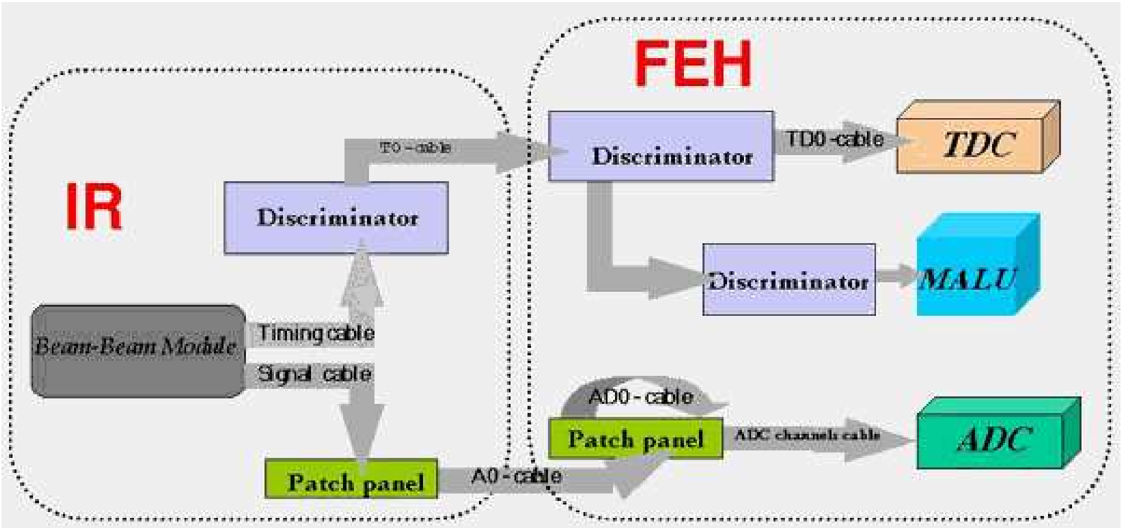

Figure 3.16: Beam-Beam Counters Cabling scheme.

me describe the electronics employed, going left to right in the figure. "*IR*" stands for the "*Interaction Region*"and "*FEH*" for "*Fast Electronics Hut*".

Analog Signal.

Analog cables run through a set of patch panels, extension and delay cables to the FE Hut, where they then go into the *LeCroy 1885F* FASTBUS ADC unit. It has 96 inputs and current into each of them is integrated during the period for which a gate signal is applied to the module. It supports a rate of $10MHz$, which is sufficient for our purposes.

Timing Signal.

Cables used for timing go directly from the phototube into a set of *Phillips 710* Leading Edge Discriminators, physically located close to the phototube in the IR. This discriminator features simple independent threshold control of the signal. The discriminated signal is transferred into the FE Hut and into another set of *Phillips 710* Leading Edge Discriminators. Each of these modules has one input and two outputs, which are distributed as follows:

1. One output goes into the *LeCroy 3412* CAMAC Discriminators, which are used as a triggering electronics and have a 16 channels programmable delay assigned to it. Output of this delay goes into the *LeCroy 4532 MALU* – "*MAjority Logic Unit*". This unit calculates multiplicity from all its logic channels and presents the result as a current proportional to the number of inputs and is used to form a trigger for the event selection.

2. The other output of the *Phillips 710* Leading Edge Discriminators goes into the *Phillips 7186 TDC* unit and forms a timing signal for Beam-Beam Counters with a $25psec - per - channel$ resolution.

3.4 Trigger and Data Acquisition.

In this section I will describe in some general detail the trigger for BRAHMS, and the Beam-Beam Counters role in forming the level0 trigger, in particular. More details about trigger design will be given in **Sec. 4.1.3**. The basic description of the DAQ system also will be given.

Trigger.

Multiple trigger levels are required for BRAHMS. Let me define, name and characterize these levels:

Trigger : is used to select "good" events and to suppress background events as efficiently as possible [33].

Level 0 The Beam-Beam Counters will provide high efficiency and $\sim 2cm$ vertex resolution and start the triggering system and the integrated electronics.

Level 1 Multiplicity Tiles of the Centrality detector will provide a 10% centrality cut and

SPEC trigger is provided by the Forward Spectrometer's Hodoscopes and Drift Chambers

In designing a trigger for the experiment, one should first decide on a physical criterion for the events to record. Trigger electronics should accept events only if they appear within a narrow time window ("*gate*"). There exists a whole classification of triggers, based on different criteria:

- track multiplicity, based on the direction or momentum of particles;
- type of particle (neutral particles, charged hadrons or leptons);
- deposited (like BRAHMS ZDC) or missing energy;
- interaction point (vertex), and so on ...

Fig. 3.17 shows simplest scheme for the BRAHMS level0 trigger implementation. A more detailed design as well as explanations will be given in **Sec. 4.1.3**.

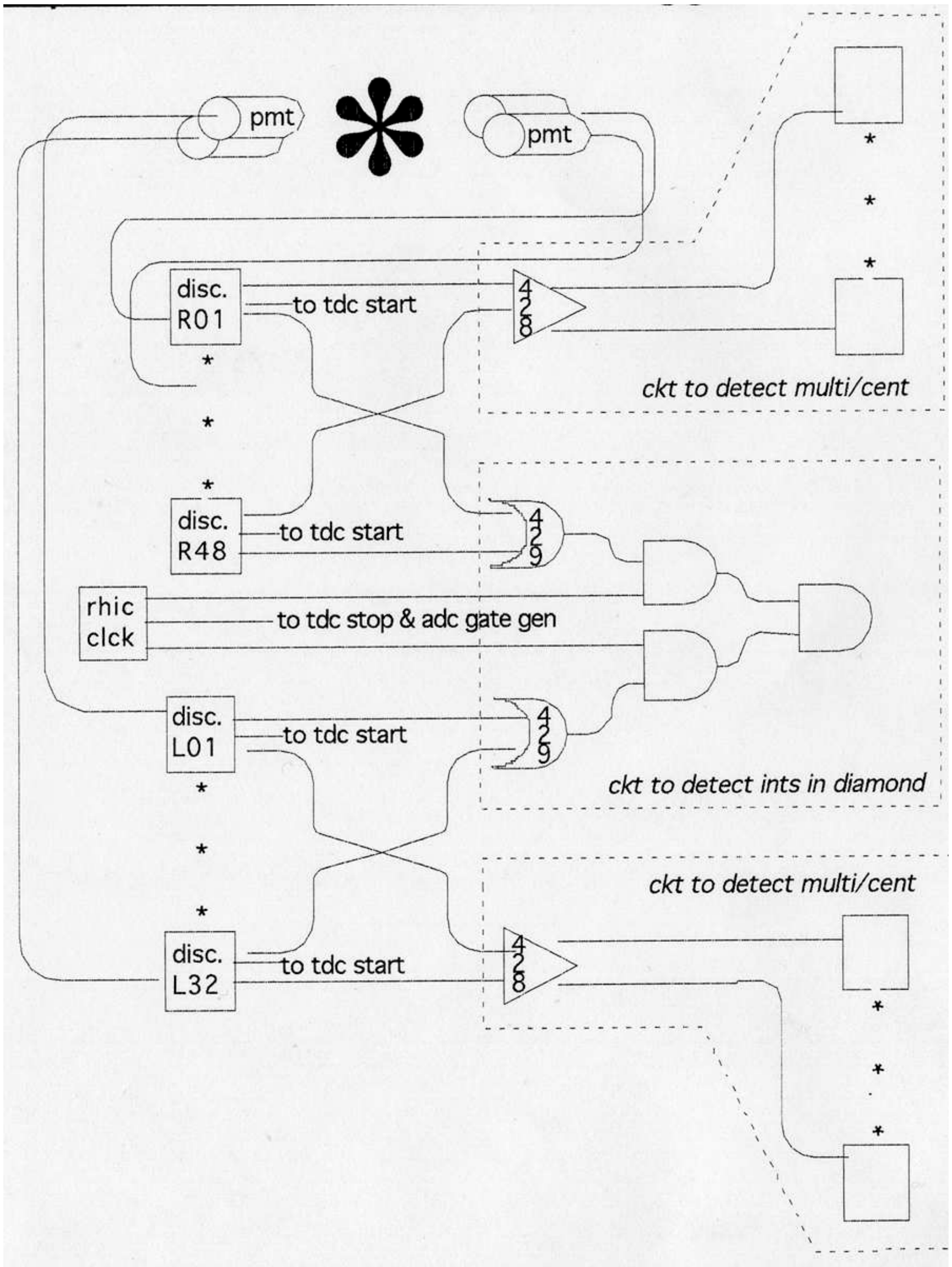

Figure 3.17: BRAHMS Level0 trigger. Simple Scheme.

Data Acquisition.

> *Data Acquisition (DAQ)* : process of gathering and calibrating raw data from different parts of the detector and storing it on permanent storage media from where it can be centrally processed off-line [36].

The communication standard for BRAHMS DAQ system, as well as for most other experiments is IEEE VMEbus industrial standard

The next stage of this thesis and describe the main design aspects of the Beam-Beam Counters.

CHAPTER 4

DESIGN and COMMISSIONING

In this chapter I would like to describe the Beam-Beam Counters in more detail, starting with the history of their original design. Then I will say a few words about the construction and computer simulations of their different parameters and finish with the results of the "*Test Beam*" of Summer'99 and "*Commissioning Run*" of Summer'2000.

4.1 Original Design.

As was mentioned above, the design constraints on the Beam-Beam Counters system for BRAHMS are dominated by the need for a good timing start for the spectrometers. Two arrays (Left and Right) were deliberately placed on each side of the Interaction Region such that they subtend a small angle for the produced particles ($\theta_{lab_{min}} = 1^o$) and high pseudorapidity $|\eta|_{max} \simeq 4.7$. This geometry favors detection of the $\beta = 1$ particles and can provide a timing start with a reasonable number of modules. Two kinds of tubes are used in Beam-Beam Counters:

Small Tube:	$3/4in$	Hamamatsu $R3478$ fast timing tube
Big Tube:	$2in$	Hamamatsu $R2083$ fast timing tube

The Left array has 44 modules, 36 of them are Small Tubes and 8 are Big, while Right Array has 35 modules in total with 30 Small and 5 Big ones. Each module has a lucite Cherenkov radiator, attached to the photomultiplier face.

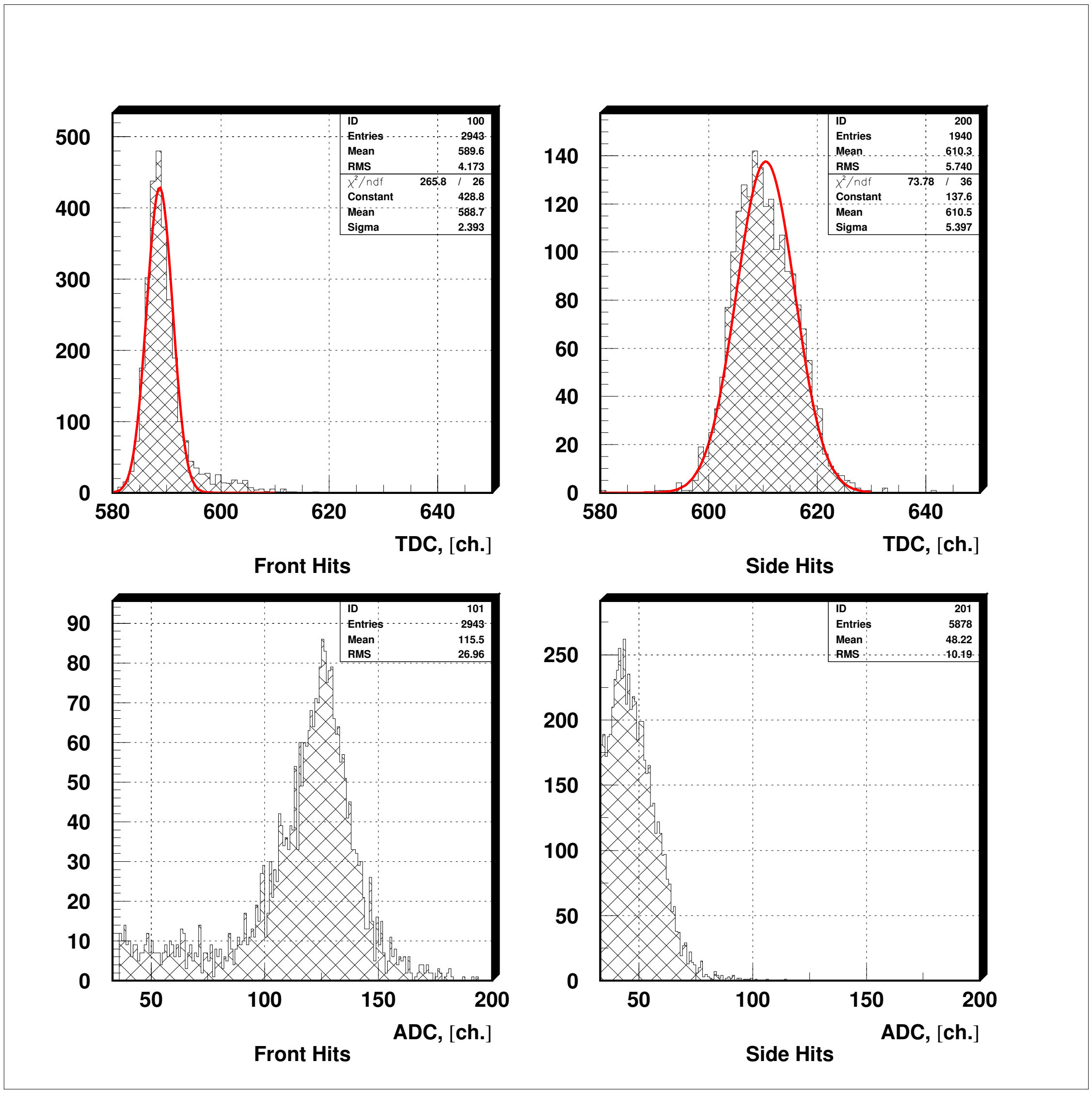

Figure 4.1: Test-Beam Studies of the phototubes prototypes. Front and Side tube's location with respect to the test beam.

Fig. 4.1 shows the phototube' prototype performance in the test beam. Two phototubes with the $4cm$ lucite radiator attached were tested in two positions:

- Facing the test-beam – two left panels of **Fig. 4.1** and
- Sideways to the test-beam – two right panels of **Fig. 4.1**.

The top two panels of the figure show the timing spectra of the prototype phototubes in the TDC channels. The timing resolution of the phototube can be calculated using the `RMS` of the Gaussian fit to the spectrum in the top-left panel (the case of the front tube location with respect to the beam):

$$\left.\begin{aligned} \sigma &= 2.4\ TDC\ ch. \\ k &= 25\ psec/TDC\ ch. \end{aligned}\right\} \Longrightarrow \ \delta t \simeq 60psec, \tag{4.1}$$

where k is a TDC conversion constant. **Appendix C** demonstrates its extraction.

This timing resolution was accepted along with the specific phototube type and the Cherenkov radiator type and length. This was our first step in the general Beam-Beam Counters design.

4.1.1 Geometrical Studies.

The original idea behind the geometrical studies was to place as many detectors as possible into areas with the maximum value of the particles hits density. We analyzed the dependence of the hits density with respect to the detector's position in the array. The CERN code GEANT was used for these purposes. It will be discussed in more details in **Sec. 6.1.1**. GEANT describes the passage of elementary particles through matter using the experiment's geometrical layout and particle distribution model as an input. Below are the main results of these studies for two different collision models from event generators FRITIOF and VENUS:

Angular dependence.

The first thing to do would be to check whether the particle distribution is azimuthally symmetric. We studied the dependence of the hit density with respect to the angular ϕ (see **Fig. 1.2**) position of the detector in the array ($x - y$ plane). The circle of the closest detectors with the distance to the beam-pipe $R = 6cm$ was chosen and analyzed for the hits distribution over the circle for two different models. The precision of the detector's position in the array is $\sim 1mm$. **Fig. 4.2** is a good description of the result. The result is as anticipated and demonstrates angular symmetry for both models.

An alternative method of placing the phototubes was used. Tubes in the Left Array were placed symmetrically in ϕ, while tubes in the Right Array were placed

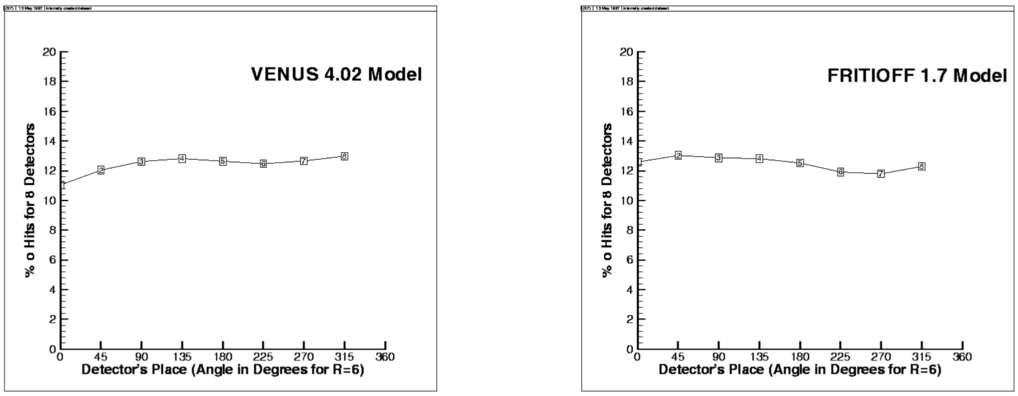

Figure 4.2: Angular distribution of relative number of hits at 6cm from the beam-pipe.

trying to occupy as many angular positions as possible, as shown in **Fig. 4.4**.

Radial dependence.

The next thing to check is the radial dependence of the hits distribution. Six detectors of the same size, but located at different distances from the beam pipe were selected. The decreasing of the particle hits density with respect to the distance from the beam pipe was studied. It was interesting to compare not only the rate of decrease for different models, but also to check the difference of this rate for the same model, but with the different impact parameter. Previous investigations were done for the case of the head–on collision with impact parameter $b \leq 1fm$. The radial dependence for two different types of collision in FRITIOF model were compared. The cases with partial ($6fm \leq b \leq 8fm$) and total ($10fm \leq b \leq 12fm$) peripheral collisions were taken. The result is shown in **Fig. 4.3**.

Our studies demonstrate that the FRITIOF model will give a faster decrease of the particle hits density with respect to the distance from the beam pipe. Also, hits density in a fully peripheral collision was found to descend faster than for the partial one. Maximum acceptable distance of the detector from the beam pipe was established. Placing our phototube at this distance would still allow us to register a reasonably big hits density in the most peripheral collisions, sufficient for the good timing.

The final decision was arrived at using an alternative approach: the Left Array tubes were located in concentric circles, while Right Array tubes were placed at as

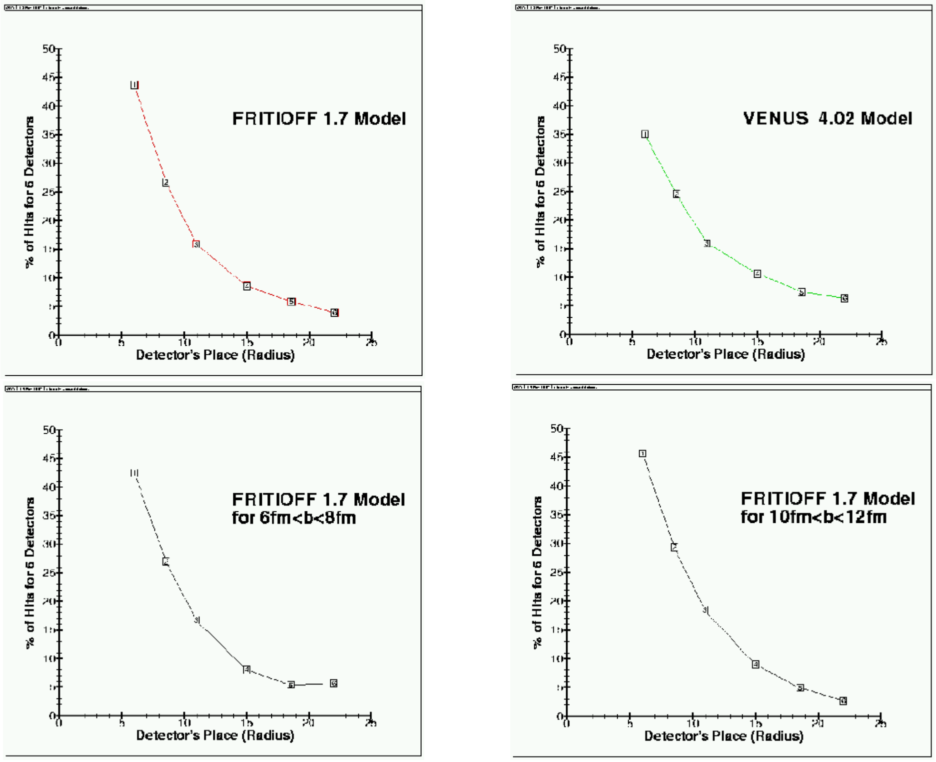

Figure 4.3: Relative hits amount radial distribution for the head-on and side collisions in FRITIOF model.

many possible radii, as possible. With such a geometry we planned to achieve several main objectives:

1. Cover the maximum possible phase space.

2. Be able to register at least one charged particle in the most peripheral event in the tubes, sitting at large θ angles in order to provide a good timing.

3. Reject most of the slow or "late" particles.

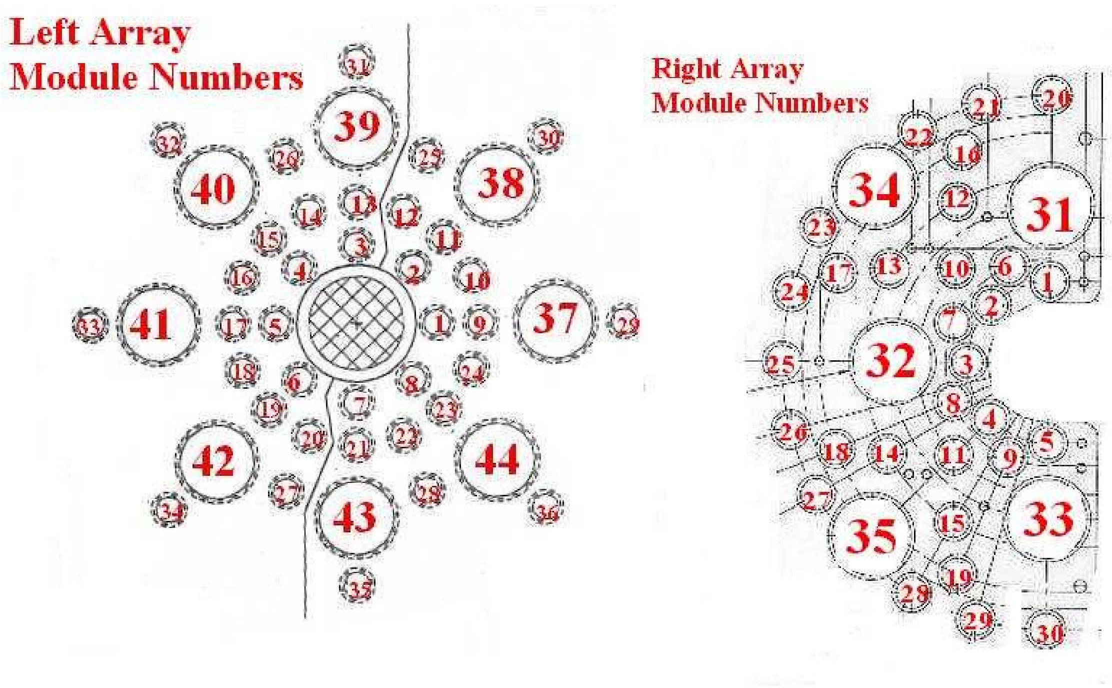

Figure 4.4: Schematic view of the Beam-Beam Counters arrays with the module numbers.

4. And at the same time to have a reasonably small event rates for the central collisions, in the tubes, closest to the beam-pipe.

5. Have symmetrical coverage of the phase-space.

6. Have a good handle on possible malfunctions by having several tubes sitting at the same pseudorapity value.

The final scheme of the Beam-Beam Counters arrays is shown in **Fig. 4.4** with module numbers on the face of the tubes. These are the reference numbers used in the analysis. The distance from the individual tube to the beam-pipe can be found in **Appendix B**.

Location of the Arrays.

The other task was to identify the best position for the array locations along the beam-pipe. Four main distances were tried for the symmetrical picture of arrays. They were located at ±1.0, ±1.5, ±2.4 and ±3.0 meters from the vertex. Three important features were investigated: hits density, time-of-flight and, the ratio of the hits made by electrons and positrons to the rest of the events (it is believed, that e^+e^- pairs come mostly coming from the γ conversions in the beam-pipe creating most of the background). An additional question was to locate the origin of the secondaries. This is important because they do not carry timing information and could be a problem for accurate timing measurements which rely on primary particles. **Fig. 4.5** shows the time-of-flight distribution of all charged particles generated in the collision (empty bins) in comparison with the e^- e^+ pairs (black bins) for different location of the arrays. It can be easily seen, that

- the time-of-flight is directly proportional to the distance from the vertex, and
- the ratio of the secondary particles (mainly $e^+ - e^-$) to the total number of charged particles gets bigger with the distance.

The final decision was to place our arrays at $220cm$ from the vertex, which would give us a good timing, a reasonably low rate of the primary hits and at the same time a reasonably low background rate.

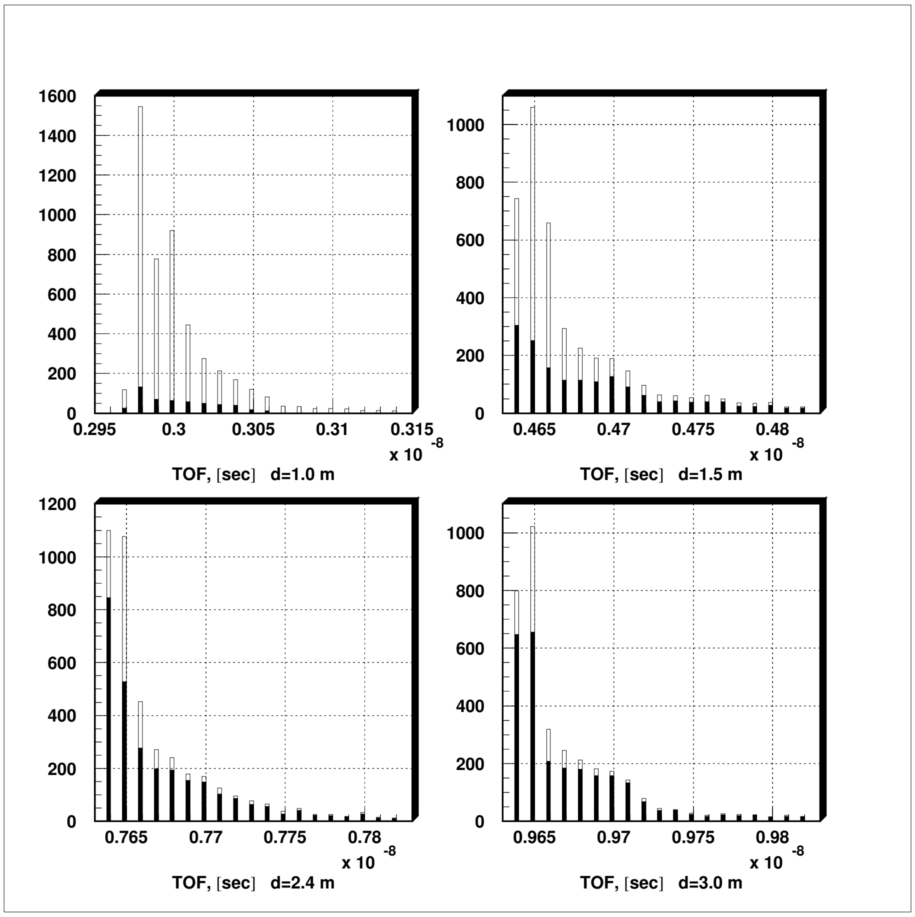

Figure 4.5: Time–of–Flight ratio of e^+, e^- hits (black bins) with respect to all charged particles (empty bins) for different array locations.

Impact parameter.

The other step was to analyze occupancy as a function of impact parameter for the array located at $220cm$ from the vertex. The main concern here was to make sure, that we will be able to register even the most peripheral collisions in the outermost ring of the detectors. As anticipated, the occupancy decreases with

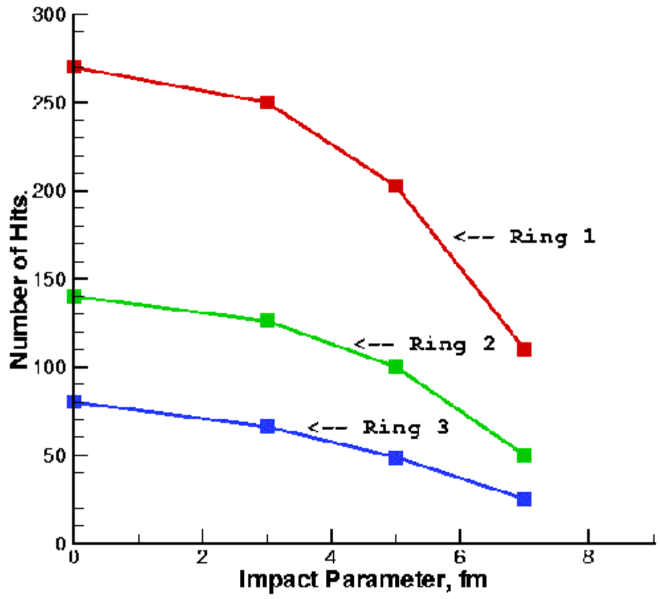

Figure 4.6: Occupancy as a function of the impact parameter for different detector's locations.

the increase of the impact parameter. **Fig. 4.6** exhibits the occupancy *vs.* impact parameter for different detector's locations.

"Ring 1" on the picture is the closest to the beam–pipe and "Ring 3" is the farthest. As you can see, even the outermost detector will register at least one particle hit in a case of the most peripheral collision (30 events were generated, so the numbers on the vertical axis of the graph should be divided by 30). That means, that our array locations were chosen reasonably.

4.1.2 Hardware Studies.

A series of hardware studies were carried out in order to improve the Beam-Beam Counters performance.

Cherenkov radiator length.

The length of the Cherenkov radiator in front of the photomultiplier was the first topic to investigate. The length determines the quantity of Cherenkov light. This issue was studied in the test beam with phototubes that were glued to different length of UV transmitting (UVT) or absorbing Cherenkov radiators. **Fig. 4.7** shows the results of these studies through the spectrum of the energy deposited in the attached phototube. It can be easily seen in the bottom panel of the picture, that $4cm$ of the UV transmitting radiator performed with the best energy resolution of $\Delta E/E \simeq 0.155$. That is why, lucite was chosen for the radiator material, since the energy resolution achieved with the $4cm$ UV transmitting lucite radiator was best.

The length of the radiator will also effect the timing of the detector. The longer the UVT, the more light will be received by the phototube, the better the timing. But at the same time, the longer radiator creates a lot of "late" events, which could be bad for a timing (there will be a lot of light coming from hits on the side of the UVT). **Fig. 4.8** shows the location of hit origins for two different UVT sizes for the small tubes. It can be easily seen, that most of the hits are coming from the 2 or $4cm$ area, occupied by the lucite radiator. These particular studies were made for the case of Fe beam-pipe and $210cm$ as the array's distance from the

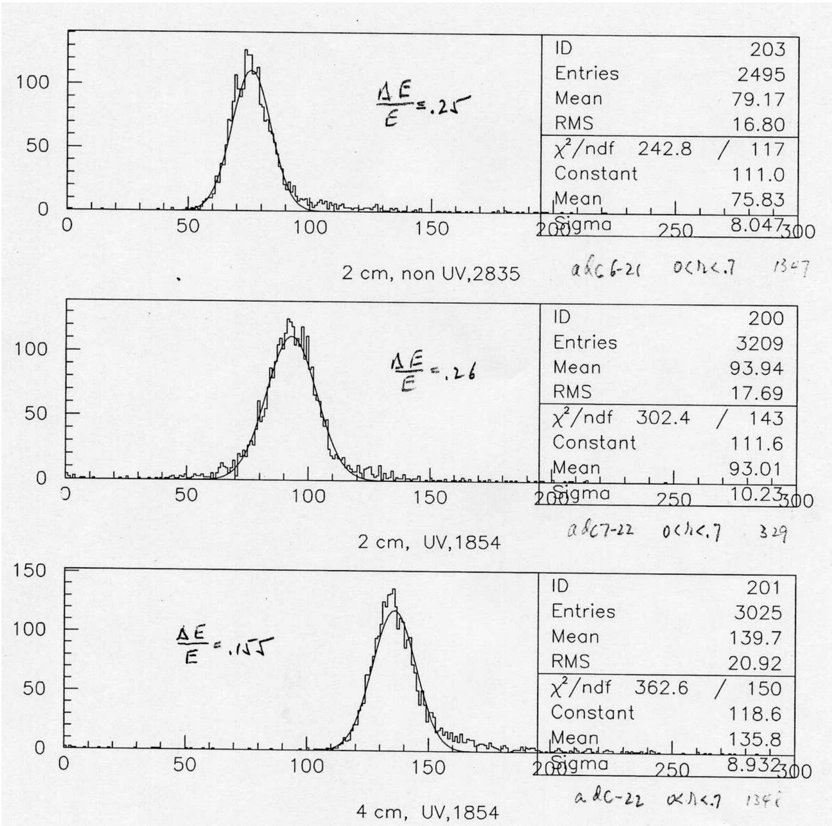

Figure 4.7: Cherenkov radiator study in the Test Beam.

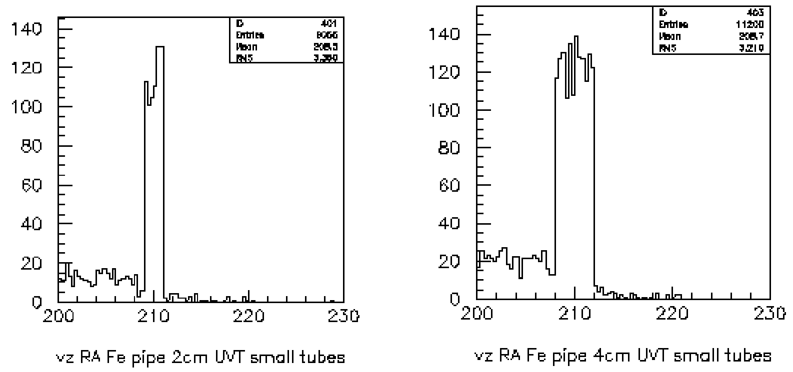

Figure 4.8: Hits origins for different UVT sizes (small tubes).

origin.

The final decision made was to place $4cm$ UVT on the small tubes and $3cm$ on big ones.

Beam–pipe.

In the original Conceptual Design Report (CDR) the beam-pipe was designed to be made partially of Be, placed symmetrically $\pm 1m$ about the vertex, and the reminder of Fe. The idea was to reduce number of secondary particles near the collision vertex. Secondaries in this context are particles coming from the beam–pipe itself. The secondaries are least for a beam-pipe fabricated entirely from Be, but this would be very expensive. Fe is cheap, but produces a lot of secondaries. The amount, in turn, depends on the thickness of the Fe walls of the beam–pipe.

- ***Be* length and *Fe* thickness.**

  This section provides an analysis of the time of flight of the particles as a function of the walls (Fe) thickness and of the length of the Be section of the beam–pipe. We used two lengths of Be: $1m$ and $1.5m$ and two Fe thicknesses: $1mm$ and $0.5mm$, combining them with each other. **Fig. 4.9** shows time-of-flight spectra for e^+e^- (shaded area) compared with the time-of-flight for all charged particles (empty bins) for three different beam-pipe configurations. As anticipated, the thinner walls and longer Be section, the better the results in terms of the secondaries-to-primaries ratio. The contributions of e^+e^- pairs is reduced with the longer Be section.

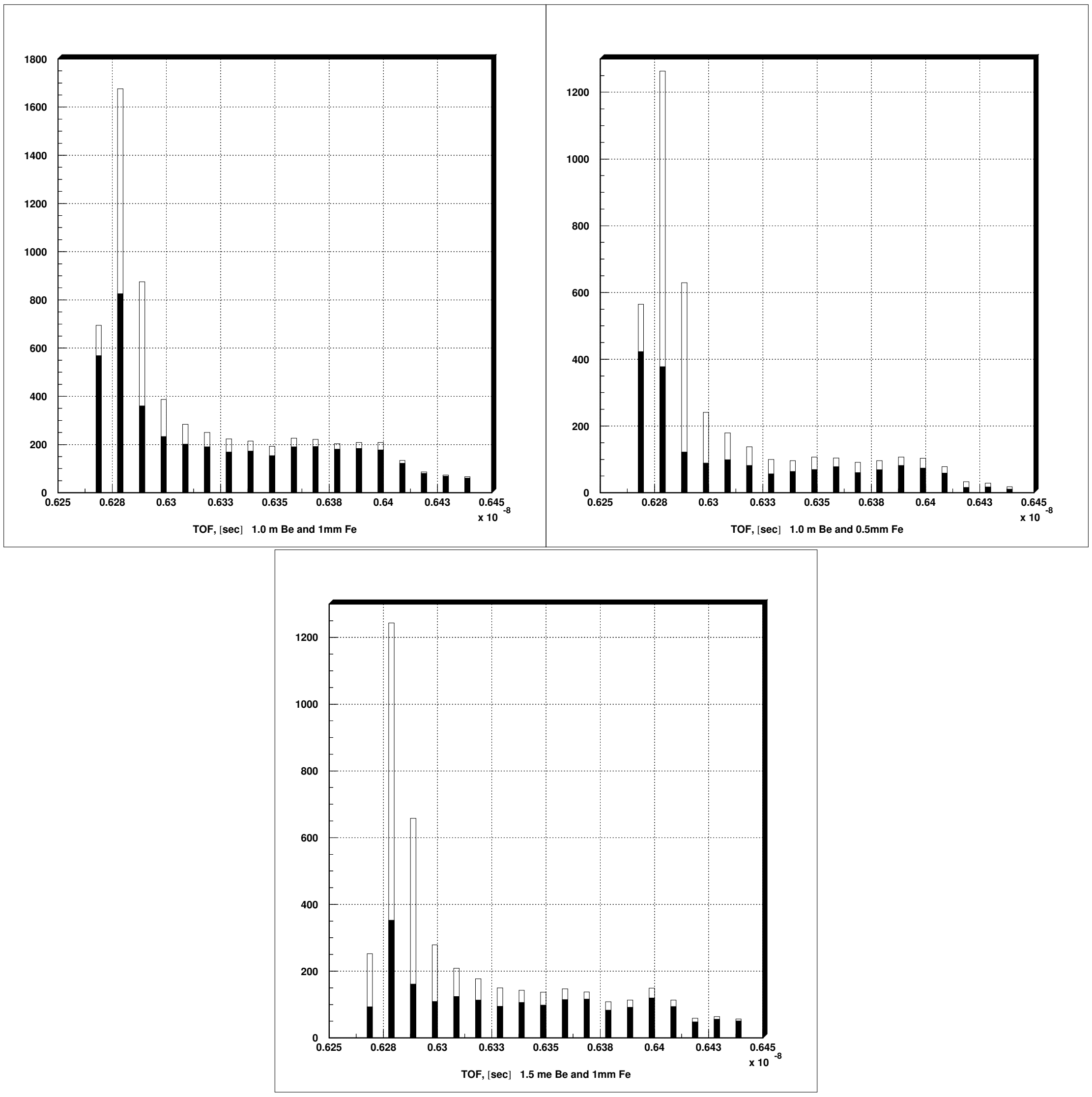

Figure 4.9: Time-of-Flight for e^+e^- (shaded area) as compared to the time-of-flight for all charged particles (empty bins) for different beam-pipe configurations. Particular configurations can be seen under the pictures.

But again, the length of Be is restricted by funds, and the thickness of Fe is also restricted by the firmness requirements. It has to be thick enough, to keep the cylindrical shape against the external atmospheric pressure and the vacuum inside. But the solution turned out to lie in an entirely different direction.

- ***Be* – *Al* beam–pipe.**

  Alluminum was substituted for iron. Al gives far fewer secondaries than Fe! **Fig. 4.10** shows a comparison between Al and Fe usage. The top four panels show the origin of hits distribution with respect to the distance from the Interaction Region to the Left or Right Array. It can be easily seen how the Fe part of the beam-pipe acts as the major source of hits. On the other side, the Be section produces almost no particles at all and the Al part produces them much fewer than the Fe one. In the bottom two panels of **Fig. 4.10** we have the time-of-flight spectrum comparison between the two beam-pipe configurations. And again, the transparent bars represent all charged particles, when the filled ones are for the $e^+ - e^-$ pairs produced in the secondary interactions.

  The improvement in the number of secondaries and in the time-of-flight is apparent for the case of the Al beam-pipe. So, the final decision was to use an Al–Be beam pipe.

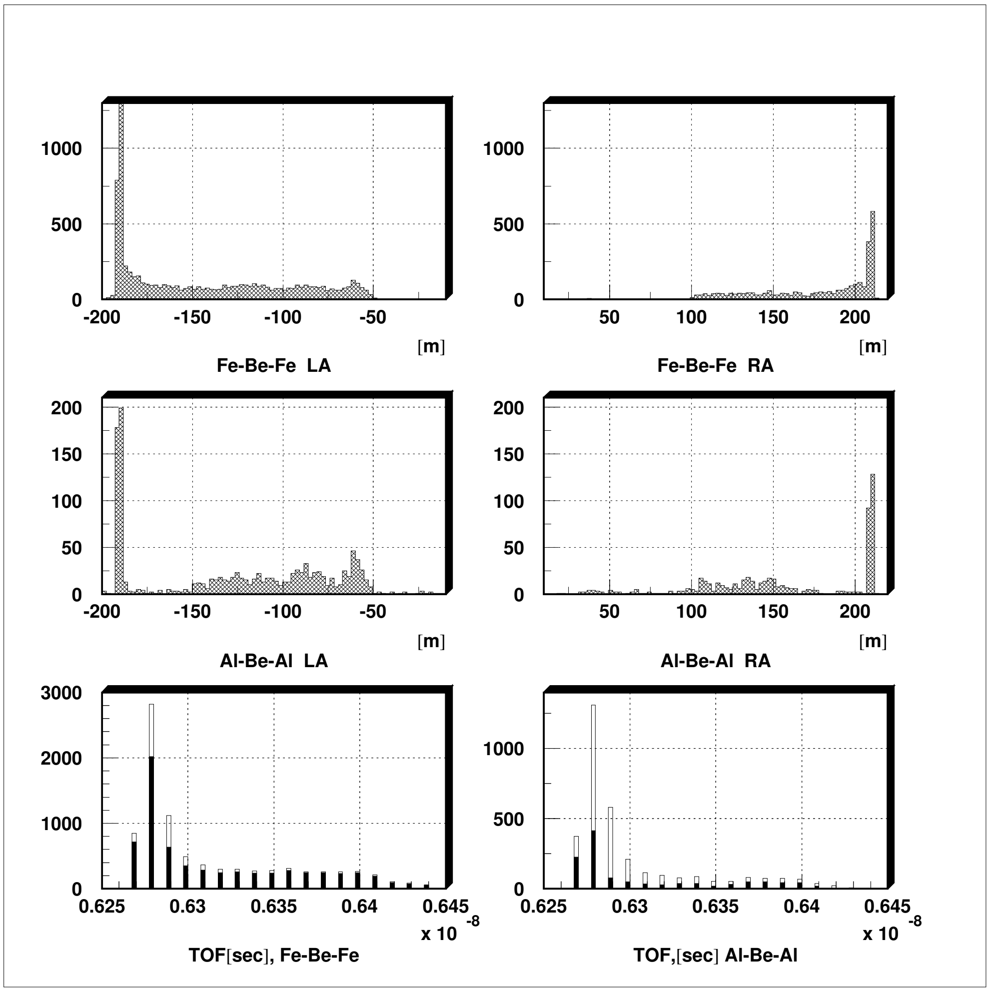

Figure 4.10: Beam–pipe structure. Z coordinate of points from which hits originate. Time–of–Flight for e^+e^- with respect to the other particles.

General shape of the array.

A final concern was a design layout for the array holder. All the counters must point with some small angle towards the vertex, so their directions would form a cone whose apex is the vertex, as shown in **Fig. 4.11**. Simple calculations were

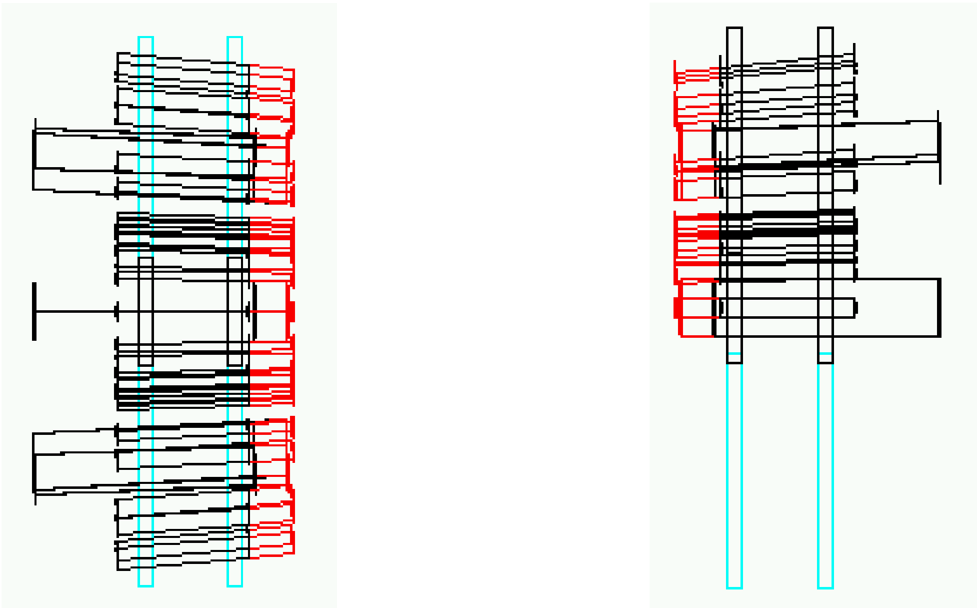

Figure 4.11: Schematic topview of the Beam-Beam Counters arrays.

performed to extract the required angles based on the distance of the tube from the beam-pipe and distance of the whole array from the vertex. The detectors are fixed in their position by two plates separated by a small distance. The plates have holes at slightly different radii. These holes, in turn, are filled with "*O - rings*" to keep each individual tube in place. Details can be easily seen in **Fig. 4.11**: lucite radiators in front of the tubes; array holders, and Big Tubes are longer than the Small tubes.

4.1.3 Trigger Studies.

One of the major roles the Beam-Beam Counters have to play in BRAHMS is to serve as a zero level trigger. **Fig. 4.12** shows an outline of the basic trigger logic.

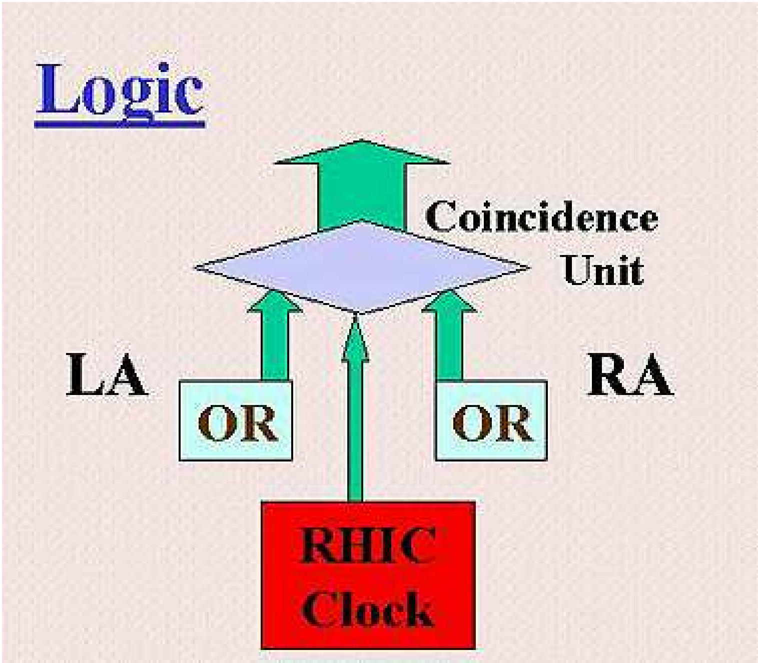

Figure 4.12: Beam-Beam Counters Trigger logic outline

A "`START`" signal will be given to the experiment when a "*Coincidence Unit*" receives three signals at the same time: from two logical "*OR*" units, related to each of the two arrays (Left and Right); and a signal from the RHIC Clock, saying that beam entered the Interaction Region. The OR unit can be set to give an output if some desired number of tubes in the Left and in the Right Array are hit simultaneously. This number depends on the kind of event one wants to detect.

A good trigger must not only be formed as fast as possible, but also has to be able to select good events and suppress those reactions which are not interesting. In our case it would have to distinguish collisions between two gold nuclei from possible collisions of a beam particle with a residual gas molecule (say, O_2) in the beam-pipe or from the interactions of beam particles with the walls of the beam pipe. This problem was addressed with some computer simulations and simple calculations.

Simple Estimates.

I want to start with some estimates of the coincidence rates in the case of a

- **Central $\boldsymbol{Au - Au}$ collision.**

  The number of reactions per time interval is usually defined by

$$Rate\ of\ Collisions = \mathcal{L} \cdot \sigma, \tag{4.2}$$

where $\mathcal{L}$ – Beam Luminosity and σ – Collision Cross Section [33].

In Relativistic Heavy Ion Collisions with storage rings particles are injected in several bunches simultaneously in opposite directions. The luminosity $\mathcal{L}$ depends on several parameters such as number of particles per bunch N_b, the number of bunches in each beam k_b, the distance between bunches or the revolution frequency f and the beam radii of the bunches a at the crossing point:

$$\mathcal{L} = \frac{N_b^2 \cdot f \cdot k_b}{4\pi a^2} \tag{4.3}$$

RHIC will be injecting $k_b = 60$ bunches with $N_b = 10^9$ particles per bunch. RHIC's circumference is $C = 3.84km$ and assuming that the bunches are moving close to the speed of light we can get, that $f = k_b \cdot c/C \simeq 4.7 \cdot 10^6 Hz$.

Or, we can just use RHIC's official design number of $\mathcal{L} = 10^{26}\frac{particles}{cm^2 \cdot sec}$.

For the collision cross section estimates let's consider collisions of two Au beams with impact parameter of $R_{Au}/2$, then the geometric cross-section is given by

$$\sigma = \pi(2 \cdot R_{Au}^2), \qquad \text{where } R_{Au} = 1.2 \cdot (A_{Au})^{\frac{1}{3}} = 1.2 \cdot \sqrt[3]{179} \simeq 6.76fm.$$

That makes $\sigma \simeq 5.7bn$. Final substitution into the **Eq.(4.2)** predicts result of 570 expected collision events per second. Thus, in the case of the central collision our coincidence rate will be equal to $\boxed{570Hz}$. Next consider the case of beam-gas collisions.

- **Beam – Gas ($\boldsymbol{He^4}$) collisions.**

Possible coincidence events can arise from accidentals due to the collisions of both of the beams with the residual gas in the beam pipe. Let me take He^4 as an example. In this case I have to use different definitions:

$$Random\ Coincidence\ Rate = R_{blue} \cdot R_{yellow} \cdot t_{res}, \tag{4.4}$$

where R_{blue} and R_{yellow} – Beam-Gas "Singles" Collision Rate of the Blue and Yellow beams respectively[3], and t_{res} is the time resolution between the consecutive bunches.

Time t_{res} can be easily calculated from the revolution frequency f, simply as $t_{res} = 1/f \simeq 213nsec$. Then we have to use different following formula for the

[3]RHIC calls Blue a beam which goes in the direction of the Beam-Beam Counters Right Array

individual beam-gas collisions rates. We use Blue beam as an example:

$$R_{blue} = F \cdot \sigma \cdot N_{residual} \cdot l \quad (4.5)$$

where

– F – flux of particles, or number of the incoming particles per second:

$F = N_b \cdot f \simeq 4.7 \cdot 10^{15} particles/second$

– σ – collision cross section:

$$\sigma = \pi (R_{He^4} + R_{Au})^2$$

and using the fact, that $R_{He^4} \simeq 2.5 fm$ one can easily get, that in our case $\sigma \simeq 2.7 bn$

– $N_{residual}$ – number of residual He^4 particles inside the beam pipe per cm^3. We can estimate this value by using the following relation:

$$\frac{N_{residual}}{P_{residual}} = \frac{N_{atm}}{P_{atm}}, \qquad N_{atm} = \frac{N_{Avogadro}}{22.4l}$$

The beam pipe residual pressure is claimed to be $P_{residual} \simeq 10^{-9} Torr$. So after some simple calculations one can get, that $N_{residual} \simeq 35.2 \cdot 10^6 particles/cm^3$

– l – length of the possible beam-gas interaction region, $l \simeq 10^3 cm$.

Substituting into **Eq.(4.4)** and **Eq.(4.5)** we find that in a case of the beam collision with the residual gas in the beam pipe we expect to have the beam-gas "singles rate of the order of $\boxed{350Hz}$ and the accidental coincidence rate of the order of $\boxed{0.04Hz}$.

Our conclusion is that accidental coincidence events are negligible. That means, that a trigger based on the coincidence of only one particle detected in each array, would reject possible beam-gas events. This type of trigger, "one particle in each array" is called a "*Minimum Bias*" trigger.

GEANT Simulations.

Setting the trigger for the detection of a "*Minimum Bias*" events to get rid of the background and scraping events leads to a loss of some "good" events, also represented by only one hit in each array. GEANT studies were carried out to answer this question of loss. **Fig. 4.13** shows the results of GEANT simulations of 3 kinds of collisions:

1. Central collision of two Au beams.

2. Collision of 2 Au beams with minimum bias.

3. Collision of one Au beam with the residual O_2 gas in the beam-pipe.

The percentages shown in the panels in **Fig. 4.13** represent the fraction of "good" events which will be rejected for a particular chosen cut in the beam-gas collisions. One can see, that "*5 hits*" cut will eliminate almost all the background, but simultaneously reject about 12% of the Minimum Bias collision events!

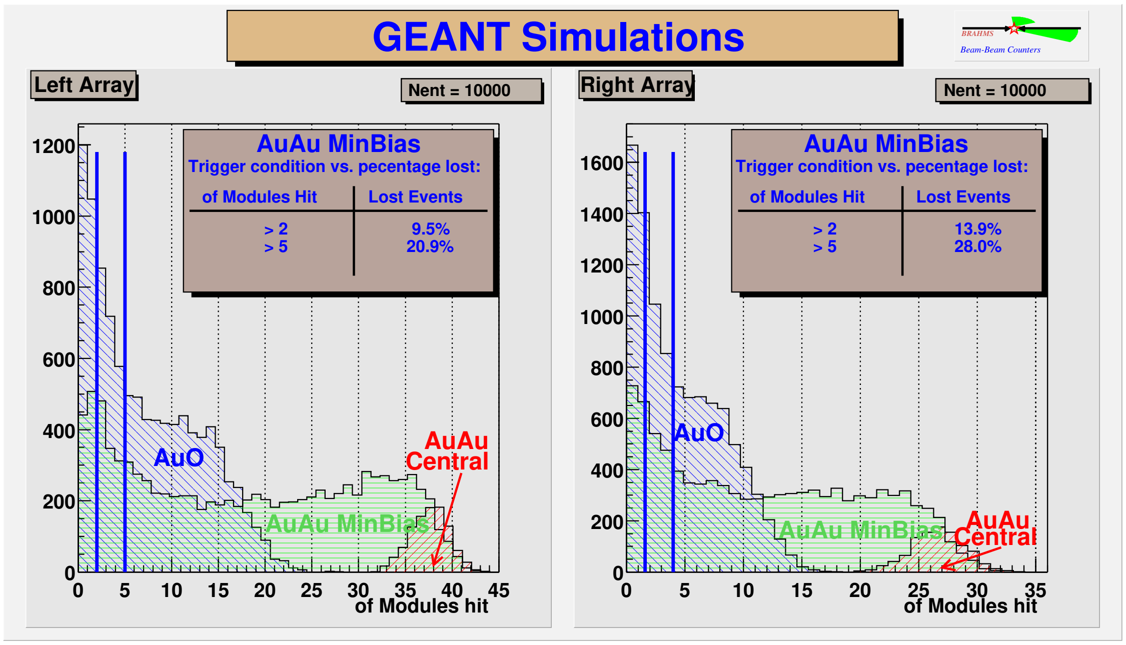

Figure 4.13: Beam-Beam Counters multiplicity for different kinds of GEANT simulated collisions. Vertical axes represents number of hits, while horizontal shows number of modules hit in the array.

Again, the main concern here was to identify the trigger which will eliminate the Au beam – residual gas collisions, and identify collisions between the two gold beams. **Fig. 4.13** is plotted out of scale for simpler analysis. It was decided to use 2 modules in each array as a trigger. It can be seen from the figure above, that with this setting only a very small number of “good events” are lost.

So, everything was ready for the real experiment. The next section describes our first data taking.

4.2 Commissioning.

"*One must learn by doing the thing; though you think you know it, you have no certainty until you try.*"

/Sophocles/

This section consists of the first experimental results, achieved during the RHIC commissioning runs. It is split into two main parts:

- Beam-Beam Counters performance in the very first RHIC "*Test Beam*" of Summer 1999;
- and First data during the RHIC commissioning run of May – July 2000.

4.2.1 Test Beam (Summer 1999).

The RHIC Test Beam in Summer'99 provided us with the first real test of our detector system. No real collisions were achieved during this time, but instead two independent particle beams circulated in the collider's rings. Again, the "*Blue beam*" of gold nuclei was moving in the direction of our Right Array and "*Yellow Beam*" in the direction of our Left Array. As a result, data saved during some runs have been identified as a "*good runs*" for Beam-Beam Counters commissioning. The main criteria for this classification are:

- reasonable beam storage time;
- reasonable beam intensity values;
- sufficient number of events triggered by Beam-Beam Counters.

These good runs were merged and they served as a major data source for our analysis. Since no real collisions were achieved, only ADC spectrum analysis is worth mentioning here.

Short explanation is in place here. It was mentioned many times how the number of particles hitting our detector is crucial to the charged particle multiplicity analysis. In GEANT simulations one can easily access that information just by extracting the number of particles directly from the simulation. In real life the ADC spectrum carries the multiplicity information converting the analog energy of the particle deposited in the Cherenkov counter into the digital ADC signal. Thus, a two particle hit should have the ADC signal doubled with respect to the single particle hit. Statistical fluctuations in the multiplication process in the photomultiplier makes total ADC signal to be binomially distributed for the n particle hit with `MEAN`$= n$ and `RMS`$= \sqrt{n}$.

Fig. 4.14 shows raw pre-calibrated ADC spectra for all modules in the Right Array for the Blue Beam. Although it does not contain any scientific information, it does constitute the first demonstration of the Beam-Beam Counters performance. The number of the distinguishable peaks on the histogram corresponds again to the number of particle hits for the phototube. This allowed us to conclude, that some particular modules in the Right Array registered more charged particle hits than others. Mainly: Right Modules 1-3, 6, 7, 10, 12, 13, etc.

If we take a look at the modules location scheme in **Fig. 4.15**, we can easily see, that these modules are located in the upper-left corner of the Right Array (marked in the picture). This implies that the beam was not properly centered

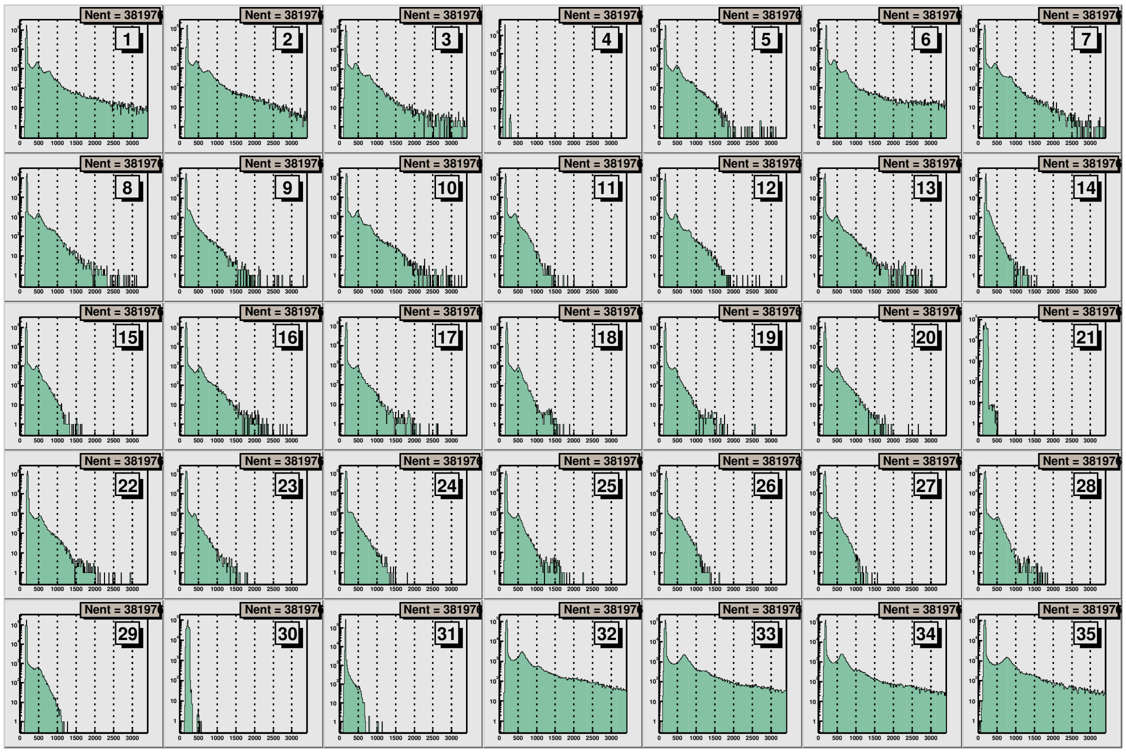

Figure 4.14: Right Array ADC spectra. Vertical axes shows number of entries and horizontal gives ADC channels.

and that all detected particles mainly come from the beam scraping the beam-pipe somewhere far behind the Left Array. This was confirmed later by the results and analysis of the Multiplicity Tiles, located cylindrically around the vertex.

These pictures by themselves give very little information, so these spectra had to be calibrated by the following scheme:

- Only events with Beam-Beam Trigger were selected. This trigger was set as described in **Sec. 4.1.3** to have at least two Big Tubes hit within a wide time range of $\sim 15nsec.$;

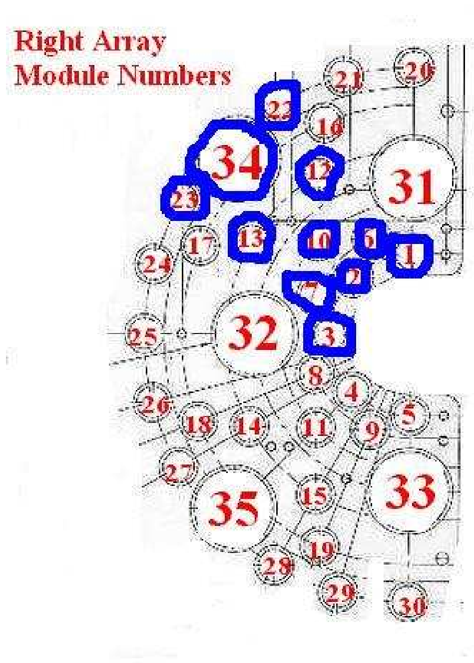

Figure 4.15: Scheme of the Beam-Beam modules locations in the Right Array.

- Pedestal values due to the synchronization trigger and constant noise background were identified as discussed in the next chapter, and subtracted;
- ADC values were divided by the Gain values, which represent the phototube response to one particle hit. These values were identified earlier in the Lab studies for each particular module. Thus the alignment of individual ADC spectra of different tubes was accomplished[4].

Fig. 4.16 shows calibrated ADC spectra for some modules in the Right Array for the Blue Beam.

[4]**Sec. 5.1** demonstrates how the Gain value was later extracted form the real data.

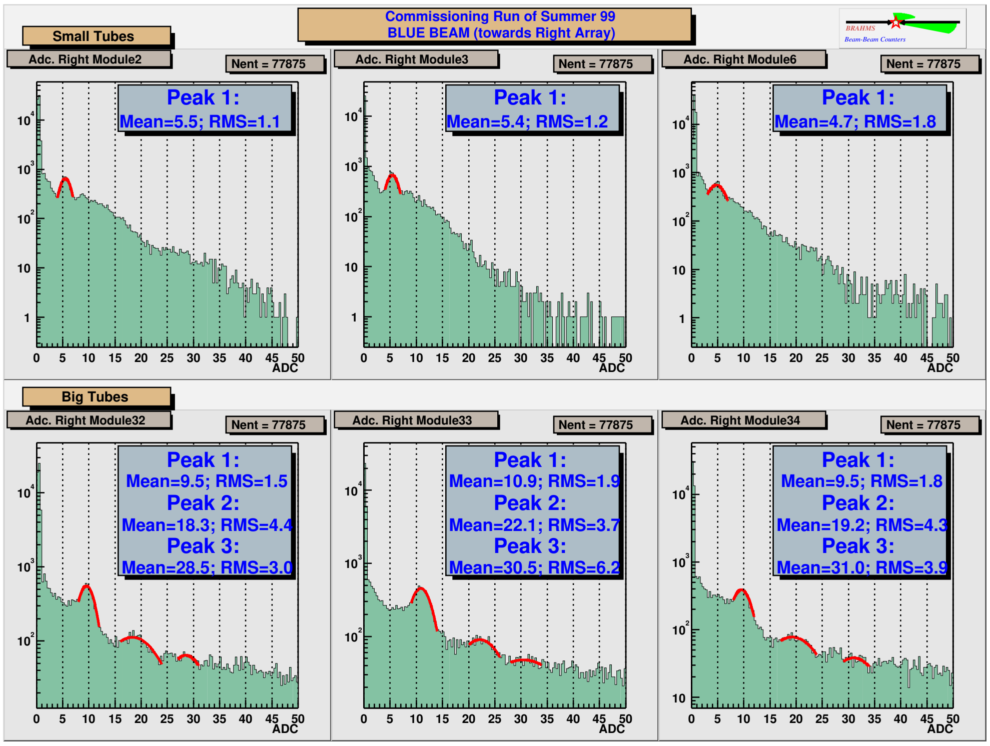

Figure 4.16: Selected ADC calibrated spectra in the Right Array. Top raw shows Small tubes and bottom raw – Big Tubes.

These figures demonstrate, that some tubes have really experienced 2 or 3 hits. Moreover, the location and width of theses peaks confirms our conclusion, based on the GEANT studies, that Beam-Beam Counters should be able to detect about 7– 9 particles. Another thing worth mentioning here is the fact, that these hits deposited same amount of energy for different tubes, which validated our laboratory measured gains that were carried out for calibration purposes.

The pictures presented on the previous pages demonstrate our ability to provide some rough charged multiplicity estimates for the gold-gold collisions in the BRAHMS experiment at RHIC.

Finally we conclude on the basis of the RHIC "Test Beam" period, that the Beam-Beam Counters will be able to serve as a zero–level trigger for BRAHMS, to identify collisions for RHIC and also to provide some rough preliminary estimate of the charged particle multiplicity.

4.2.2 Collision Triggers.

As it was mentioned already in **Sec. 3.4**, several triggers have to be employed in order to determine the collision event. The Beam-Beam Counters played an integral role in several of them. All triggers pursued the same goal of identifying collision and rejecting background events, like beam-gas collisions of the Au beam with residual gas in the beam-pipe. This was achieved through the coincidence of two signals in devices located on both sides of the Interaction Region. The Zero Degree Calorimeters (ZDC) and the Beam-Beam Counters are appropriate devices for this purpose. **Table 4.1** summarizes the characteristics of the various triggers.

The principal difference between these triggers is the "*Overlap*", or the "*Gate Width*", which not only determines whether a collision has occurred, but can also separate different classes of collisions. For example, the physical characteristics of the ZDC, as mentioned in **Sec. 3.2.1**, allow it to serve as a good "*Minimum Bias*" trigger, rejecting beam-gas collisions and triggering on the most peripheral collisions,

ID #	Detectors	Coincidence of	Overlap Width	Rate
1	BBC	Any 3 Left Array and 3 Right Array Big Tubes	$5nsec$	$50 - 60Hz$
4	ZDC	Left and Right Modules	$18nsec$	$140 - 150Hz$
5	BBC	3 Left Array and 3 Right Array Big Tubes	$14nsec$	$100 - 110Hz$
6	BBC	Perfectly timed 2 Left Array and 2 Right Array Big Tubes	$5nsec$	$20 - 30Hz$

Table 4.1: Collision triggers characteristics. Rates are given after the scale down.

when nuclei just brush against each other, freeing a limited number of neutrons. The Beam-Beam Counters served as a major collision trigger with $Trigger$ 6 being the most successful. It was constructed of 2 manually timed Big Tubes in both arrays with individual timing matched by the digital delay device. The time resolution for this trigger was later found to be of the order of $65psec$. A correlation of the BBC and the ZDC triggers was used to detect first collisions:

4.2.3 First Collisions (June 2000).

In the RHIC commissioning run three major goals had to be achieved:

1. Collision detection, was definitely the most important accomplishment of the commissioning period.

2. Proof of the proper timing (vertex) resolution.

3. Proof of the detector's proper operation at different beam energies.

As for the first collisions, they were detected in the BRAHMS area on June 15, 2000 by two detectors: Beam-Beam Counters and Zero Degree Calorimeters.

Two beams of gold nuclei, both beams traveling at $\gamma = 30$ collided in the BRAHMS Interaction Region (IR). For a nucleon mass $m_o = 1.67 \cdot 10^{-27} kg$ one can calculate the energy as

$$\mathcal{E}_{one\ nucleon} = \gamma m_o c^2 \simeq .94\gamma GeV$$

That makes beam energy to be of about $\mathcal{E} \simeq 28A\ GeV$ and $\sqrt{s} \simeq 56A\ GeV$. Six bunches circulated in the rings, and the Beam-Beam Counters confirmed their ability to work as a zero-level trigger by detecting the first collisions.

Fig. 4.17 demonstrates a 3-d "LEGO" plot of time differences. Axes are clearly labeled. The vertical axis represents number of entries. Both detectors are located symmetrically with respect to the expected collision vertex, so the time difference $\Delta t = 0$ represents a collision, that occurred at $z_o = 0$. The agreement of the Beam-Beam Counters and the ZDC's on "*time-zero*" allows a positive identification of a collision. Based in **Fig. 4.17** the BRAHMS collaboration claimed that first $Au+Au$ collision were detected, and this picture was published in the "*Brookhaven Bulletin*" [41].

Events on both sides of the vertex are from the particles, which did not collide, but instead, produced a signal in both arrays by hitting one of them from the back and flying all way through to the other array. This can easily be confirmed by a simple calculation. In projection on the Beam-Beam axis, the mean values of these

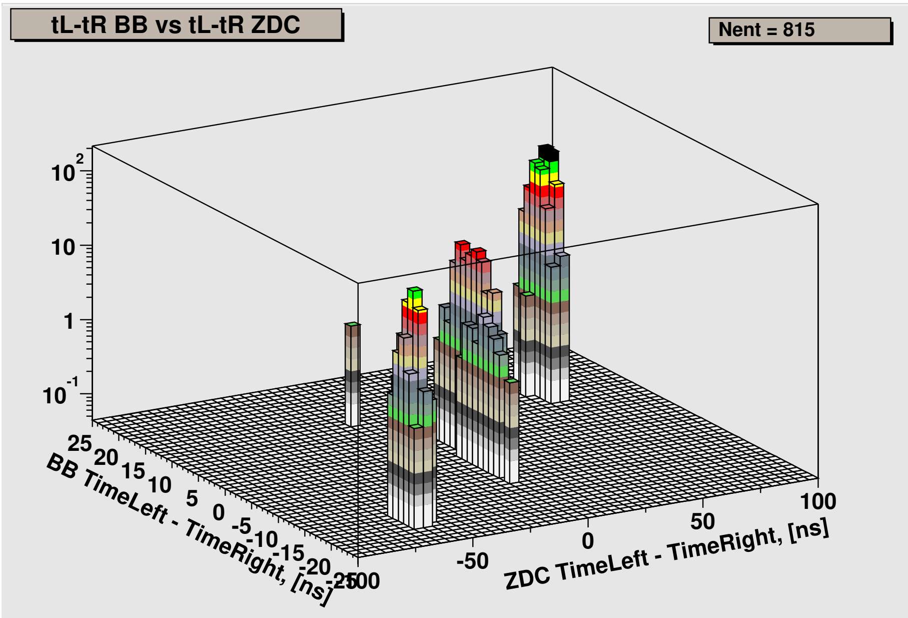

Figure 4.17: RHIC first collisions at BRAHMS. BBC Time Difference *vs.* ZDC Time Difference.

"side-bars" are located at $\pm 14.67 nsec$. One can easily determine the vertex position of these events.

As one can see in **Fig. 4.18**,

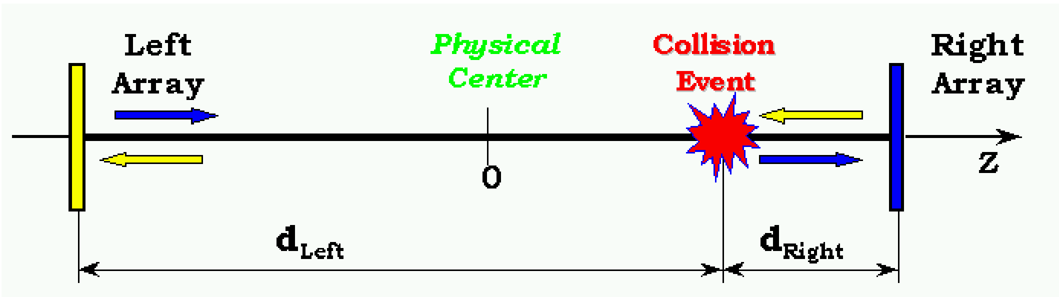

Figure 4.18: Collision event geometry.

$$\begin{cases} \Delta t = t_L - t_R \\ d_R = c \cdot t_R \\ d_L = c \cdot t_L \end{cases} \quad and \quad \begin{cases} z_{Vertex} = 219cm - d_R \\ z_{Vertex} = d_L - 219cm \end{cases} \Longrightarrow 2z_{Vertex} = d_L - d_R = c \cdot \Delta t,$$

where $219cm$ is the distance from the arrays to the physical vertex[5]. In High-Energy Physics experiments cm units are used for distance and $nsec$ for time. In these units we can write for the Vertex location:

$$z_{Vertex} = 15 \cdot \Delta t \tag{4.6}$$

Substituting $\pm 14.67nsec$ in the **Eq. (4.6)**, we get the vertex to be located at one of the arrays, which corresponds to the particle striking the back of one array and the front of the other.

The end of the commissioning phase occurred when 56 bunches of gold nuclei were inserted in the collider rings with number of particles in a bunch close to the nominal value of 10^9 and beam's energy increased to $65A\ GeV$. Thus, total CM energy was equal to $\sqrt{s} \simeq 130A\ GeV$. The Beam-Beam Counters behaved perfectly registering high multiplicity collision events with rates close to $50 - 70Hz$. The detector was operating as designed. **Fig. 4.19** shows time differences between the events registered in Left and Right Arrays of the Beam-Beam Counters and ZDC's at energy of $\sqrt{s} = 130A\ GeV$ and rates of $50 - 70Hz$.

[5] Both arrays were accidentally positioned at $219cm$ instead of the designed value of $220cm$

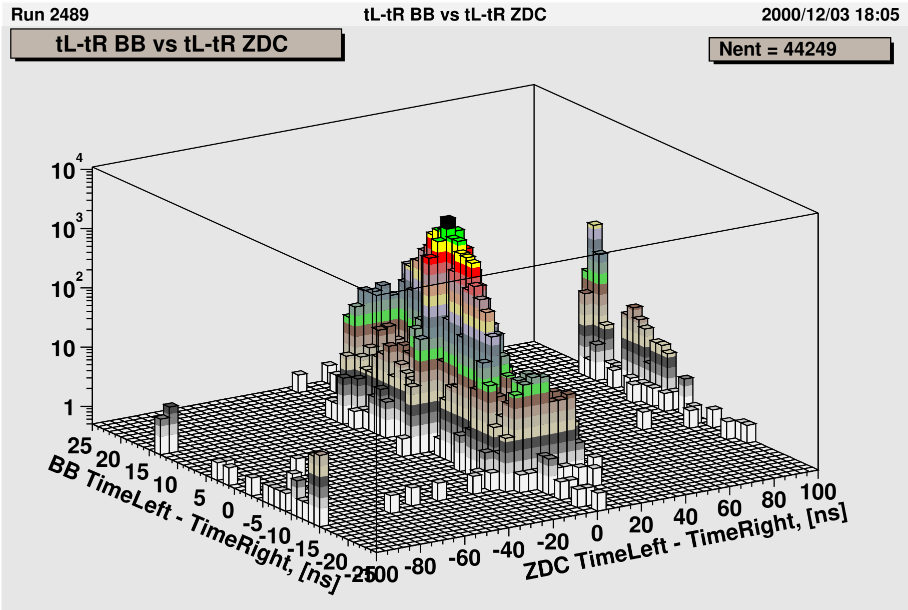

Figure 4.19: Mature RHIC collisions at BRAHMS. BBC time difference *vs.* ZDC time difference.

4.2.4 Small Tubes Saturation Analysis.

It is believed, that if the phototube is behaving as designed, then it's ADC spectrum can be considered as arising from the distribution of charged particles hits. This assumes that number of particles n is distributed with a Poisson distribution as

$$P(n) \simeq \frac{\lambda^n e^{-n}}{n!}, \tag{4.7}$$

where λ is the mean value. More detailed justification of such approach will be given in **Sec. 6.3.1**.

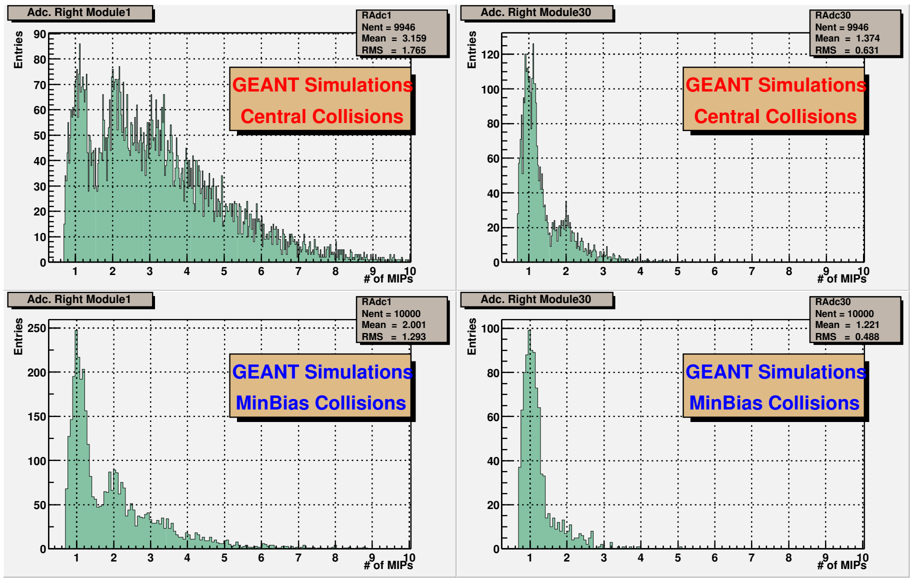

Figure 4.20: Particle hits distributions from the Monte-Carlo simulation. Small Tubes.

A Monte-Carlo simulation uses this distribution to generate a phototube's response to particles hits. **Fig. 4.20** shows examples of such distributions for the Small Tubes in the Right Array for two kinds of collisions: "*Central*" for impact parameter $b \leq 3fm$ and "*Minimum Bias*" – no restrictions on the impact parameter, or $b \leq 15fm$. The left histograms are for the phototubes with the smallest distance to the beam-pipe, while right histograms are for the outer-most tubes. All pictures show several peaks with the integer mean value, corresponding to the number of particles hitting the detector. Each peak is Gaussian with $\sigma = \sqrt{n}$, where n is number of hitting particles. This is what happens in a "perfect world".

The experimental ADC spectra for the Small Tubes are shown in **Fig. 4.21**. The Pedestals were subtracted and ADC values were calibrated by the pulse-hight

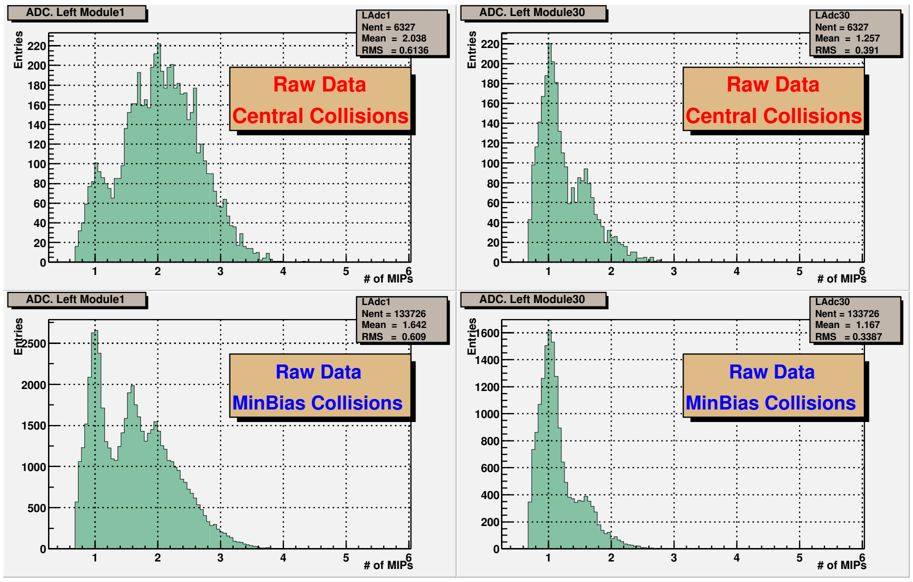

Figure 4.21: Particle hits distributions from the Raw Data. Small Tubes.

of the 1 particle hit response (See next chapter for more details), so **Fig. 4.21** shows particle hits distribution form the raw data. One can easily see, that "two particle hit peak" has a mean value of approximately 1.5, instead of the expected mean value of 2.0. This effect would arise from saturation in the tubes. A large number of particles generates a large current in the tube and space charge effect causes the tube to depart from the "linear region". The tube's specification indicates a 5% non-linearity at an instantaneous current of $8mA$ [38]. The first peak in the spectrum corresponded to a tube current of roughly twice that value.

Several tests were made in order to ensure that the saturation effect was really occurring and to develop a correction technique. If the saturation effect was due to space charge it could result form a high instantaneous rate of hits as might arise from a high background. This background, in turn, might be due to beam-gas collisions or to background particles entering the radiator from the side.

Alternatively, and more likely, is the possibility that the space charge resulted from the large number of of Cherenkov photons generated in the radiator. This number multiplied by the tube's high gain at $1700V$ produced the space charge.

Beam intensity studies.

Some data acquired during the run could be used to test the possibilities mentioned above:

1. One of the first runs had only 6 bunches circulating in RHIC. Later this number was increased to 56. Thus, the intensity in these few earlier runs was $(6\ bunches)/(56\ bunches)$ times smaller.

2. In some of the runs tubes were operated at $1600V$ *vs.* nominal $1700V$. This should decrease the current through the tube.

Fig. 4.22 shows the comparison of the regular ADC spectra (shown in the right panel) with the two lower intensity cases mentioned above. The ratio of the mean value of the "two particle hit peak" to the mean value of the "one particle hit peak" should be equal to 2.0. As one can see in **Fig. 4.22**, it is equal to $1.55 - 1.66$, which is consistent with the saturation concept. It also appears that a high background was not responsible for the saturation.

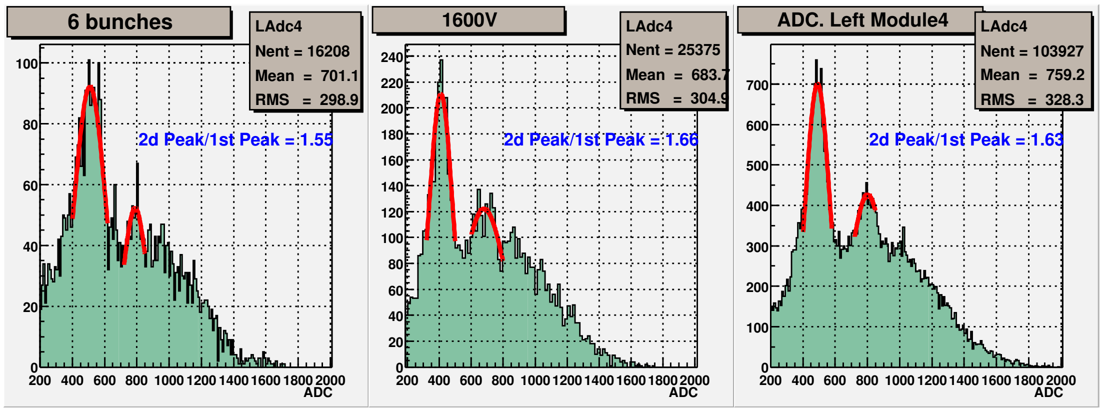

Figure 4.22: Particle hits distributions from the Raw Data. Small Tubes. Saturation studies.

Light-emitting diode studies.

These studies were performed in a tight light-protected dark box with an LED source of light as an input. Several Small Tube responses were compared to the response of a "known-to-be-linear" phototube. Experiments were conducted with different high voltage settings. The results are presented in **Fig. 4.23**. It is apparent that our Small Tube starts to behave in a linear way only if the high voltage is lowered to 1400V!

These studies were very important for three reasons:

1. They prove the saturation effect in our Small Tubes.

2. They provide us with one solution for this problem: Small Tubes have to be operated at a lower High-Voltage setting (presumably, 1500V should be enough to steer them back into the linear region).

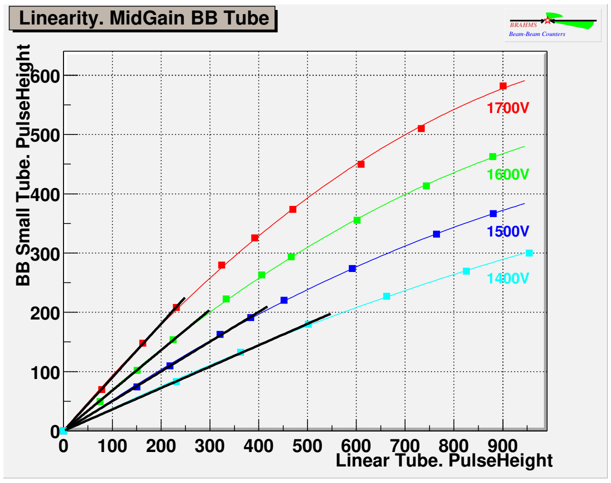

Figure 4.23: Light source studies of the Small Tube's linearity

3. The saturation effect can be corrected for by using the "1700V" graph from **Fig. 4.23** and by extracting the, so called, "*Nonlinearity Function*". This function can be later used for the off-line pulse height correction. This method turned out to be successful and is presented in the analysis section of this thesis in **Ch. 6**.

CHAPTER 5
DATA PREPARATION

This chapter discusses several technical achievements of the Beam-Beam Counters during the data-taking phase of the RHIC run. I will describe here

- How the Beam-Beam Counters response is extracted in general
- How the Beam-Beam Counters provide the space and time characteristics (t_o and z_o) of the collision event.
- How a collision event was identified and extracted from the global event pool.
- How the charged particle multiplicity was extracted from the raw events for different centrality cuts.

5.1 Data Extraction.

In this section I would like to show how data was actually acquired and to define several notations, that will be used later. The variables, necessary for the analysis are defined as follows:

Pedestals.

Fig. 5.1 shows the actual view of the signals registered by the ADC unit in the Left and Right Arrays, respectively. One can easily identify the huge spike in

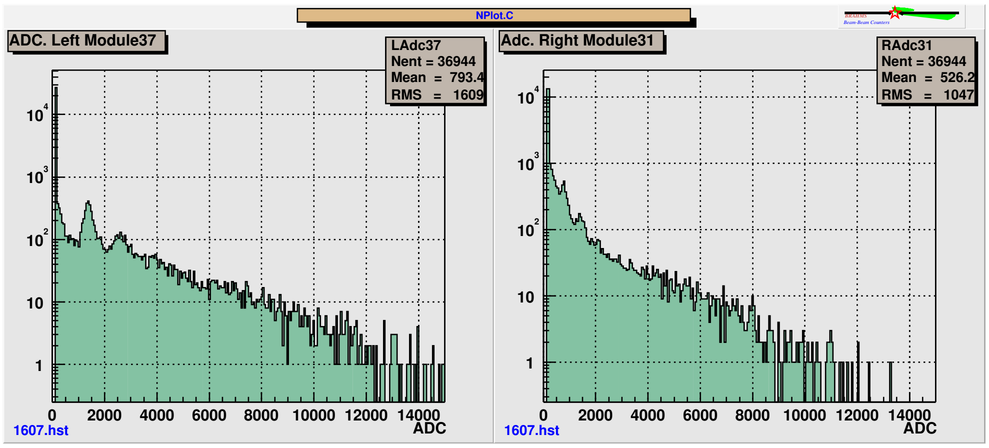

Figure 5.1: ADC Pedestals.

the few left-most bins of the histogram. This is caused by so called, "*pedestal*" and is created by the "blank" synchronization trigger, common for the whole experiment and designed for calibration purposes. The width of the pedestal characterizes the noise level in the system. A lot of effort was put into trying to make the noise as small as possible. The final noise level was down to a reasonable level of $2-3$ *ADC Channels*.

The pedestal can be isolated for extraction by requiring the information only from the synchronization trigger. The pedestal's mean value extracted from the histogram is written in the analysis database and is called `LPedMean[l]` or `RPedMean[r]` for the Left and Right Arrays, respectively, with indexes $l=\overline{1,44}$ and $r=\overline{1,35}$.

Gain values.

`AdcGain0[i]` – is the value of the *Adc Channel* corresponding to the converted

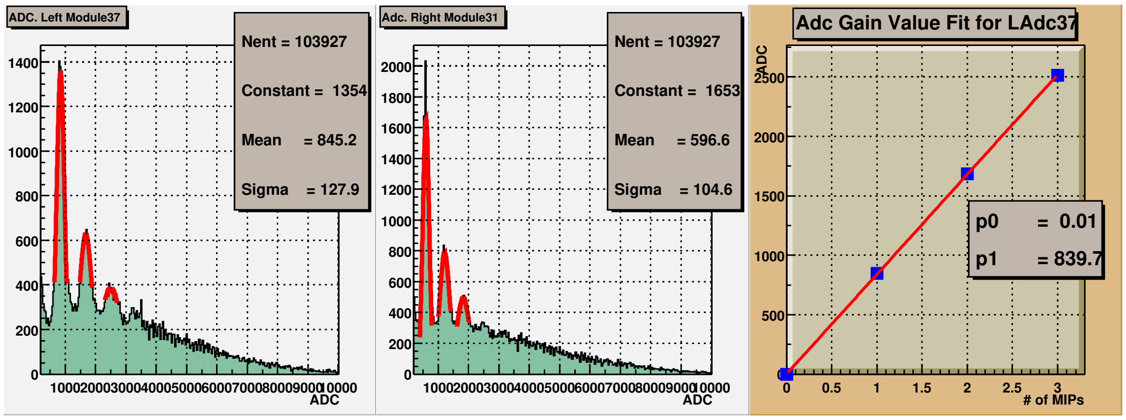

Figure 5.2: ADC Gain extraction.

analog response of the Beam-Beam Counters for one Minimum Ionizing Particle (MIP) hitting a detector. **Fig. 5.2** shows the pedestal subtracted view of the Left and Right ADC response to the collision events. Different peaks correspond to two, three and more MIP hits.

With the known gain value it is very simple to define the number of particles hitting the detector for the particular event as

$$n_L = \frac{(LAdc[l] - LPedMean[l])}{LAdcGain0[l]}$$
$$n_R = \frac{(RAdc[r] - RPedMean[r])}{RAdcGain0[r]}$$

where again $l = \overline{1,44}$ and $r = \overline{1,35}$. This scaling allows us to transform the ADC spectrum into the charged particle distribution spectrum for a particular tube.

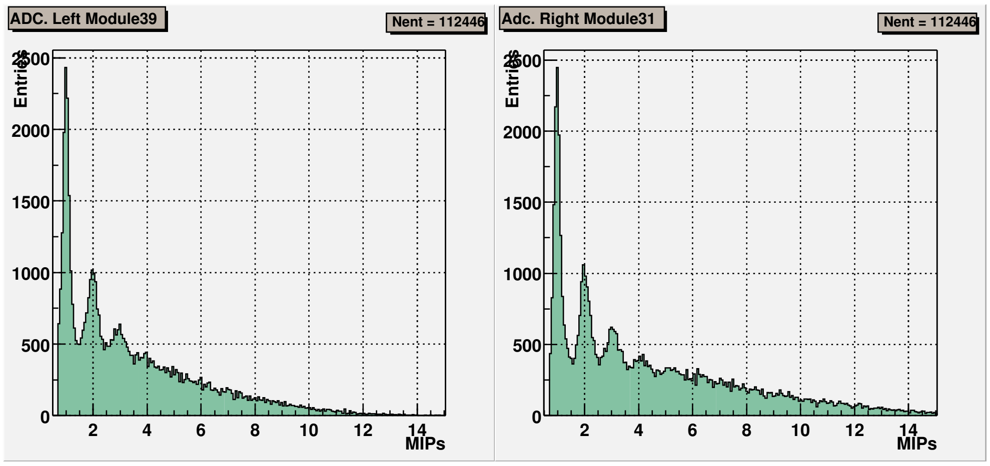

Figure 5.3: Calibrated ADC distribution.

Fig. 5.3 shows these kinds of distributions for the "Minimum Bias" events (no restriction on the impact parameter of the collision) in several Big Tubes. For a Minimum Bias events there are many events for which a particular tube has no hits. The large number of "*no hits*", or zero entries in the ADC spectrum produced a very high peak at zero making it difficult to see the one or higher hit peaks. The zero value is suppressed in these pictures for better representation. The good agreement between the experimental charged particle distribution and a Monte-Carlo example in **Fig. 4.20** in addition to our good understanding of the Monte-Carlo Minimum Bias distribution, allows us to claim that Big Tubes were not saturating at the level of 4 hits. Further studies showed that their linearity extended higher multiplicities of the order of 10 MIPs.

Also, **Fig. 5.3** shows the background located underneath the peaks. This background is partially due to the particle conversions in the beam-pipe and surrounding equipment and has to be subtracted later.

All extracted values of Gains, Pedestals and Pedestal Widths were placed in the database.

5.2 $t0$ and $z0$. Vertex Location.

Let's assume, that the collision event happens at some point along the beam-pipe at some instant of time: (z_o, t_o). Now, since we cannot physically measure the distance to the collision point we will have to assume, that most of the particles detected in the Beam-Beam Counters during the triggering were traveling at the speed of light c. Then we can figure out the vertex location by using some simple formulae and the time of the arrival as measured by our TDC unit. Let me modify **Fig. 4.18** a little bit and show the collision event geometry through the notations of time, as in **Fig. 5.4**:

Using T_L and T_R as the actual particle's time-of-flight (as compared to the time-of-flight t_L and t_R deduced from the TDC measurements, see later), to the

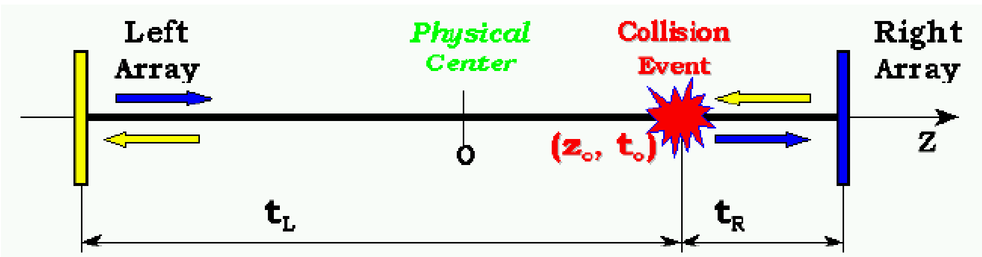

Figure 5.4: Collision Event geometry II.

Right and Left arrays respectively, one can easily write:

$$\begin{cases} T_L = t_o + (d + z_o)/c \\ T_R = t_o + (d - z_o)/c \end{cases} \quad and \quad \begin{cases} t_o = (T_L + T_R)/2 - d/c \\ z_o = (T_L - T_R) \cdot c/2 \end{cases}, \tag{5.1}$$

where c is the speed of light and $d = 219cm$ – distance from either of the arrays to the physical center.

The problem is how to relate the time measured in the TDC to the real time-of-flight. The TDC actually measures:

$$\begin{cases} t_L = T_L + \Delta T_L + T_{Trigger} \\ t_R = T_R + \Delta T_R + T_{Trigger} \end{cases}, \tag{5.2}$$

where

ΔT is the time offset due to a variety of reasons, some of which are:

1. some number of particles with $\beta < 1$;
2. different timing cable lengths;
3. difference in the timing characteristics of individual cables;
4. different transit time in individual phototubes.

and $T_{Trigger}$ is the trigger time common for every detector.

Substituting **Eq.(5.2)** into the **Eq.(5.1)** and merging all the offsets into the single vertex offset calibration constant of Δz, we get:

$$\begin{cases} z_o = (t_L - t_R) \cdot c/2 + \Delta z \\ t_o = (t_L + t_R)/2 - (219 + \Delta z)/c + T_{Trigger} \end{cases} \tag{5.3}$$

But the TDC does not measure time! Instead it returns information in digital units of TDC channels. This implies that the TDC's have to be calibrated in order to extract a calibration constant, converting the TDC channel number into time units. **Appendix C** describes this procedure in more detail.

Now let me

- demonstrate several methods of extracting t_L and t_R values for every collision event using the Beam-Beam Counters;
- identify the precision of each method and the necessary offset parameters;
- show figures of the characteristic z_o and t_o distributions for Summer 2000 collisions at RHIC.

By design, the BRAHMS experiment has more than one method for determining the collision vertex. Only the vertex determined by the Beam-Beam Counters can provide the vertex information to be used as a level 0 trigger for the experiment. On the other side, one of the TPC chambers, located in the Midrapidity Spectrometer arm (TPM1) can provide us with the vertex information with a precision of better than $5mm$ but in the analysis mode. It does that by matching particle tracks in two Time Projection Chambers and by tracing them back to the vertex position. This is a very complicated task which cannot be done in the online mode, but once this information is extracted in the analysis mode it helps us to determine the precision of our vertex locator and to identify all the offset constants needed in **Eq.(5.3)**.

Only events corresponding to true collisions must be used in all the procedures described here. Event selection will be discussed in more detail in **Sec. 5.3.1**. For the moment using triggers 4 and 6 as described in **Table 4.1** is adequate for selecting good collision events. The quality of each timing method is determined by comparing the vertex as measured by that method with the vertex extracted by TPM1 for the same collision event.

Let me start with the simplest method for vertex determination. It can be used, when no other method can provide us with t_L and t_R values. This method is mostly intuitive, but can produce the desired result.

5.2.1 Using "Earliest Left" and "Earliest Right" tubes.

This method is based on using the tubes in the Left and Right Array, which gave timing signals of being hit earlier than all others. The procedure for extracting timing information is as follows:

1. "Align" all tubes in time

   This is done by plotting cumulative TDC spectra for every tube and assuming that the timing signal for a particular event should arrive roughly at the same time for all tubes in the array. We require the `Mean` values for each tube's TDC spectrum over a large set of events to be identical. This requirement

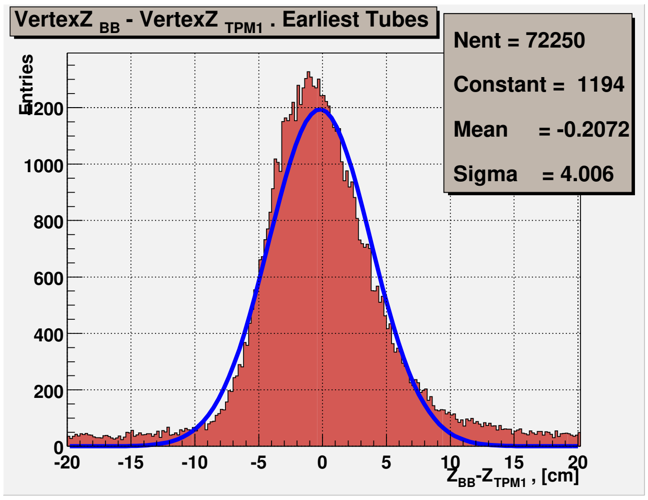

Figure 5.5: Beam-Beam Counters vertex resolution as compared to the vertex provided by the TPM1. The "Earliest" tubes.

introduces individual offsets for every tube in each array: $\Delta LTdc$ and $\Delta RTdc$.

2. Get the vertex value:

$$\begin{cases} t_L = (min(LTdc[i]) - \Delta LTdc) \cdot 25\frac{psec}{ch} \\ t_R = (min(RTdc[i]) - \Delta RTdc) \cdot 25\frac{psec}{ch} \end{cases},$$

where $min(RTdc[i])$ is the earliest Tdc value for all Right Array tubes for each event and $25psec/ch$ – TDC-to-time conversion constant, as from **Fig. C.2**. Now we just substitute these values into **Eq.(5.3)**.

3. Determine z_o resolution and the vertex offset calibration constant Δz:

We do that by comparing the vertex values found by this method to the vertex determined by the TPM1, as in **Fig. 5.5**. Vertex offset calibration constant Δz was determined by manually requiring the mean value of the vertex difference to be equal to 0. This correction is included in the picture. A vertex resolution $\delta z_o \simeq 4.0cm$ was determined through the Gaussian fit of the vertex difference as shown in **Fig. 5.5**. This resolution is rather poor since no "slewing" correction is possible for this method. The failure to include slewing is also seen in the poor fit of the Gaussian to the showed peak. That is why it can be used only as a last resort in our vertex determination when no other timing information is available.

5.2.2 Using Big Tubes only.

Real timing calculations require a more sophisticated approach. The problem that must be addressed, as described in **Sec. 3.3.2**, is that higher amplitude pulses cross the discriminator threshold earlier, than the smaller pulses. This is the source of the "walk" or time slewing. Consequently, the TDC signal can be used for time determination only after a "*Slewing correction*" is made.

Take the Right Array as an example. The Big Tube numbers are from 31 to 35, and again

$RTdc[i]$ and $RAdc[i]$	–	TDC and Adc channel number in the Right Module i;
$RPedMean[i]$	–	Pedestal value for the Right Module i;
$RPedRMS[i]$	–	Pedestal's RMS value for the Right Module i;
$RAdcGain0[i]$	–	Adc Gain value (as in **Sec. 5.1**) for the Right Module i;

- Use Tube 31 as a reference tube and fill 4 histograms with the TDC differences as $(RTdc[31] - RTdc[i])$ for all collision events (see **Sec. 5.3.1** for the collision event definition) and with the following restrictions on the pulse hight:

$$\left[\begin{array}{lcl} |(RAdc[31] - RPedMean[31]) - RAdcGain0[31]| & < & 0.10 \times RAdcGain0[31] \\ (RAdc[i] - RPedMean[i]) & > & 0.7 \times RAdcGain0[i] \end{array}\right. \tag{5.4}$$

  where first line of this condition corresponds to the pulse height in the reference tube 31 to differ by less than 10% from the pulse hight corresponding to 1 MIP, when $Adc[i] \equiv AdcGain0[i]$, and second line says, that the signal in the other tube has to correspond to at least one hit in the tube (70% level of 1 MIP hit). And these conditions on the TDC signal:

$$\left[\begin{array}{cc} RTdc[31] > 10\ ; & RTdc[31] < 2200 \\ RTdc[i] > 10\ ; & RTdc[i] < 2200 \end{array}\right. ,$$

  meaning, that we require for the TDC signal to be present (nonzero) and to be reasonably in time.

- Do a Slewing or Walk Correction for 4 Big Modules, $i = 32, \ \ldots\ , 34$ by filling again these histograms for the conditions mentioned above, but now using a slewing correction in a customary form as:

$$RTdc[31] - \left(RTdc[i] - \frac{k_i}{\sqrt{(RAdc[i] - RPedMean[i])}} \right) \tag{5.5}$$

and getting Slewing Constants k_i for each of these 4 modules by minimizing the “sigma” of the Gaussian fit of the histogram. A similar procedure is used for finding the slewing constant for the reference tube, using one of the others.

- Align these 4 histograms of TDC differences to have mean value 0 and, by doing that, obtain Aligning Constants $\Delta RTdc[i]$ with $i = 32,\ \ldots\ , 34$

- Obtain corrected (slewed) values for the TDC’s and the number of tubes N_R, satisfying all the conditions above for this particular event ($N_R \leq 5$):

$$RTdcSlew[i] = \left(RTdc[i] - \frac{k_i}{\sqrt{(RAdc[i] - RPedMean[i])}} - \Delta RTdc[i] \right)$$

Fig. 5.6 shows the comparison between the TDC difference before and after the slewing correction, as well as the comparison of the TDC difference *vs.* ADC dependence before and after the slewing correction. It can be seen how the slewing correction improves the timing. The timing resolution improved from 152*psec*, shown in the top-left panel of **Fig. 5.6**, to the value of 63*psec* on the top-right panel. It improved almost by a factor of 3, and so is the t_o!

- Find the average value and remove the “outliers”, tubes, that give time outside

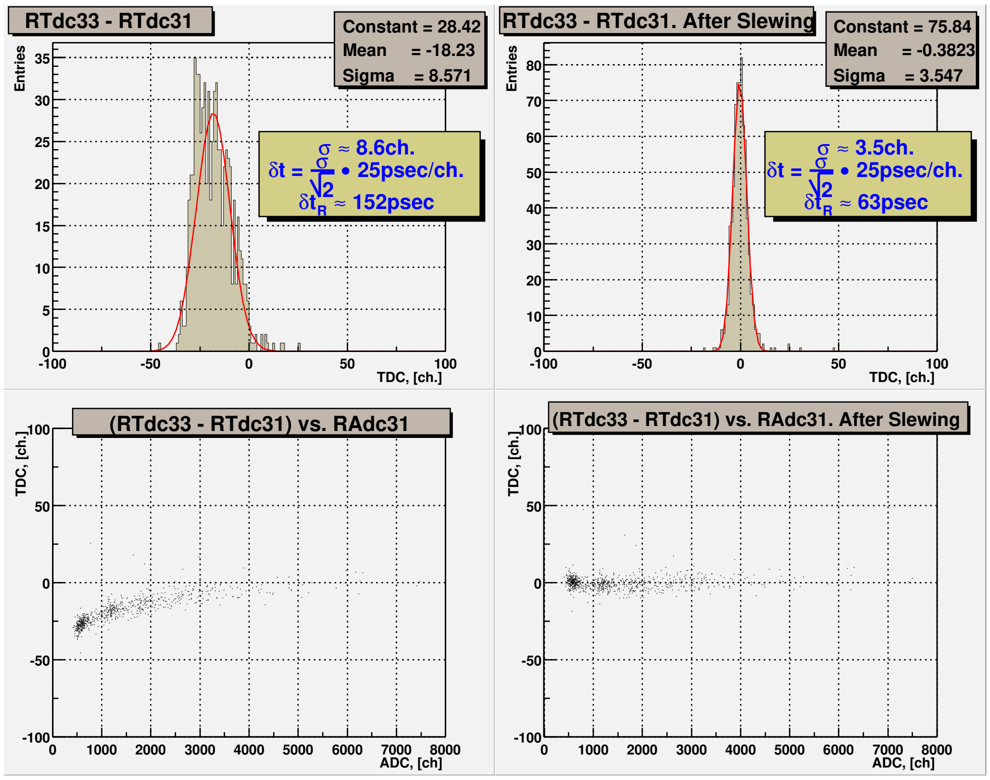

Figure 5.6: TDC difference and TDC difference *vs.* ADC dependence in two Right Array Big Tubes before and after the slewing correction.

of the 3σ range of the mean value:

$$RTdcAverage = \frac{1}{N_R} \sum_{i=31}^{35} RTdcSlew[i]$$
$$|RTdcSlew[i]_{outlier} - RTdcAverage| < 3 \cdot \sigma_{timing},$$

where σ_{timing} is the Beam-Beam Counters timing resolution, which is described in **Sec. 5.2.4**.

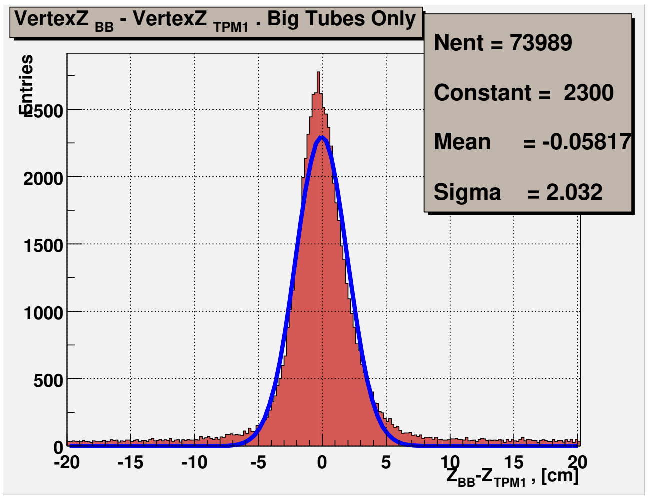

Figure 5.7: Beam-Beam Counters vertex resolution as compared to the vertex provided by the TPM1. Big Tubes only.

- Get t_R using Big Tubes, that survived all the conditions and the outliers removal.
- Get Δz and δz_o as in previous paragraph by the comparison of the vertex location extracted using this method, with the vertex value determined by the TPM1. **Fig. 5.7** shows this comparison and gives us $\delta z_o \simeq 2.0cm$.

5.2.3 Using Small Tubes only.

In this section I will show another approach in determining the vertex location and timing using our Small tubes as an example. Let me now use the Left Array and Left Tube 4 as a reference tube. Here are the steps of the Slewing correction using Left Tube 3 as an example and all same notations as for the Big tubes:

- In exactly the same fashion, as was described for the case of the Big tubes, we fill one histogram with the TDC differences as $(LTdc[4] - LTdc[3])$ for all collision events (see **Sec. 5.3.1** for the collision event definition) and the other histogram, two dimensional, with the $(LTdc[4] - LTdc[3])$ *vs.* $LAdc[3]$ dependence. The same restrictions were used on the pulse hight, as for the Big tubes:

$$\left[\begin{array}{ccc} |LAdc[4] - LPedMean[4] - LAdcGain0[4]| & < & 0.10 \times LAdcGain0[4] \\ (LAdc[3] - LPedMean[3]) & > & 0.7 \times LAdcGain0[3] \end{array}\right. , \tag{5.6}$$

where first line of this condition corresponds again to the pulse height in the reference tube 4 to differ by less than 10% from the pulse hight corresponding to 1 MIP, when $Adc[i] \equiv AdcGain0[i]$, and second line says, that the signal in the other tube has to correspond to at least one hit in the tube (70% level of 1 MIP hit). And again these conditions on the TDC signal:

$$\left[\begin{array}{l} LTdc[4] > 10\ ; \quad LTdc[4] < 2200 \\ LTdc[3] > 10\ ; \quad LTdc[3] < 2200 \end{array}\right. ,$$

meaning again, that we require for the TDC signal to be present (nonzero) and to be reasonably in time. One dimensional histogram of the $Tdc[4] - Tdc[3]$ before the Slewing correction is shown in **Fig. 5.8** , top left panel. It is quite wide!

- Now, let's look at the two-dimensional histogram, shown in the top center

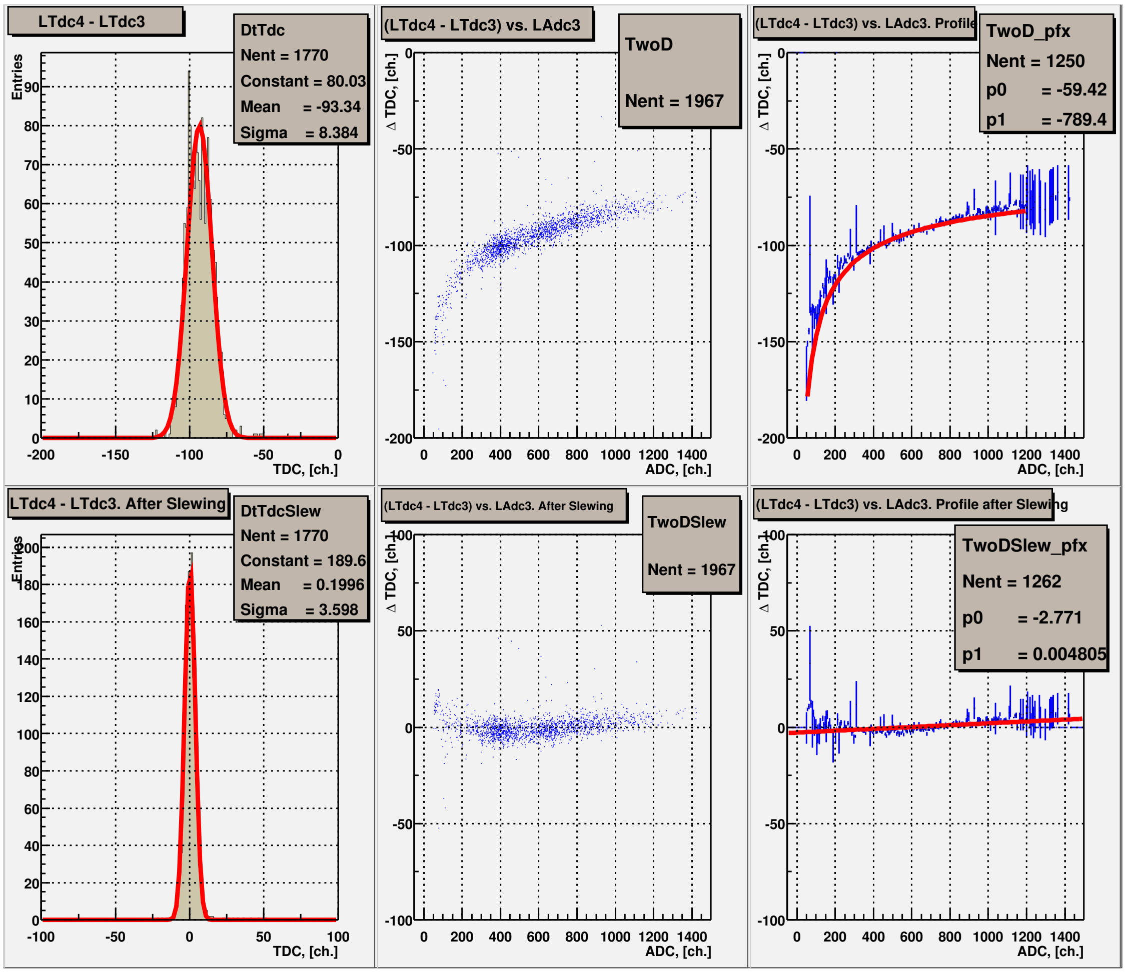

Figure 5.8: Slewing correction. Small tubes.

panel of **Fig. 5.8**. We can do a slewing correction here by fitting this 2-d histogram with a function and using this function later for the correction. This was done using the profile of the 2-d histogram. The top-right panel of **Fig. 5.8** shows such fitting. Standard function was used in the fitting procedure:

$$SlewFunc(adc) = p0 + \frac{p1}{\sqrt{adc}}, \tag{5.7}$$

the same as for the Big tubes.

- The slewed (corrected) $LTdc[3]$ value was obtained in the following way:

$$LTdcSlew[3] = \left(LTdc[4] - \frac{p1}{\sqrt{(LAdc[3] - LPedMean[4])}} - p0 \right),$$

in the same way, as for the Big tubes.

- The bottom panels of **Fig. 5.8** show the improvement we achieved with this slewing method. It was used to do the slewing correction for all of the Small tubes.

- The rest of the procedure is absolutely the same and Δz and δz_o again were found by the comparison of the vertex location extracted using this method, with the vertex value determined by the TPM1. **Fig. 5.9** shows this comparison and gives us $\delta z_o \simeq 1.5cm$.

The last two methods are complementary to each other and allow the Beam-Beam Counters to locate the collision instant in time and position in space with good precision. Since Small tubes allow to get better vertex precision (the vertex resolution $[\delta z_o]_{Small} < [\delta z_o]_{Big}$), they are used as a primary vertex location source.

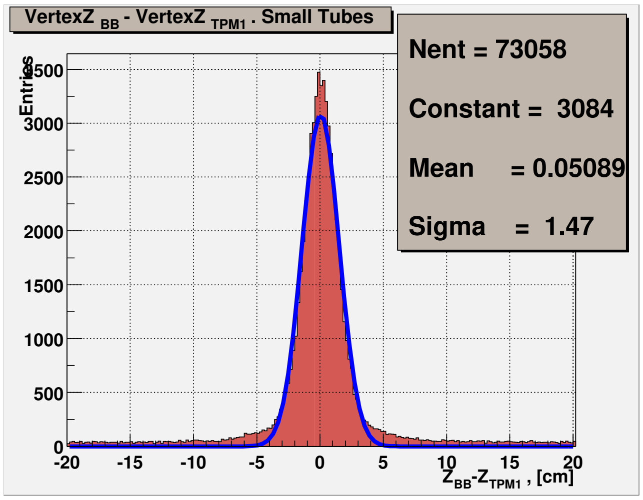

Figure 5.9: Beam-Beam Counters vertex resolution as compared to the vertex provided by the TPM1. Small Tubes only.

5.2.4 Time resolution and collision vertex.

The timing resolution of the Beam-Beam Counters can be defined through the difference between the collision time identified by any one of the counters and the average collision time identified by all of them. Let me do that for two sets of our tubes:

Big Tubes

The top panel of **Fig. 5.10** shows these kinds of distributions for the Big Tubes. Let's calculate the Beam-Beam Counters time resolution for the "*Big Tubes Only*" method. From the top panel of **Fig. 5.10** one can see, that $\sigma_{t_L} \simeq 82psec$ and $\sigma_{t_R} \simeq 98psec$. The bottom panel of this figure shows the hit distributions in two arrays. It shows, that 6.1 tubes were hit on the average in the Left Array and 4.0

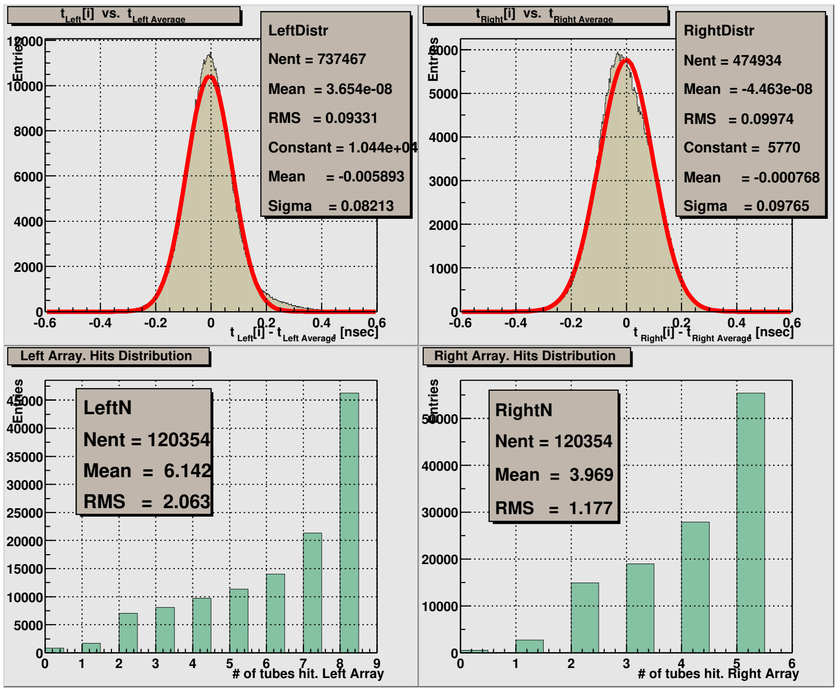

Figure 5.10: Time Resolution of the Beam-Beam Counters Big tubes.

in the Right, respectively. Taking into account these mean numbers of Big Tubes being hit in the Left and Right array, one can easily get:

$$\begin{cases} \delta t_L = \sigma_{t_L}/\sqrt{n_L} \simeq 82psec/\sqrt{6.1} \simeq 33psec \\ \delta t_R = \sigma_{t_R}/\sqrt{n_R} \simeq 98psec/\sqrt{4.0} \simeq 49psec \end{cases} \Longrightarrow \quad \delta t = \sqrt{(\delta t_L)^2 + (\delta t_R)^2} \;\simeq\; 59psec,$$

and that gives the vertex resolution to be:

$$\delta z_o = \frac{c}{2} \cdot \delta t \simeq 9mm$$

Small Tubes

Due to the large number of the Small Tubes, timing information can be extracted from them with better precision. **Fig. 5.11** shows time deviations and hit distributions for the Small tubes. The same analysis as for the Big tubes gives us:

$$\begin{cases} \delta t_L = \sigma_{t_L}/\sqrt{n_L} \simeq 92psec/\sqrt{14.4} \simeq 24psec \\ \delta t_R = \sigma_{t_R}/\sqrt{n_R} \simeq 125psec/\sqrt{8.2} \simeq 44psec \end{cases} \Longrightarrow \delta t = \sqrt{(\delta t_L)^2 + (\delta t_R)^2} \simeq \ 50psec,$$

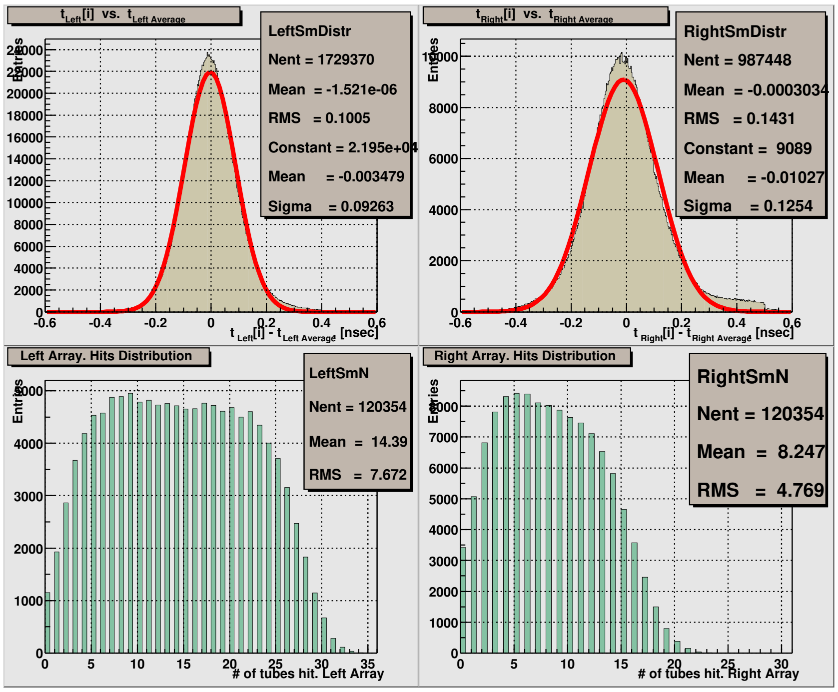

Figure 5.11: Time Resolution of the Beam-Beam Counters Small tubes.

and that gives the vertex resolution to be:

$$\delta z_o = \frac{c}{2} \cdot \delta t \simeq 8mm,$$

which agrees with the result from the Big tubes. At least two assumptions have to be made for the validity of these results:

i) all particles, that hit our detector, have $\beta = 1$;

ii) all tubes are perfectly aligned in time with the precision better than the best claimed time resolution of $24psec$.

This is definitely not the case, that is why we have to use the deviation between the vertex determined by the Beam-Beam Counters and the vertex determined by the TPM1 in order to claim our time and vertex resolution.

Our best timing result, achieved with the Small tubes gave us the vertex resolution of $\delta z_o \simeq 1.4cm$. With several improvements, the vertex resolution from the Small tubes can be made more precise:

1. The TPM1 vertex y-coordinate resolution of $\delta y \simeq 8mm$.
2. The tracking imperfections, which give us these "shoulders" in **Fig. 5.9**
3. The σ of the Gaussian fit to the graph in **Fig. 5.9** restricted by the $|\Delta z_o| \leq 3cm$ range.

All these things together improve our vertex and timing resolutions to the values of

$$\boxed{\delta z_o \simeq 1.0cm \Rightarrow \delta t_o \simeq 65psec}$$

Collision vertex.

The final picture I want to present in this section describes a collision vertex distribution, as measured by the Beam-Beam Counters. **Fig. 5.12** shows a

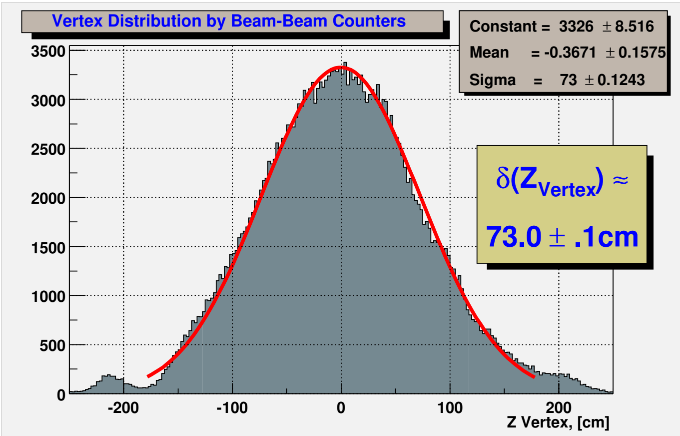

Figure 5.12: Collision vertex distribution.

distribution of vertex positions in the "*Collision Diamond*". It shows, that vertex position z_o was smeared longitudinally with an approximately Gaussian distribution with $\sigma_{Vertex} \simeq 75cm$. This conclusion was later confirmed by the RHIC accelerator group!

> *Our final conclusion: the Beam-Beam Counters successfully served as a level0 trigger and a vertex locator with the design resolution.*

5.3 Raw Data Analysis.

This section presents the analysis procedure followed to obtain the charged particle multiplicity distribution. Before undertaking the analysis, a valid class of events has to be identified, the data has to be extracted in it's raw form, and all necessary acceptance corrections have to be made.

5.3.1 Event selection and centrality determination.

Primary to our analysis is the identification of collision events. Several steps were followed to accomplish this.

❶ Trigger selection:

This was done the same way as described in **Sec. 4.2.2**, using different trigger definitions; ZDCs trigger, $Trig$ 4 served as a "*Minimum Bias*" trigger, identifying all the peripheral events and the Beam-Beam Counters served as a good collision trigger with a narrow vertex cut. Thus, both triggers had to be used inclusively in order to identify the collision event.

❷ Vertex restriction:

The next step was to restrict the events, to those which occurred within the collision diamond. Based on the size of the diamond, delivered to our IR by the RHIC accelerator team, we restrict our collision events to be within a range of $|z_o| \leq 150cm$. This follows from the above

$$150cm \simeq 2 \cdot \sigma_{Vertex}, \qquad \text{where} \qquad \sigma_{Vertex} \simeq 75cm,$$

as in **Fig. 5.12**.

❸ Centrality determination:

The centrality of the event has to be determined in order to select the most central collision events with impact parameter $b \leq 3fm$. Since these events will give us the maximum particle density in the collision region, they are the most interesting to look at and to compare to the event-generator models described earlier. In addition, it should be interesting to look at different centrality cuts to be identified later.

Many different methods exist to determine centrality in general. Here, at BRAHMS, most of them involve the Scintillator Tiles, as a part of the Multiplicity Array and a special device designed to provide a centrality cut. All these methods differ in detail, but do have one major point in common: they use the total number of particles, registered in the device (through the deposited energy) as a signature of the centrality. This can be easily understood if we go back and look at the "*spectator-participant*" model, shown on **Fig. 2.4**. The number of particles, participating in the collision, and thus the number of charged particles produced in it, is inversely proportional to the impact parameter b of the collision. **Fig. 5.13** shows the total number of particles registered in the Multiplicity Array (Scintillator Tiles). The most central events produce the largest number of particles. Three different centrality cuts are shown, with 0% centrality equivalent to the most central

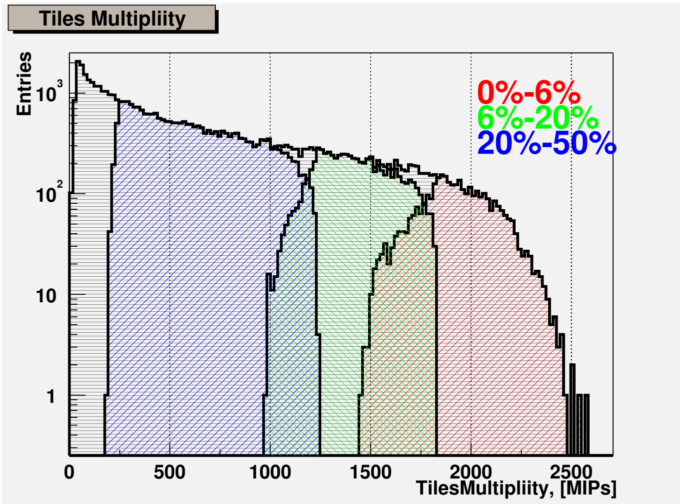

Figure 5.13: Scintillator Tiles Multiplicity distribution. Percents represent centrality of the collision: 0% – the most central collisions with impact parameter $b = 0fm$.

collision events with the impact parameter $b = 0fm$.

The only problem with this approach lies in the vertex dependence of the Tile's output. The geometrical range of the tiles physical location at $\pm 30cm$ with respect to the vertex makes them incapable of providing centrality for wider cuts. But as it was mentioned earlier, the RHIC' collision vertex had $\sigma \simeq 75cm$ during the year 2000 run which is much wider the designed value of $\sigma \simeq 15-20cm$. That is why different methods for the centrality determination, vertex independent methods, had to be employed. The geometrical analysis of this problem provides us with one very simple solution: use detectors located at both sides of the vertex. The ZDCs and the Beam-Beam Counters are the only two detectors satisfying these requirements.

`ZdcAdcSum` plotted *vs.* the total number of MIPs registered in the Beam-Beam

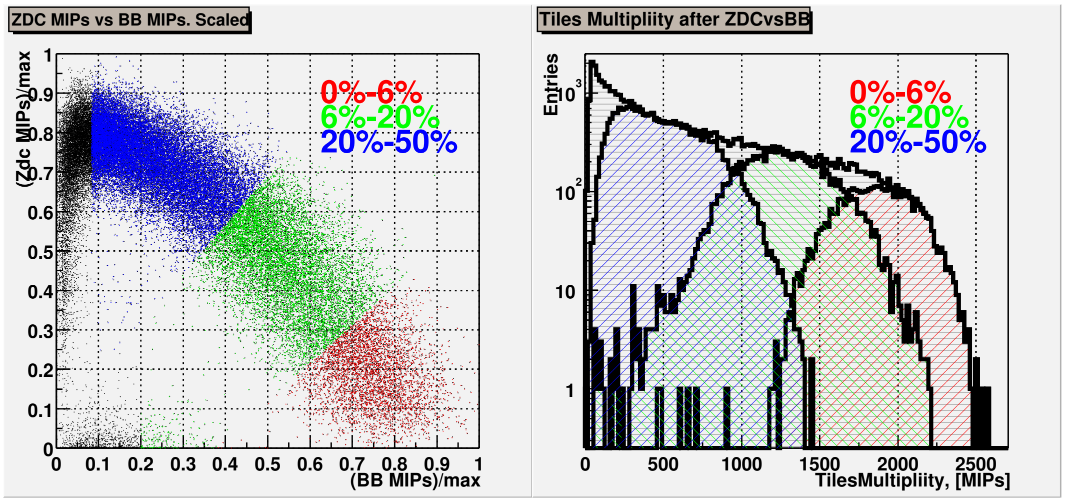

Figure 5.14: Centrality determination method, using ZDCs and BBCs.

Counters can provide the range for the different centrality cuts. `ZdcAdcSum` is essentially a total amount of energy, deposited in the ZDC array. The graph is expected to have an inverted horseshoe shape and this can be explained as follows: for very peripheral events, when no particles will be registered in the Beam-Beam Counters, the ZDC sees just a few neutrons, liberated in the collision with a very small number of participants. At the same time, for a very central event, when all nucleons participate in a collision, the ZDC will again register again very small number of neutrons, with a big amount of deposited energy in the intermediate cases. **Fig. 5.14** shows this graph with different shades representing different centrality cuts, and with a comparison of these cuts to the multiplicity registered in the Scintillator Tiles, mentioned above. Both methods were performed on the collision events with the same vertex restrictions of $|z_o| \leq 30cm$.

As shown in **Fig. 5.14**, the following centrality cuts were chosen to perform the analysis:

1. 0% − 6% centrality;

2. 6% − 20% centrality;

3. 20% − 50% centrality;

Two consistency checks were made:

1. The outcome of this centrality method was compared to the other one, using Tiles Centrality cuts for the same vertex cut. The charged particle multiplicity distribution based on the `ZDCvsBBC` 0% − 6% centrality cut for the events with $|z_o| \leq 30cm$ was within 1.5% of the $dN_{ch}/d\eta$ numbers extracted using the Tiles Centrality method for the same class of events.

2. How precise and consistent within itself is this new method based on the `ZDCvsBBC` dependence? $dN_{ch}/d\eta$ numbers extracted for 0%−6% central events were found to be about ∼ 5% above the numbers for the 0%−9% central events and about ∼ 7% above the numbers for the 0% − 10% central events. This small monotonic increase is consistent with expectations.

Even though two centrality definitions are not identical, the difference between them is well within the systematic error of our measurements. Thus, we conclude, that we can use the `ZDCvsBBC` as one of the possible centrality methods for the Beam-Beam Counters analysis.

5.3.2 Dealing with the Raw Data.

Here I would like to give the detailed step-by-step description of the charged particle multiplicity analysis method starting from the raw ADC spectrum of the phototube:

1. Extract the ADC pedestal values, `PedMean`, the ADC gain values, `AdcGain0`, and the number of MIPs, hitting the detector in a collision event, n, as described in **Sec. 5.1**.

2. Do the acceptance correction in order to determine N, equivalent number of hits for the whole segment of the array, as shown on **Fig. 5.15**. The shaded

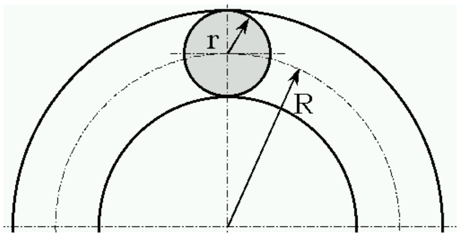

Figure 5.15: Beam-Beam Counters acceptance correction.

tube with radius r sits at a distance R from the beam pipe. Thus, if we know the number of hits hitting the face of the tube (area of πr^2), and assuming that the entire tube area has the same efficiency, we can recalculate how many particles are hitting the whole segment of the array, which occupies a ring at a distance $R \pm r$ from the beam pipe:

$$N = n \cdot \frac{RingArea}{TubeArea},$$

where

$$RingArea = \pi(R+r)^2 - \pi(R-r)^2, \qquad TubeArea = \pi r^2$$

We assume here that the hits density stays constant along the face of the tube.

3. Determine the vertex location of the collision z_o, as described in **Sec 5.2.4**

4. Use this vertex value, **Eq. (1.7)** and **Fig. 6.16** in order to find η, $\Delta\eta$ and $dN/d\eta$ as:

$$\begin{aligned} \eta &= -log\left[tan(\theta/2)\right], \\ \theta &= tan^{-1}\left(\frac{R}{d}\right), \\ \Delta\eta &= \eta|_{R=R+r} - \eta|_{R=R-r}, \end{aligned}$$

where

R – distance to the ring of tubes from the beam-pipe;

θ – angle between the beam-pipe (z-axis) and a ray from the vertex to the tube, as in **Fig. 1.2**;

d – distance from the vertex to the array location along the z-axis, as in **Fig. 4.18** and

$\Delta\eta$ – change of pseudorapidity value along the face of the tube.

5. Thus, for every tube and for every event we can extract a pair of numbers: $\{\eta,\ dN/d\eta\}$, where one can easily find $dN/d\eta = N/\Delta\eta$.

6. The physical location of the tubes and the vertex restriction on the collision events of $|z_o| \leq 150cm|$ provide us with a range of $\eta_{min} \leq \eta \leq \eta_{max}$ available to the Beam-Beam Counters. This range is split into smaller intervals of $\Delta\eta = 0.05$ with the number of intervals obviously dependent on the total range. For each small interval $\Delta\eta$, an individual histogram is created which is filled with $dN/d\eta$ values whose η fall in this particular interval. **Fig. 5.16** shows two examples of such histograms for Left and Right Array. This method

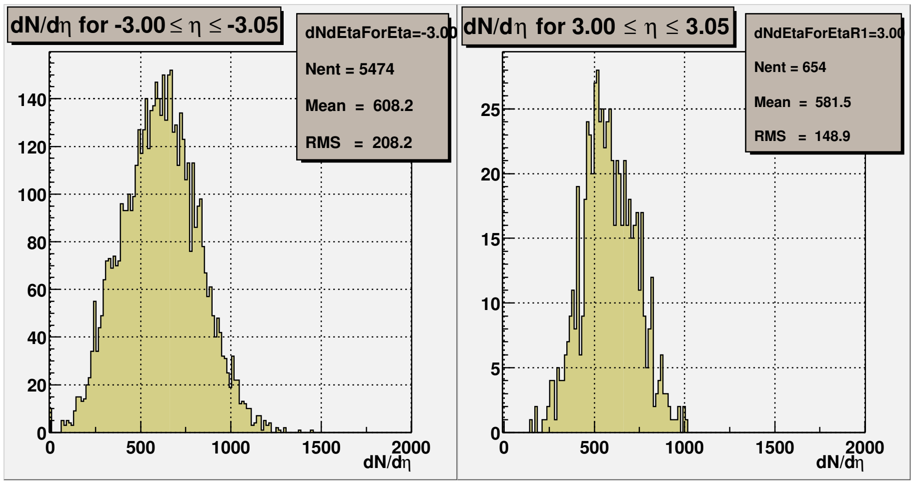

Figure 5.16: Histograms for extracting $dN_{ch}/d\eta$ values for small intervals of pseudorapidity.

forces the η uncertainties to be equal to $\delta\eta = \frac{1}{2}\Delta\eta = 0.025$.

7. The actual $dN_{ch}/d\eta$ values are extracted from the corresponding histogram as a `Mean` value of the distribution, and with `RMS` value, scaled by the $1/\sqrt{Entries}$ as a corresponding statistical error value. For example, from **Fig. 5.16** we

would extract the following points to be placed on the $dN_{ch}/d\eta$ *vs.* η graph:

$$\eta = -3.025 \pm 0.025 \qquad\qquad \eta = 3.025 \pm 0.025$$

$$dN_{ch}/d\eta = 608.2 \pm 2.8 \qquad\qquad dN_{ch}/d\eta = 581.5 \pm 5.8$$

Finally, **Fig. 5.17** shows the raw data charged particle multiplicity distributions for central collision events, extracted through the `ZDCvsBBC` centrality method described above. The Big tubes are used in this figure as an example. The HIJING charged particle multiplicity distribution is shown on the graphs for comparison with the raw data. Same analysis steps are used in the next chapter to extract the charged particle multiplicity information from the Small tubes. The Small tubes

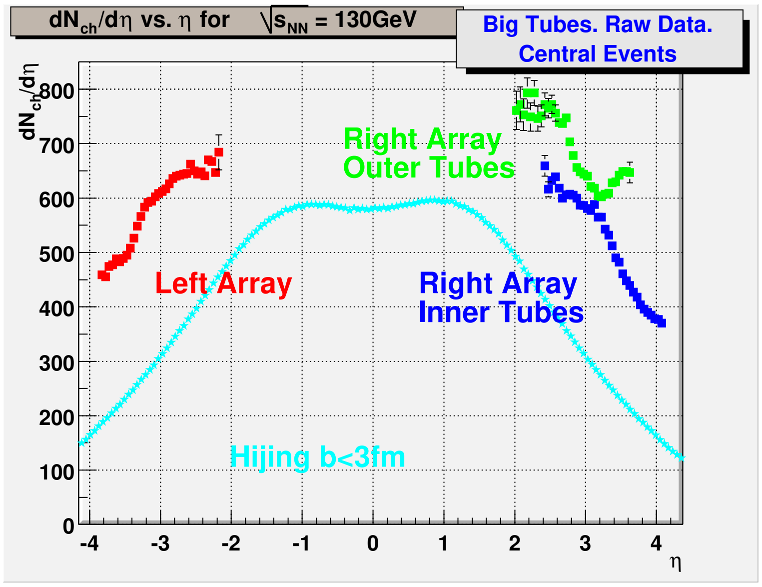

Figure 5.17: $dN_{ch}/d\eta$ *vs.* η. Raw Data. Big tubes.

analysis is slightly different from that of the Big Tubes, since it requires a nonlinearity correction.

The raw data presented in **Fig. 5.17** includes all background from the secondary particles created in the surrounding materials due to a variety of processes and interactions. Only primary particles should be included in our analysis. The next chapter will describe how this background can be determined and subtracted.

CHAPTER 6
DATA ANALYSIS

This chapter will describe how the final charged particle multiplicity distribution can be extracted from the raw data presented in **Ch. 5**. It will discuss the background subtraction mechanism and will present several ways of utilizing data from the Small Tubes. The angular symmetry of the charged particle multiplicity will be analyzed. Now, let me pick up where we have stopped in the previous chapter and continue to the question of the background estimation in the relativistic heavy ion collisions.

6.1 GEANT and Background Corrections.

The final step in our lengthy analysis is the determination of the background. The results presented in the previous section include a myriad of charged particles created at points other than the true collision vertex. These particles represent a background, for example, γ-rays converting to a $e^+ - e^-$ pairs in the beam-pipe and in the material surrounding the Beam-Beam Counters. This section discusses how to identify this background in order to “clean up” our collision events.

The philosophy behind such an approach is based on a comparison of the detector’s actual performance and the response generated by Monte-Carlo simulations. The Monte-Carlo simulation is the only method to identify the background particles created in the secondary collisions. In our case this would be a comparison of the ADC spectrum from the response of one of our phototubes in the real collision with the simulated ADC distribution from the events + background, artificially generated in the Monte-Carlo simulations.

6.1.1 GBRAHMS.

There exists a special code for simulating High Energy Physics Experiments and the response of various detectors to the input collision models such as described in **Sec. 2.2**. CERN code GEANT [43] was used for this purpose. The GEANT program describes the passage of elementary particles through matter. The principal applications of GEANT in High Energy Physics are:

1. the tracking of particles through an experimental setup for simulation of detector response;
2. the graphical representation of the setup and of the particle trajectories.

A code called GBRAHMS includes all the components of the BRAHMS experiment: magnets, detectors, *etc.*, including their geometrical positions, composition, performance characteristics, response functions, *etc...* GBRAHMS is able to track particles distributed by the input event generator throughout the BRAHMS hardware. A small part of this code describes the geometry and performance of the Beam-Beam Counters.

An additional piece of code used a geometrical model to trace each charged particle entering the detector and find the number of photons generated in the Cherenkov radiator, using **Eq. (3.1)**. The photons in turn, were tracked through the lucite to the photocathode. All possible total internal reflections of light inside the lucite were tracked and accounted for. A special correction for the lucite absorption of light was included in this code. Also, a special digitization routine was written and used to produce an ADC spectrum of the detector's response from the generated number of photons. As a result, the simulated phototube response was made to match as close as possible the test-beam study results shown in **Fig. 4.1**.

All possible sources of the background were included in the simulation code. These parts of the BRAHMS set-up were found to introduce most of the background:

1. *Al* part of the beam-pipe, as was discussed in **Sec. 4.1.2**.

2. *Al* material of the array's holders, as described in **Sec. 4.1.2**.

3. Special beam-pipe support construction

4. The Multiplicity Array partially block the path of particles coming from collisions far away from the physical center. Thus it creates a lot of the background as well.

Fig. 6.1 shows the actual GBRAHMS output. All parts of the BRAHMS experiment responsible for introducing background into the Beam-Beam Counters are presented there. One can easily identify the metal holder plates, supporting the Beam-Beam Counters phototubes. In front of them, in green, a special beam-pipe holder is shown. The middle part of the picture is occupied by the Multiplicity Array.

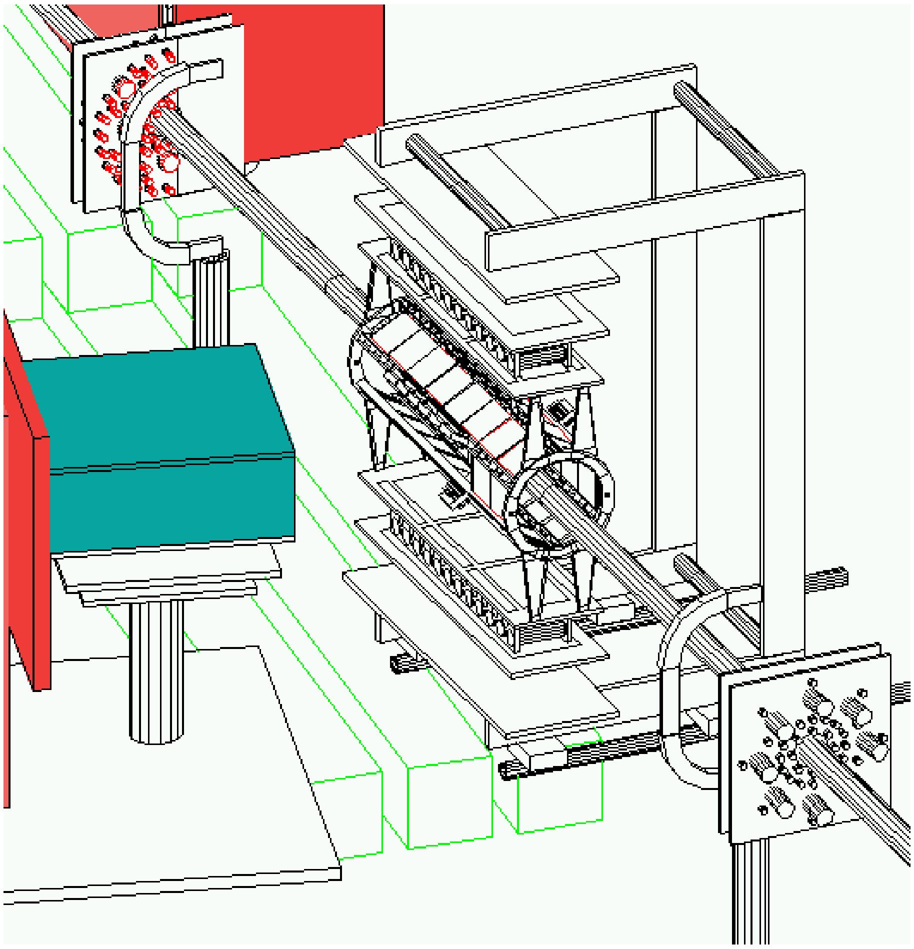

Figure 6.1: Background introducing hardware. GBRAHMS output.

6.1.2 Models and background corrections.

The next step in the background determination is to pick a model, describing the charged particle distribution for gold-gold collisions at $\sqrt{s} = 130GeV$. As discussed in **Sec. 2.2**, predictions of the available models differ almost by a factor of two in the number of charged particles in the unit of pseudorapidity at the midra-

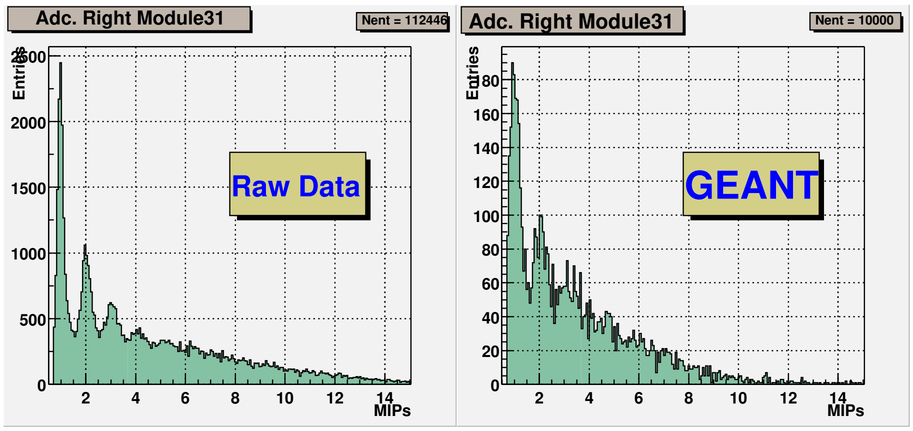

Figure 6.2: ADC spectra comparison. Raw data *vs.* GEANT simulations.

pidity level ($\eta = 0$). Thus, it could be a very complicated task to produce outputs for every available event generator, and to try and match it with the measured results. Many models were used and considered, but the first experimental results from RHIC, as described in **Sec. 2.3**, suggested that the HIJING event generator was better than other models describing the charged particle multiplicity in the midrapidity region. That is why we used this model for our background studies. The HIJING model details are discussed in **Sec. 2.2**.

Fig. 6.2 shows a comparison of the two ADC spectra. "*Minimum Bias*" collision events raw ADC spectrum in the left panel of the picture is compared to the model-generated GEANT simulation ADC spectrum for the same class of events on the right one. The HIJING event generator was used as an input. From the similarity of the two we conclude that we can use the GEANT output for the purpose of the background correction.

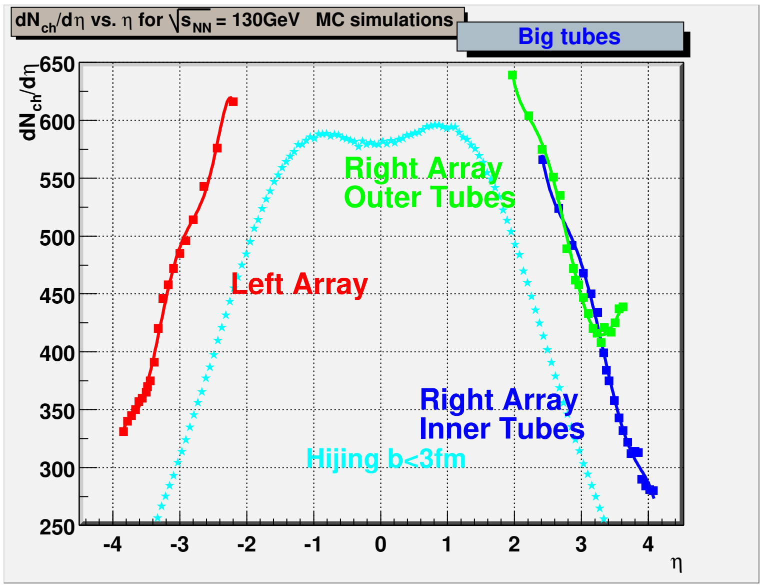

Figure 6.3: Charged particle multiplicity distribution for the Beam-Beam Counters Big Tubes in GEANT simulations.

A set of GEANT simulation files were generated. Each file was for a specific vertex. Therefore, a large number of them was needed to cover the wide range of possible vertex locations. With the collision diamond distributed with $\sigma \simeq 75cm$, as was shown on **Fig. 5.12**, it was reasonable to use the vertex range of $|z_o| \leq 150cm$ for our collision events. This condition required the generation of 20 simulation files, each for a pinpoint vertex located at different points evenly distributed within this range. **Fig. 6.3**. shows three different curves as an example, for three different sets of Big Tubes:

- Two sets from the Right Array, shown in blue and green, and
- One set form the Left Array, shown in red.

Once we have the GEANT simulations output for the measured charged particle multiplicity, including the background, we have to generate a set of the "*background correction coefficients*" as:

$$k = \frac{(dN_{ch}/d\eta)_{HIJING;\ No\ Background}}{(dN_{ch}/d\eta)_{HIJING;\ With\ the\ Background}}, \tag{6.1}$$

assuming, that the actual HIJING distribution represents "*No background*" charged particle multiplicity distribution. Index $[i]$ in the coefficient stands for the different correction value depending on the vertex position or η value. The strange jump in the Right Array green line for the Outer Big Tubes is attributed to the high background due to the Multiplicity Array, which starts to interfere and contribute to the background for the far left vertex locations ($z_o \leq -75cm$).

The extracted background correction coefficient can be used to correct the results of **Sec. 5.3.2**:

6.2 Charged Particle Multiplicity. Big Tubes.

"*Truth is ever to be found in the simplicity,*
and not in the multiplicity ..."
/Sir Isaac Newton/

The final charged particle multiplicity distribution for the Big Tubes is extracted by taking the results of **Sec. 5.3.2**, shown in **Fig. 5.17**, scaling them with the background correction constants, defined by **Eq. (6.1)** and extracted from

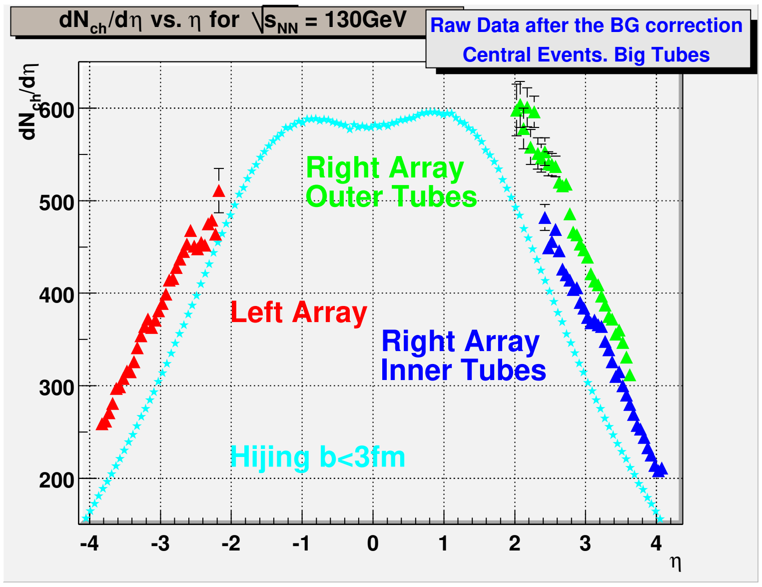

Figure 6.4: $dN_{ch}/d\eta$ *vs.* η after the background subtraction.

Fig. 6.3.

Fig. 6.4 shows the charged particle multiplicity distribution for the central events after the background subtraction for three different sets of Big Tubes.

The next step was to average the distributions from the different sets of tubes in order to come up with a final distribution. Weighted averaging was done as described in **Appendix D** over the three sets of Big Tubes shown in **Fig. 6.4**. This weighted average was mirror reflected on both sides of the pseudorapidity. Three centrality cuts were used as described before.

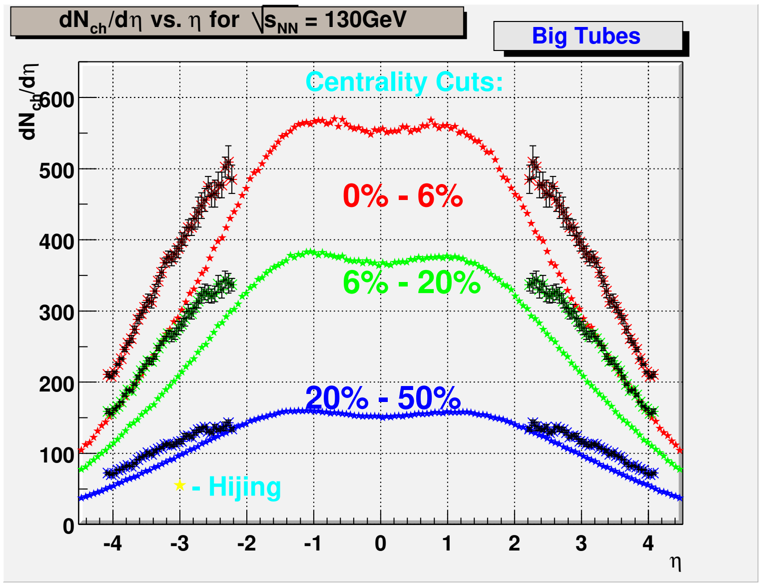

Figure 6.5: $dN_{ch}/d\eta$ *vs.* η. Big tubes.

Fig. 6.5 *shows the final charged particle multiplicity distribution, as measured by the Beam-Beam Counters Big Tubes for three different collision centrality cuts.*

Scale by the number of participants.

Another interesting result could be extracted from the multiplicity information. The graph can be scaled by the number of the charged particles participating in the collision of the two nuclei. "*Participant-spectator model*", described in **Sec. 2.1.2** can determine number of the nucleons participating in the collision of two gold nuclei with the specific centrality, or impact parameter b. **Table 6.1** presents this dependence.

Centrality Percentage	Number of Participants
0% – 6%	334
6% – 20%	239
20% – 50%	106

Table 6.1: Number of the participants for different centrality cuts. 0% corresponds to the most central collision event of $b = 0fm$.

Thus, the charged particle multiplicity distribution can be scaled with the half number of the participants in order to demonstrate the pseudorapidity distribution of the number of created charged particles per number of nucleons participating in the collision. This distribution is shown on **Fig. 6.6**. The results for different cen-

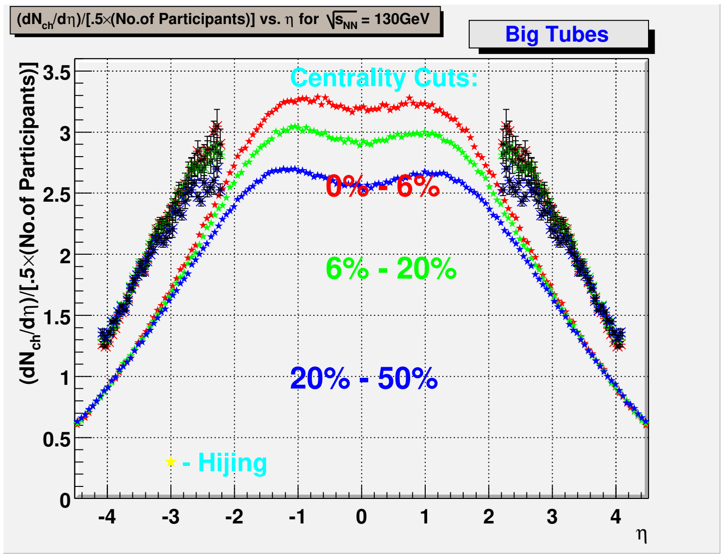

Figure 6.6: The charged particle multiplicity distribution, scaled by the half number of the participants. Big tubes.

trality cuts agree nicely with each other, showing that average number of produced particles per participant pair does not depend on the centrality of the collision, at least in this larger pseudorapidity range.

6.3 Charged Particle Multiplicity. Small Tubes.

Slightly different approaches were used to extract multiplicity information from the Small Tubes due to the saturation effect, as described in **Sec. 4.2.4**. Two of these approaches are presented here.

6.3.1 Using number of "No hits".

Some part of the Small Tubes spectrum can not be affected by the saturation, namely: a number of "*No hits* ":

No hits : A number of events in a phototube, among the collision events, when no particle was registered as a hit.

This can be described as no signal registered by the ADC unit. A set of Small Tubes located very far away from the beam-pipe was used for this purpose. In a theory of High Energy Heavy Ion collisions the average measured particle hit distribution in a phototube may be assumed to be Poisson, as in

$$P(n) = \frac{\lambda^n e^{-\lambda}}{n!}, \tag{6.2}$$

where n is number of incoming particles and λ is a mean of a distribution, or average number of MIPs in our case. The particle distribution may be approximated by the

Poisson distribution if we assume, that:

- We have rare occurrences of the large body of events.
- These events are uncorrelated.
- We are dealing with the small solid angle, *etc...*

If we do that, then the number of "*No hits* " tells us the number of entries for $n = 0$ and, assuming that charged particles are uniformly distributed between the phototubes, one can extract λ just as

$$\frac{\#\ of\ No\ hits}{Total\ Number\ of\ Events} = e^{-\lambda}, [45].$$

This method was successfully used by the PHOBOS collaboration for the charged particle multiplicity extraction [30].

A uniform particles distribution was achieved by considering very narrow vertex cuts. **Fig. 6.7** shows an actual ADC spectrum for one of the Small Tubes with obvious saturation and a big number of "*No hits* " in the zero's bin, and reconstructed Poisson distribution, based on the method described above.

Based on the average number of MIPs extracted from this approach, a regular analysis was performed, as described in **Sec. 5.3.2** by doing the acceptance correction and the background subtraction. The background corrections were taken from the GEANT simulations, as described in **Sec. 5.3.2**. $dN/d\eta$ distributions were produced. Five different sets of Small Tubes were used. **Fig. 6.8** shows charged

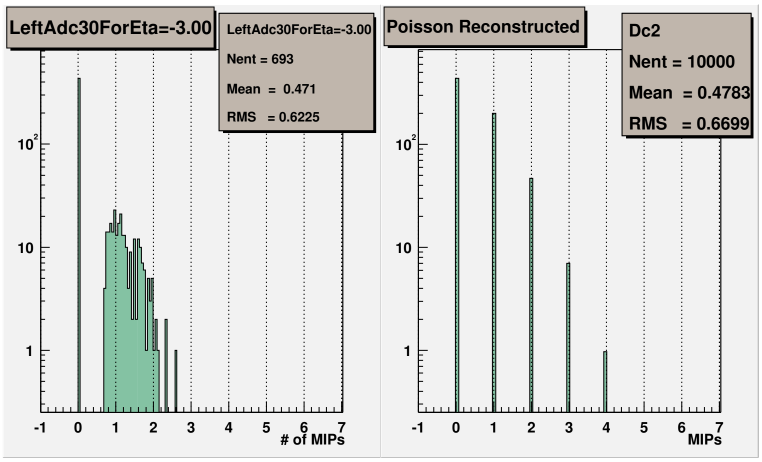

Figure 6.7: Actual ADC spectrum *vs.* Poisson distribution. Small Tube.

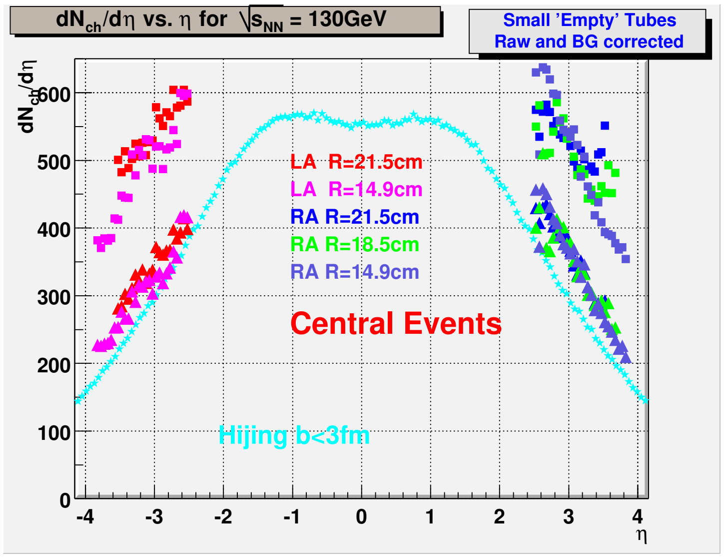

Figure 6.8: Charged particle multiplicity extracted through the "*Empty Boxes*" analysis for 5 sets of Small Tubes. Central Events. Raw and background corrected data.

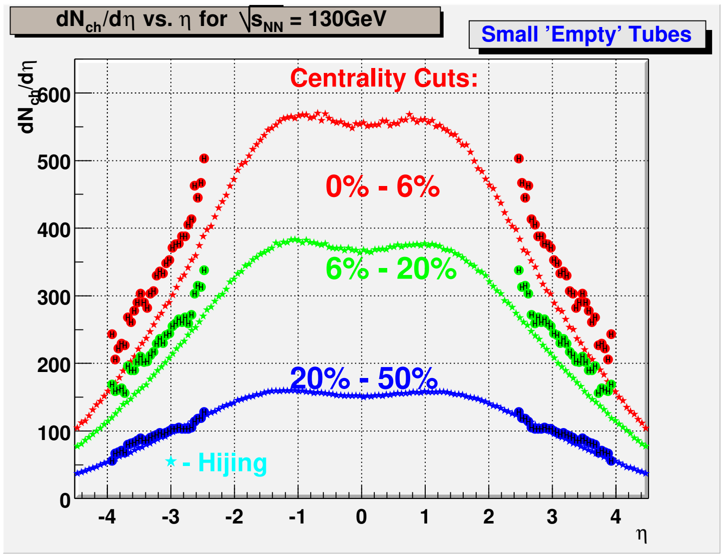

Figure 6.9: Charged particle multiplicity extracted through the "*Empty Boxes*" analysis for Small Tubes for 3 different centrality cuts.

particle multiplicity distribution in 5 sets of Small Tubes from the raw ADC spectrum and after the background corrections. **Fig. 6.9** shows the final averaged result for the central collision events from the Small Tubes. This result is in very good agreement with results for central collisions extracted from the Big Tubes and shown in **Fig. 6.5**.

6.3.2 Using "Nonlinearity correction" function.

A saturation or nonlinearity function was constructed based on the studies described in **Sec. 4.2.4**. The following steps were made:

- **Fig. 4.23** was used for these purposes with the regime of $1700V$ applied to the Small Tube.

- The pulse height corresponding to 1MIP in the linear tube was derived, using the real data ADC distribution from the Small tube and the fact that 1MIP responses should be identical in both tubes, and that 2MIP response in a linear tube must correspond to a 1.5 x 1MIP response in our Small Tube, as suggested by **Sec. 4.2.4**.

- A nonlinearity correction function $F(n)$ was derived from **Fig. 4.23** and using the item above to correct the raw data signal from the n-particle hit into the new number of hits $\hat{n}$ as

$$\hat{n} = n \cdot F(n)$$

and in **Fig. 6.10**.

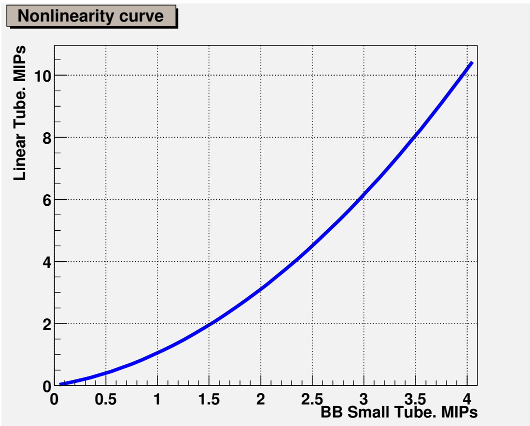

Figure 6.10: Small Tubes nonlinearity correction curve.

- An inverse function $F^{-1}(n)$ was generated to study its influence on the perfect distribution from the GEANT simulation and compare

$$\hat{n} = n \cdot F^{-1}(n)$$

distribution with the raw data.

- These functions were used to perform, so called, "*folding*" and "*unfolding*" by applying them to the GEANT and raw data ADC spectra respectively, in order to check the validity of this approach. **Fig. 6.11** shows how nicely

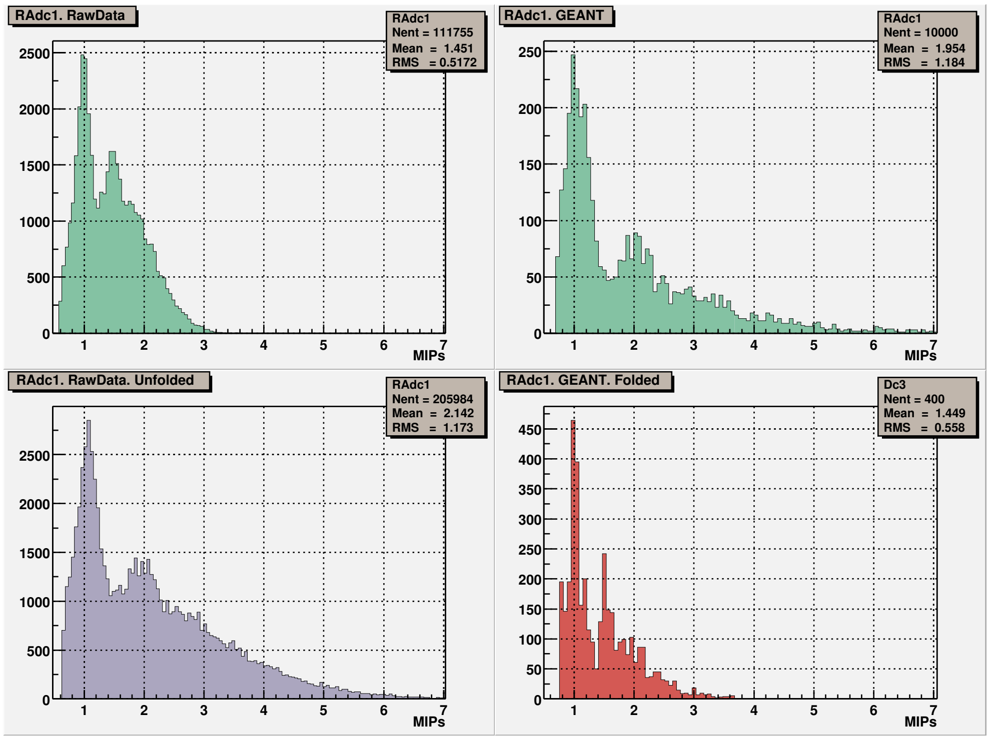

Figure 6.11: Small Tubes nonlinearity correction curve.

it worked. The "folded" GEANT spectrum looks similar to the raw data one, and the "unfolded" raw data ADC spectrum resembles the true ADC spectrum form the GEANT simulation. This allowed us to use the nonlinearity correction function in the charged particle multiplicity analysis for the Small Tubes located close to the beam pipe. They experienced the biggest saturation because of the high event rates at smaller θ angles.

And finally, $dN_{ch}/d\eta$ *vs.* η dependence was generated using the corrected number of particles in the Small Tubes and all the analysis steps described above for the Big Tubes. **Fig. 6.12** shows the raw and the background corrected charged particle multiplicity distribution extracted from the three sets of the Small Tubes using the nonlinearity correction function for the most central collision events. **Fig. 6.13** shows the final charged particle multiplicity distribution for the three centrality

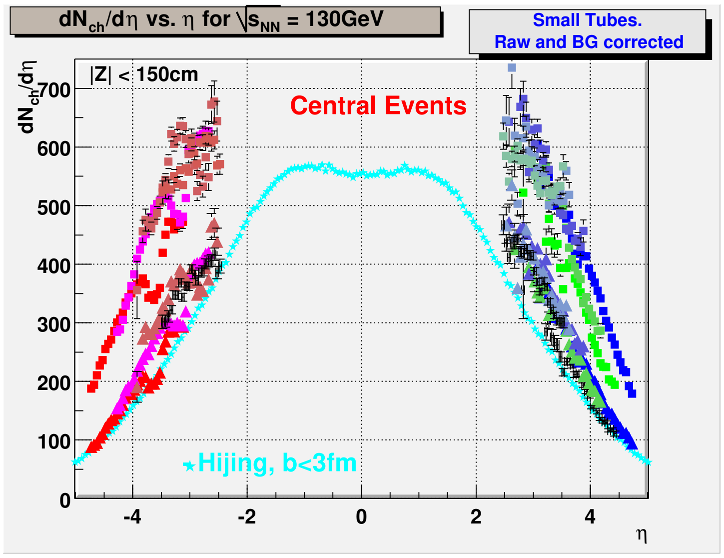

Figure 6.12: $dN_{ch}/d\eta$ *vs.* η distribution for different sets of the Small Tubes. Central Events. Raw and background corrected data.

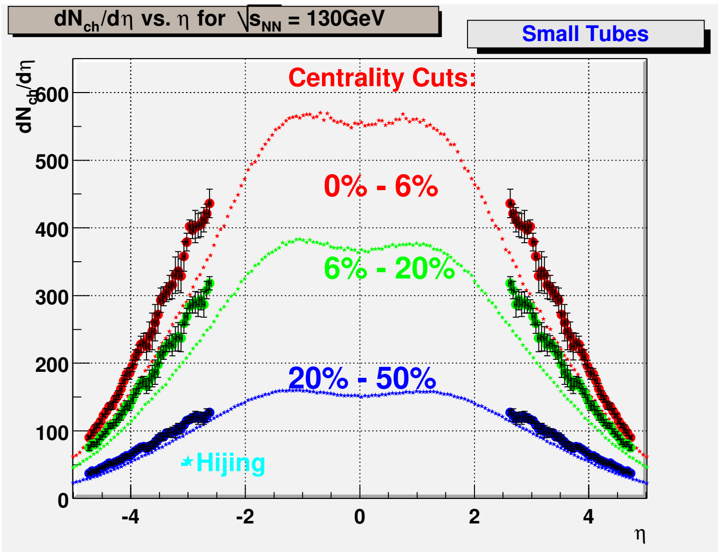

Figure 6.13: $dN_{ch}/d\eta$ *vs.* η distribution for the different centrality cuts. Small Tubes after the nonlinearity correction.

cuts extracted using the three different sets of the Small Tubes. This figure shows that the nonlinearity effect can be explained and corrected using the LED studies conducted in the lab. One can easily see that the charged particle multiplicity distribution, achieved through this method does, in general, agrees with the similar result from the Big Tubes presented in **Fig. 6.5**.

6.4 Errors Estimations.

Extremely important in evaluating any experimental result is the error associated with the measured quantity. Several sources of errors were estimated. Let me go over them briefly.

Systematic Error:

1. **Vertex Precision.**

   As it was shown in **Sec. 5.2.4**, the precision of the Beam-Beam Counters vertex determination as compared to TPM1, was equal to $15mm$. We took this number and using a random number generator, we repeated the regular analysis for charged particle multiplicity extraction while smearing the determined value of z_o by the Gaussian distribution with $mean = 0$ and $\sigma = 2 \cdot 15mm$. The, the error associated with this analysis was found to be $\leq 1.0\%$. Let me use $\delta\left(\frac{dN_{ch}}{d\eta}\right)$ for the error notation, then

   $$\delta\left(\frac{dN_{ch}}{d\eta}\right)_1 \simeq 1.0\%$$

2. **Poisson Distribution.**

   As was mentioned earlier, charged particles in any collision may be considered distributed according to the Poisson distribution. Some imperfections in the detector may cause the measured distribution to deviate from the real one. The error associated with such a deviation was estimated by approximating the fractional value of MIP hits with the integer numbers, as showed in **Fig. 6.14** The left panel of this figure shows a raw calibrated ADC distribution in one of the Big Tubes, while the right panel shows the same distribution after the rounding of the number of MIPs as described above. The charged particle multiplicity distribution from both methods were compared and the

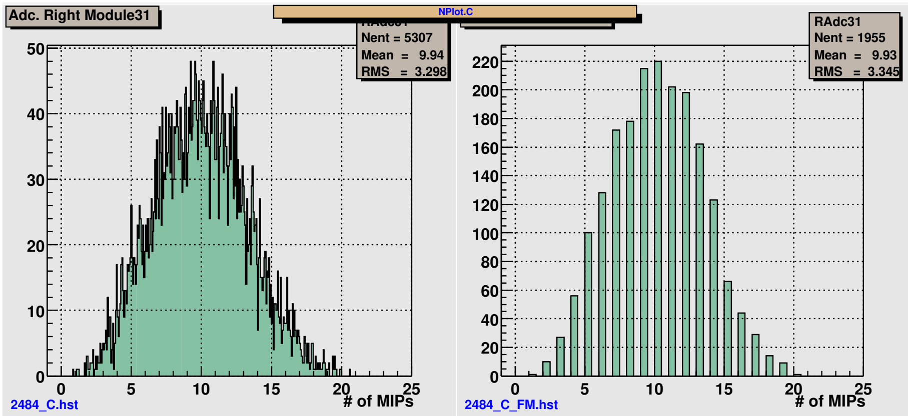

Figure 6.14: Raw distribution of charged particles hits *vs.* Poisson distribution

error associated with this source was found to be about $\leq 1.0\%$.

$$\delta\left(\frac{dN_{ch}}{d\eta}\right)_2 \simeq 1.0\%$$

3. **Direct Error Analysis.**

   Combining the formulae of **Sec. 5.3.2** one can get for the charged particle multiplicity of one event:

$$\frac{dN}{d\eta} = \frac{n \cdot RingArea}{\Delta\eta \cdot TubeArea}, \tag{6.3}$$

   where n is number of hits in one event and and let $k = RingArea/TubeArea$, then

$$\left[\delta\left(\frac{dn}{d\eta}\right)\right]^2 = \left(\frac{k}{\Delta\eta}(\delta n)\right)^2 + \left(\frac{kn}{(\Delta\eta)^2}\delta(\Delta\eta)\right)^2,$$

or just

$$\left[\frac{\delta\left(\frac{dN}{d\eta}\right)}{\frac{dN}{d\eta}}\right]^2 = \left(\frac{\delta n}{n}\right)^2 + \left[\frac{\delta(\Delta\eta)}{\Delta\eta}\right]^2$$

Now,

$$\eta = -\log\left(\tan\frac{\theta}{2}\right) \propto -log\frac{\theta}{2} \quad \Longrightarrow \delta\eta \propto \frac{\delta\theta}{\theta}$$

So, $\delta n/n$ is negligible because it has to be scaled with the number of entries factor as $1/\sqrt{Number\ of\ entries}$, and $\Delta\eta \simeq\ Const$ because of the small angle approximation, which makes $\delta(\Delta\eta) = 0$. Thus,

$$\delta\left(\frac{dN_{ch}}{d\eta}\right)_3 \simeq 0\ \%$$

4. **Individual tubes difference.**

Did differences between the responses of individual tubes contribute to the uncertainty? The same set of analysis steps was repeated for each individual tube, leading to the charged particle multiplicity distribution as determined by that tube. Then the individual $dN_{ch}/d\eta$ distributions were averaged and the result was compared to the one in **Fig. 6.5**. **Fig. 6.15** shows the distribution of the deviations in the $dN_{ch}/d\eta$ value of an individual tube in the Left Array from the averaged value. Using the numbers extracted from the comparison

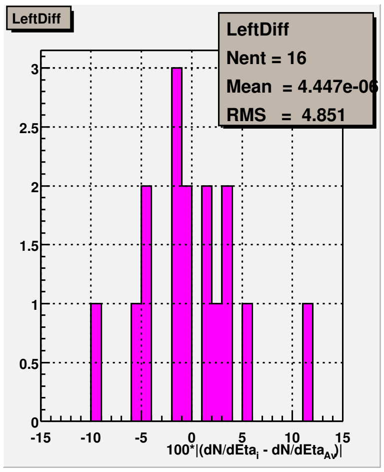

Figure 6.15: Individual tubes charged particle multiplicity distribution as compared to the averaging approach.

in the Right Array and adding them as squares, one can get

$$\delta\left(\frac{dN_{ch}}{d\eta}\right)_4 \simeq 4.9\%$$

5. **Thickness of the *Al* beampipe.**

   Another possible source of error is the thickness of the Al beampipe. As shown in **Sec. 4.1.2**, the beampipe serves as a huge source of background converting gammas into the $e^+ - e^-$ pairs. An example of the geometry of such event is shown in **Fig. 6.16**.

$$\delta\left(\frac{dN_{ch}}{d\eta}\right)_5 \simeq 2.0\%$$

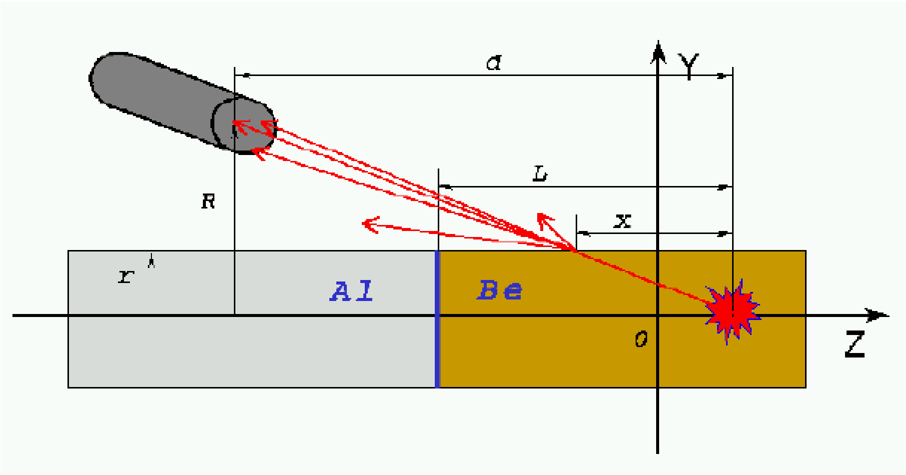

Figure 6.16: The beampipe as a source of the background.

All events which come from the vertex location $x > L$ create background. Using specification numbers for the possible variations on the Al thickness and creating a set of simulation files for the Beam-Beam Counters response to the Al beam-pipe thickness correction, we were able to get a possible error of 2% due to these variations.

6. **Centrality determination.** Our centrality cuts definitions differ by some small fraction from the nominal centrality cuts performed by the Centrality Tiles detector, as described in **Sec. 5.3.1**. That section also mentions, that the difference was found to be of the order of 1.5% for the most central events. This difference gets a bit greater for the more peripheral events, thus an average

error assigned for this kind of uncertainty is:

$$\delta\left(\frac{dN_{ch}}{d\eta}\right)_6 \simeq 2.0\%$$

7. **δ - rays.**

   Last considered was the possible contribution to the background from the δ-rays, produced in the Al beampipe. Primary ionization occurs in the material by the formation of ion pairs (positive ions and electrons) in the medium. In the first stage of this process, an incident particle produces primary ionization. Subsequently, most energetic electrons knocked out of the atoms (called δ-rays) can themselves produce fresh ions in transversing the medium [44]. This process can create much more background in the detector. The necessary modifications were made in the simulation codes and the Beam-Beam Counters response to these changes was studied again. The result was the following:

$$\delta\left(\frac{dN_{ch}}{d\eta}\right)_7 \simeq 1.0\%$$

Assuming all these errors are independent:

$$\delta\left(\frac{dN_{ch}}{d\eta}\right)_{Syst} = \sqrt{\sum_{i=1}^{7}\delta\left(\frac{dN_{ch}}{d\eta}\right)_i^2} \simeq 5.9\ \% \tag{6.4}$$

8. **GEANT**

   One more source of error was left out. Namely, the uncertainty of the GEANT approximations. It is very complicated to identify all possible uncertainties in many different parts of the GEANT code. The following questions have to be answered:

- How good does the GEANT describe our phototube' response?
- How precise is the mechanism, describing the production of the Cherenkov photons inside the lucite?
- What other possible sources of the background were not accounted for? *etc...*

It has been estimated, that these kind of uncertainties would increase our systematic error approximately to the 10% value. So,

Overall, a systematic error of ~ 10% was assigned to our measurements and has to be added to the reported charged particle multiplicity results.

Statistical Error :

As already mentioned in **Sec. 5.3.2**, the statistical error was taken from the histograms with $dN_{ch}/d\eta$ entries for a specific pseudorapidity interval as

$$\delta\left(\frac{dN_{ch}}{d\eta}\right)_{Stat} = \frac{Mean\ Value}{(RMS\ Value)\cdot\sqrt{Number\ of\ Entries}} \tag{6.5}$$

and is shown in all the histograms as vertical error bars.

Final Conclusion: *The Beam-Beam Counters not only successfully provided the BRAHMS experiment with expected timing and level0 triggering, as designed, but also served as a reliable mechanism for determining the charged particle multiplicity distribution, as was advertised in* **Ch. 1**.

CHAPTER 7
CONCLUSION

In this chapter I will try to accomplish several goals. I will

1. present final charged particle multiplicity distributions for the the pseudorapidity range of $-4.7 \leq \eta \leq 4.7$;
2. compare it with known models of the relativistic heavy-ion collisions;
3. draw a general conclusion about a possible signature of the QGP formation;
4. sum up the performance of the Beam-Beam Counters along the objectives outlined in **Sec. 1.4**.

7.1 Final Charged Particle Multiplicity.

Our final result for the charged particle multiplicity distribution will be presented in this section. It will include the final result from the Beam-Beam Counters as well as data from the other BRAHMS' detectors.

From the Beam-Beam Counters.

Three different methods were used in this thesis to determine the charged particle multiplicity distribution using the Beam-Beam Counters, as described in

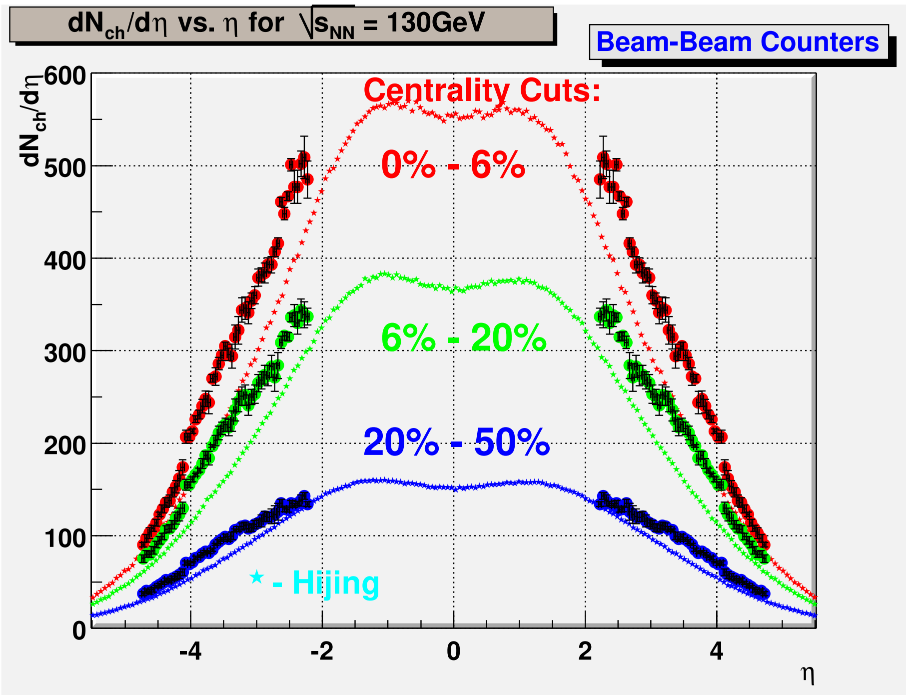

Figure 7.1: Final graph of the charged particle multiplicity distribution as measured by the BRAHMS' Beam-Beam Counters at RHIC.

Ch. 6. These methods are complementary and their results differ within the systematic error, so the results can be averaged by the "Weighted Average" technique, as described in **Appendix D**. This was done for three different centrality cuts and **Fig. 7.1** shows the resulting final charged particle multiplicity distribution in the relativistic heavy ion collisions at RHIC as measured by the BRAHMS' Beam-Beam Counters. Three centrality cuts are shown in this figure. The error bars represent the statistical errors and the overall systematic error is ~10%. All distributions are shown in comparison to the HIJING model prediction.

General picture.

Three other components of the BRAHMS experiment provide us with an independent and complimentary measurement of the charged particle multiplicity for the pseudorapidity range inaccessible to the Beam-Beam Counters. Namely, for the range of $-2.2 \leq \eta \leq 2.2$. Merged together with the results presented on **Fig. 6.5**, a complete $dN_{ch}/d\eta$ *vs.* η distribution can be shown for the entire pseudorapidity range of $-4.2 \leq \eta \leq 4.2$.

The detector systems relevant for this analysis are the Tiles Multiplicity Array, the Si Multiplicity Array and the first Time Projection Chamber (TPM1), described in **Sec. 3.2.1**. Multiplicity Tiles together with the Si Multiplicity array can provide us with the charged particle multiplicity distribution in the pseudorapidity range of $-2.2 \leq \eta \leq 2.2$, while TPM1 is capable of providing a very precise measurement of the charged particle multiplicity density in the midrapidity region of $-0.2 \leq \eta \leq 0.2$.

Fig. 7.2 shows an example of the final merged charged particle multiplicity distribution for three centrality cuts. Comparing it to the distributions provided by various models of the relativistic heavy ion collisions, discussed in **Sec. 2.2**, one can easily see that only the HIJING model predicts a distribution resembling our experimental result. This proves in general, that the HIJING model most realisticly describes such collisions. It also suggests, that in order to describe high energy heavy ion collisions a regular transport model most probably should include:

- multiple mini-jet production;
- parton shadowing;

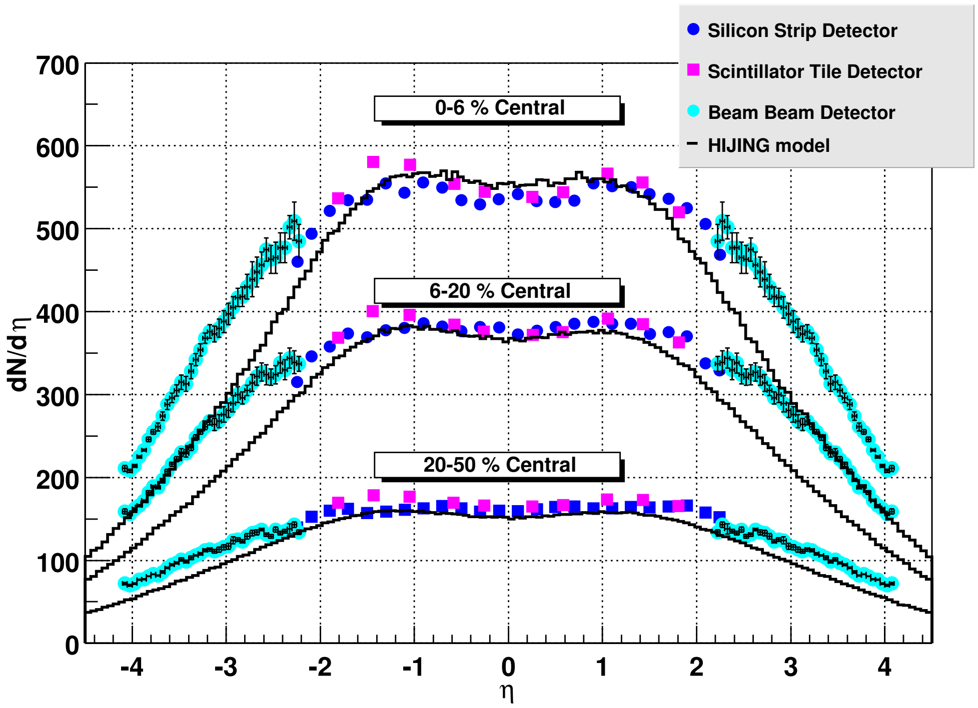

Figure 7.2: Compiled full graph of the charged particle multiplicity distribution. Three centrality cuts.

- jet quenching;
- different treatment of the first and all consecutive collisions.

Thus, one of the goals of this thesis was successfully accomplished. Namely:

> HIJING model's description of the high energy heavy-ion collision was found to be the best, among the available models, in predicting the charged particle multiplicity distribution, especially in the midrapidity range of $|\eta| \leq 1.5$.

After agreeing on the model, we have to proceed further and compare the model's predictions with our experimental results.

7.2 Research Summary

The experimental charged particle density, shown on **Fig. 7.2**, agrees with the HIJING predictions for the $dN_{ch}/d\eta$ value in the midrapidity region ($|\eta| \leq 0.2$), but differs for larger pseudorapidity values. The experimental distribution is wider than the theoretical prediction, which means, that the model underpredicts the number of charged particles, created away from the midrapidity region. As a result, the total number of particles is undepredicted as well. That may entitle us to claim that:

❶ HIJING model overpredicts the transparency of the collision and most probably the total energy deposited in the midrapidity region.

❷ The limited analysis of the global observables in the relativistic heavy-ion collisions at RHIC with the center of mass energies of $s = \sqrt{130}A\ GeV$ does not overwhelmingly suggest a clean Quark Gluon Plasma creation. Instead this may be classified as creating a state of matter, said to be in the "*Transition region*", as in transition to the QGP.

7.3 Performance Summary

In the final section of this thesis I would like to make a few last remarks on the overall Beam-Beam Counters performance in the BRAHMS experiment at RHIC.

❶ The Beam-Beam Counters served, exactly as designed, as a level0 trigger for the BRAHMS experiment, providing the best collision trigger from among the other BRAHMS detectors.

❷ The Beam-Beam Counters attained the designed precision in determining the space and time coordinates of the collision vertex position with a time resolution $\delta t \simeq 65 psec$ and vertex resolution of $\delta z \simeq 1.4 cm$.

❸ The collision instant t_o, measured by the Beam-Beam Counters was used by the BRAHMS time-of-flight detectors for particle ID purposes.

An example of such particle ID in the Midrapidity Spectrometer is shown in **Fig. 7.3**. It shows the determined time-of-flight *vs.* the particle momentum. The time-of-flight value was derived as follows:

$$time - of - flight \ = t_{TOFW} - t_o,$$

where t_{TOFW} is the converted TDC signal, registered in the Midrapidity Time-Of-Flight Wall, and t_o is the collision instant, determined by the Beam-Beam Counters. The bands in the distribution corresponds to different particle species.

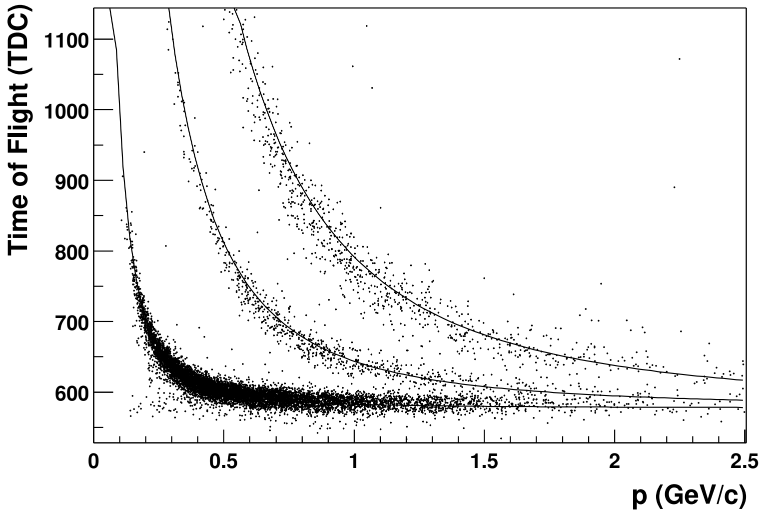

Figure 7.3: Time-of-flight *vs.* particle' momentum. BRAHMS TOFW detector.

❹ The Beam-Beam Counters successfully provided a set of unique measurements of the charged particle multiplicity distribution for different collision centrality cuts.

❺ The measured $dN_{ch}/d\eta$ distribution served as valuable input for the evaluation of the various collision models, and pinpointed the HIJING event generator as the one that most closely predicts the charged particle multiplicity distribution measured in our experiment.

"*Feci quod potui, faciant meliora potentes.*"[6]

[6] "I've done what I could, let the others to do it better!" (lat.)

APPENDIX A
PARTICLES AND FORCES

This appendix does a brief introduction to the present “zoo” of particles and forces [47].

Particles

All fundamental fermion particles (half-integer spin) can be grouped in 3 generations, as shown in **Table A.1**. The generations differ by mass. Top two rows

Generation	Flavor	Charge	mass
1	u (up)	+2/3	“few MeV
	d (down)	-1/3	“few MeV”, $m_d > m_u$
	e^-	-1	0.511 MeV
	ν_e	0	$\leq 7\ eV$
2	c (charm)	+2/3	$\simeq 0.9\ GeV$
	s (strange)	-1/3	$\simeq 0.1\ GeV$
	μ^-	-1	0.106 GeV
	ν_μ	0	$\leq 0.27\ MeV$
3	t (top)	+2/3	$\simeq 180\ GeV$
	b (bottom)	-1/3	$\simeq 5\ GeV$
	τ^-	-1	1.776 GeV
	ν_τ	0	$\leq 31\ MeV$

Table A.1: Fundamental Fermions [47].

of each generations are strongly interacting particles, called “quarks” and have a quantum number called “color”. Color comes in three varieties. Each particle has an associated anti-particle which is identical in mass with the particle, but has opposite charge and color. Bottom two raws in each generations are occupied by "leptons": e, μ, τ and their neutrinos. There are conservation laws associated with these particles:

- Sum of quarks minus anti-quarks is a conserved quantity for quarks.
- The number of leptons minus anti-leptons is conserved within each generation.

Interactions

Each interaction has a boson particle (integer spin) which "carries" the force. **Table A.2** summarizes all known interactions. Strength of the interaction is mea-

Interaction	Gravity	Electro-Magnetic	Weak	Strong
Field Quantum	Graviton	Photon	$W^{\pm}$, Z^{o} Interm. bosons	Gluon
Mass, $[GeV]$	0	0	80-90	0
Range, $[m]$	∞	∞	10^{-18}	$\leq 10^{-15}$
Source	Mass/ Energy	Electric Charge	"Weak Charge"	"Color Charge"
Cross Section, $[m^2]$	–	10^{-33}	10^{-44}	10^{-30}

Table A.2: Fundamental interactions [44].

sured by a quantity σ, called cross section. The more probable ("stronger") interaction has bigger cross section. Quarks have all four kinds of interactions. Leptons do not have the strong interactions and neutrinos do not interact electro-magnetically.

General Comments

"*Hadrons*" are strongly interacting particles built from two types of quark combination:

$$\text{Baryon} = qqq \quad \text{(three quarks)}$$

$$\text{Meson} = q\bar{q} \quad \text{(quark - antiquark pair)}$$

Examples are:

Baryons	Mesons
$uud = p$ (proton)	$u\bar{d} = \pi^+$ (pion)
$udd = n$ (neutron)	$\bar{s}d = K^o$ (kaon)
$uds = \Lambda$ (lambda hyperon)	$c\bar{c} = \psi$-meson

Conservation rule for quarks is reflected in the conservation of the "*baryon number*", where every baryon (antibaryon) is assigned a baryon number +1 (-1) [44]. This makes a quark (antiquark) have a baryon number of +1/3 (-1/3). There is no conservation rules for mesons.

The strong interaction provides a quantum glue ("*gluon*") to hold the quarks together and form hadrons. Color is a "hidden" quantum number; only colorless particles are allowed as real particles. This explains why only baryons and mesons are allowed to exist. Antiparticles have anticolors. Colors can be picked as R - red, B - blue and G - green, just to form white as: RBG or $R\bar{R}$. The gluons have to be bi-colored, $R\bar{B}$, *etc.* There eight gluons, as $3 \times 3 = 9$, minus 1 for the symmetric colorless combination. The color is conserved in the quarks and gluons interactions. These interactions are described by the Quantum Chromodynamics (QCD).

APPENDIX B

CABLING SCHEME

Actual cabling scheme for the Beam-Beam Counters is shown here. The first column has module numbers; the second one shows distance to the beam pipe. Then one can find all electronics modules used with the cable/channel numbers, and the last

RIGHT ARRAY

Module #	Dist. R, [cm]	Tube #		HV Ch. #	ADC cable	ADC Delay Cable	ADC channel in FB-4 BB		TDC -> IR Disc. Phillips 710 Ch.	TDC Cable		TDC-> FCH Disc. Phillips 710 Ch.	TDC Delay Cable		TDC->FCH Disc. LeCroy 3412 Ch.		TDC ch. in CA-1 BB Phillips	Hama-matsu KA #
SMALL TUBES																		
1	6.5	37	LeCroy4032A Mainframe M1	0	A037	AD037	48	S.N.#3032	1	T037	S.N.#2194	1	TD037	S.N. #B68863	1	S.N. #10670	1	4288
2	6.5	38		1	A038	AD038	49		2	T038		2	TD038		2		2	4618
3	6.5	39		2	A039	AD039	50		3	T039		3	TD039		3		3	5089
4	6.5	40		3	A040	AD040	51		4	T040		4	TD040		4		4	4845
5	6.5	41		4	A041	AD041	52		5	T041		5	TD041		5		5	4012
6	8.3	42		5	A042	AD042	53		6	T042		6	TD042		6		6	4944
7	8.3	43		6	A043	AD043	54		7	T043		7	TD043		7		7	3863
8	8.3	44		7	A044	AD044	55		8	T044		8	TD044		8		8	5450
9	8.3	45		8	A045	AD045	56	S.N.#1850	1	T045	S.N.#2233	1	TD045		9		9	4677
10	10.6	46		9	A046	AD046	57		2	T046		2	TD046		10		10	5085
11	10.6	47		10	A047	AD047	58		3	T047		3	TD047		11		11	5379
12	14.9	48		11	A048	AD048	59		4	T048		4	TD048		12		12	5664
13	14.9	49		12	A049	AD049	60		5	T049		5	TD049		13		13	5454
14	14.9	50		13	A050	AD050	61		6	T050		6	TD050		14		14	4023
15	14.9	51		14	A051	AD051	62		7	T051		7	TD051		15		15	4365
16	18.5	52		15	A052	AD052	63		8	T052		8	TD052		16		16	3811
17	18.5	53		16	A053	AD053	64	S.N.#2231	1	T053	S.N.#2144	1	TD053	S.N. #B68863	1	S.N. #10671	1	5051
18	18.5	54		17	A054	AD054	65		2	T054		2	TD054		2		2	5342
19	18.5	55		18	A055	AD055	66		3	T055		3	TD055		3		3	5439
20	21.5	56		19	A056	AD056	67		4	T056		4	TD056		4		4	3728
21	21.5	57		20	A057	AD057	68		5	T057		5	TD057		5		5	4206
22	21.5	58		21	A058	AD058	69		6	T058		6	TD058		6		6	5301
23	21.5	59		22	A059	AD059	70		7	T059		7	TD059		7		7	2578
24	21.5	60		23	A060	AD060	71		8	T060		8	TD060		8		8	5383
25	21.5	61		24	A061	AD061	72	S.N.#2230	1	T061	S.N.#2190	1	TD061		9		9	5029
26	21.5	62		25	A062	AD062	73		2	T062		2	TD062		10		10	5060
27	21.5	63		26	A063	AD063	74		3	T063		3	TD063		11		11	5636
28	21.5	64		27	A064	AD064	75		4	T064		4	TD064		12		12	5352
29	21.5	65		28	A065	AD065	76		5	T065		5	TD065		13		13	5580
30	21.5	66		29	A066	AD066	77		6	T066		6	TD066		14		14	5762
BIG TUBES																		
31	12.6	78	M3	8	A078	AD078	80	S.N.#2185	1	T078	S.N.#2183	1	TD078	S.N.#B6888	1	S.N.#13232	1	1952
32	12.6	79		9	A079	AD079	81		2	T079		2	TD079		2		2	4188
33	12.6	80		10	A080	AD080	82		3	T080		3	TD080		3		3	4167
34	19.8	81		11	A081	AD081	83		4	T081		4	TD081		4		4	720
35	19.8	82		12	A082	AD082	84		5	T082		5	TD082		5		5	4162

Figure B.1: Right Array Cabling.

LEFT ARRAY

Module #	Dist. R, [cm]	Tube #		HV, Ch. #	ADC cable	ADC Delay Cable	ADC channel in FB-4 BB		TDC->IR Disc. Phillips 710 Ch.	TDC Cable		TDC->FEH Disc. Phillips 710 Ch.	TDC Delay Cable		TDC->FEH Disc. LeCroy 3412 Ch.		TDC ch. in CA-1 BB Phillips71	Hama-matsu KA #
SMALL TUBES																		
1	6.5	1	LeCroy4032A Mainframe M2	0	A001	AD001	0	S.N. #3025	1	T001	S.N. 2229	1	TD001	S.N. #B68879	1	S.N. #[illegible]	1	3939
2	6.5	2		1	A002	AD002	1		2	T002		2	TD002		2		2	4607
3	6.5	3		2	A003	AD003	2		3	T003		3	TD003		3		3	4163
4	6.5	4		3	A004	AD004	3		4	T004		4	TD004		4		4	5299
5	6.5	5		4	A005	AD005	4		5	T005		5	TD005		5		5	3944
6	6.5	6		5	A006	AD006	5		6	T006		6	TD006		6		6	3761
7	6.5	7		6	A007	AD007	6		7	T007		7	TD007		7		7	4214
8	6.5	8		7	A008	AD008	7		8	T008		8	TD008		8		8	4844
9	10	9		8	A009	AD009	8	S.N.#3030	1	T009	S.N. 2197	1	TD009		9		9	5097
10	10	10		9	A010	AD010	9		2	T010		2	TD010		10		10	3955
11	10	11		9	A011	AD011	10		3	T011		3	TD011		11		11	4029
12	10	12		10	A012	AD012	11		4	T012		4	TD012		12		12	4872
13	10	13		11	A013	AD013	12		5	T013		5	TD013		13		13	3915
14	10	14		11	A014	AD014	13		6	T014		6	TD014		14		14	3741
15	10	15		12	A015	AD015	14		7	T015		7	TD015		15		15	3803
16	10	16		13	A016	AD016	15		8	T016		8	TD016		16		16	4953
17	10	17		13	A017	AD017	16	S.N.#2223	1	T017	S.N. 2187	1	TD017	S.N. #B68879	1	S.N. #[illegible]	1	5274
18	10	18		14	A018	AD018	17		2	T018		2	TD018		2		2	5188
19	10	19		15	A019	AD019	18		3	T019		3	TD019		3		3	5732
20	10	20		15	A020	AD020	19		4	T020		4	TD020		4		4	5494
21	10	21		16	A021	AD021	20		5	T021		5	TD021		5		5	4392
22	10	22		17	A022	AD022	21		6	T022		6	TD022		6		6	5631
23	10	23		18	A023	AD023	22		7	T023		7	TD023		7		7	4623
24	10	24		19	A024	AD024	23		8	T024		8	TD024		8		8	4905
25	14.9	25		20	A025	AD025	24	S.N.#2145	1	T025	S.N. 2186	1	TD025		9		9	3872
26	14.9	26		21	A026	AD026	25		2	T026		2	TD026		10		10	4837
27	14.9	27		22	A027	AD027	26		3	T027		3	TD027		11		11	5381
28	14.9	28		23	A028	AD028	27		4	T028		4	TD028		12		12	5312
29	21.5	29		24	A029	AD029	28		5	T029		5	TD029		13		13	5596
30	21.5	30		25	A030	AD030	29		6	T030		6	TD030		14		14	5313
31	21.5	31		26	A031	AD031	30		7	T031		7	TD031		15		15	5530
32	21.5	32		27	A032	AD032	31		8	T032		8	TD032		16		16	5316
33	21.5	33		28	A033	AD033	32	S.N. #2145	1	T033	S.N. #2224	1	TD033	S.N.#[illegible]	1	S.N.#[illegible]	1	5550
34	21.5	34		29	A034	AD034	33		2	T034		2	TD034		2		2	3834
35	21.5	35		30	A035	AD035	34		3	T035		3	TD035		3		3	4969
36	21.5	36		31	A036	AD036	35		4	T036		4	TD036		4		4	4047
BIG TUBES																		
37	16	70	16	0	A070	AD070	40	S.N.#2146	1	T070	S.N.#2189	1	TD070	S.N.#B68879	9	S.N.#12203	9	840
38	16	71		1	A071	AD071	41		2	T071		2	TD071		10		10	4198
39	16	72		2	A072	AD072	42		3	T072		3	TD072		11		11	4196
40	16	73		3	A073	AD073	43		4	T073		4	TD073		12		12	4161
41	16	74		4	A074	AD074	44		5	T074		5	TD074		13		13	1084
42	16	75		5	A075	AD075	45		6	T075		6	TD075		14		14	4166
43	16	76		6	A076	AD076	46		7	T076		7	TD076		15		15	4197
44	16	77		7	A077	AD077	47		8	T077		8	TD077		16		16	4195

Figure B.2: Left Array Cabling.

column shows the actual tube numbers from the Hamamatsu catalog.

APPENDIX C

TDC CALIBRATION

TDC's were calibrated against a known time interval using the Ortec 662 Time Calibrator. This kind of a calibrator produces $START$ and $STOP$ signal with a very precise interval between them [42].

$$STOP = START + n * STEP,$$

where n ranges number between 1 and m, $m = RANGE/STEP$.

Calibration constants were found to be very consistent. **Figure C.1** shows the

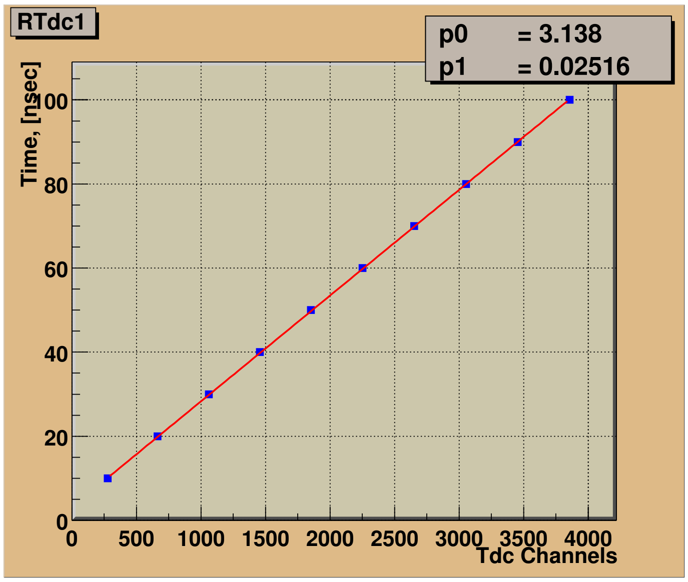

Figure C.1: TDC channel *vs.* time for one of the Beam-Beam Counters channels

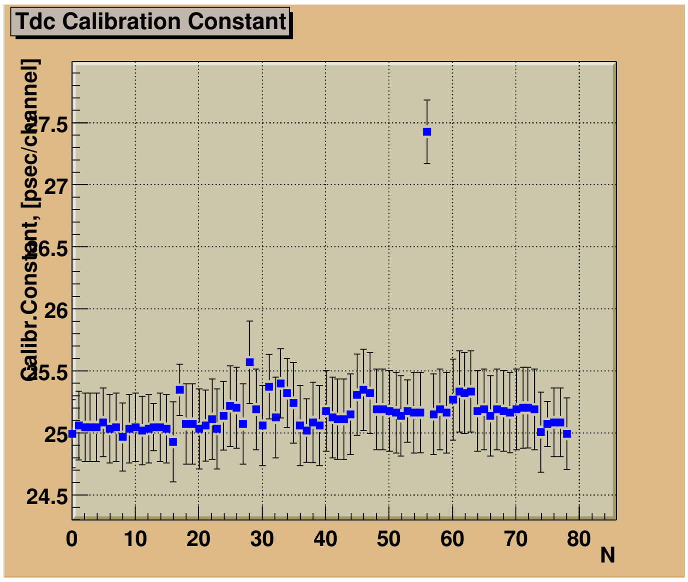

Figure C.2: TDC calibration constants *vs.* channel for the Beam-Beam Counters TDC channels

position of the TDC peaks versus time for one channel of the Beam-Beam Counters. The fit is to a first order polynomial.

Figure C.2 summarizes the results for the Beam-Beam Counters, showing calibration constants for every module.

APPENDIX D
AVERAGING

To do the average we use a standard approach of weighted least squares supplemented with an increase in the statistical error of the averaged result by a "scale" factor, as discussed in the "Particle Data Book" [46]. For noncorrelated measurements the weighted average and it's error are calculated as:

$$\bar{x} \pm \delta\bar{x} = \frac{\sum_i w_i x_i}{\sum_i w_i} \pm \left(\sum_i w_i \right)^{-1/2}, \tag{D.1}$$

where

$$w_i = 1/\left(\delta x_i\right)^2 .$$

Here, in our case, x_i and δx_i are the $dN_{ch}/d\eta$ and it's error values for $N = 3$ different sets of tubes. Then $\chi^2 = \sum w_i(\bar{x} - x_i)^2$ is calculated and compared with $N - 1$, as an expectation value for χ^2, since our measurements are Gaussian distributed. Results are accepted if $\chi^2/(N-1) \leq 1$. If $\chi^2/(N-1)$ is not much greater than 1, then the error from **Eq. (D.1)** is increased by a scale factor S, where:

$$S = \sqrt{\chi^2/(N-1)} \tag{D.2}$$

The reasoning is, that if χ^2 is too big, it means that we are underestimating some of our errors. Without knowing which error is beign underestimated, all of them are assumed to be underestimated by the same scale factor S.

APPENDIX E

BRAHMS COLLABORATION

I. G. Bearden[8], D. Beavis[1], Y. Blyakhman [7], J. Brzychczyk[5], B. Budick[7], H. Bøggild[8], C. Chasman[1], P. Christiansen[8], J. Cibor[3], R. Debbe[1], J. J. Gaardhøje[8], K. Grotowski[5], J. I. Jordre[10], F. Jundt[4], K. Hagel[9], O. Hansen[8], A. Holm[8], C. Holm[8], A. K. Holme[2], H. Ito[12], E. Jacobsen[8], A. Jipa[11], C. E. Jørgensen[8], E. J. Kim[6], T. Kozic[5], T. Keutgen[9], T. M. Larsen[2], J. H. Lee[1], Y. K. Lee[6], G. Løvhoiden[2], Z. Majka[5], A. Makeev[9], B. McBreen[1], M. Murray[9], J. Natowitz[9], B. S. Nielsen[8], K. Olchanski[1], D. Ouerdane[8], J. Olness[1], R. Planeta[5], F. Rami[4], D. Roehrich[10], B. Samset[2], S. Sanders[12], R. A. Sheetz[1], Z. Sosin[11], P. Staczel[8], T. F. Thorsteinsen[10+], T. S. Tveter[2], F. Videbæk[1], R. Wada[9], A. Wieloch[5], and I. S. Zgura[11].

[1] Brookhaven National Laboratory, Upton, NY, USA
[2] Fysisk Institutt, University of Oslo, Blindern, Norway
[3] Institute of Nuclear Physics, Krakow, Poland
[4] IReS, University Louis Pasteur, Strasbourg, France
[5] Jagiellonian University, Krakow, Poland
[6] John Hopkins University, Baltimore, MD, USA
[7] New York University, New York, NY, USA
[8] Niels Bohr Institute, University of Copenhagen, Copenhagen, Denmark
[9] Texas A&M University, College Station, TX, USA
[10] University of Bergen, Norway
[11] University of Bucharest, Romania
[12] University of Kansas, KS, USA
[+] *Deceased*

BIBLIOGRAPHY

[1] L. Van Hove, in Nucl. Phys. **A461**, 3C (1987).

[2] L.P.Csernai, *Introduction to Relativistic Heavy Ion Colisions*, John Wiley & Sons, 1994.

[3] J. B. Kogut, Nucl. Phys. **A461** (1987) 327C;
A.Ukawa, Nucl. Phys. **A498** (1989) 227C;
B.Petersson, Nucl. Phys. **A525** (1991) 237C;
T.Hatsuda, Nucl. Phys. **A544** (1992) 27C.

[4] Committee on Nuclear Physics. National Research Council, *Nuclear Physics. The Core of Matter. The Fuel of Stars*, National Academy press, 1999.

[5] C.-Y. Wong, *Introduction to High-Energy Heavy-Ion Collisions*, World Scientific, 1994.

[6] E.Segré, *Nuclei and Particles*, Addison-Wesley, 1982.

[7] D.Beavis *et. al.* [BRAHMS Collaboration], *Conceptual Design Report for BRAHMS*, BNL-62018. Available as a computer version at http://www.rhic.bnl.gov/brahms/WWW/cdr/cdr.html

[8] K. Alpgard *et al.* [UA5 Collaboration], Phys. Lett. **B107**, 315 (1981).
K. Alpgard *et al.* [Scandinavian Bubble Chamber Collaboration], Nucl. Phys. **B105**, 349 (1976).

[9] M. Gyulassy, Nucl. Phys. **A590** (1995) 431C [nucl-th/9503024]
after T.D.Lee, Quark Matter 95 proceedings.

[10] B. B. Back *et al.* [PHOBOS Collaboration], Phys. Rev. Lett. **85**, 3100 (2000) [hep-ex/0007036].

[11] K. H. Ackermann *et al.* [STAR Collaboration], [nucl-ex/0009011].

[12] K. Adcox *et al.* [PHENIX Collaboration], [nucl-ex/0012008].

[13] J. W. Harris and B. Muller, Ann. Rev. Nucl. Part. Sci. **46**, 71 (1996) [hep-ph/9602235].

[14] J. C. Collins and M. J. Perry, Phys. Rev. Lett. **34**, 1353 (1975).

[15] A. Chodos, R. L. Jaffe, K. Johnson, C. B. Thorn and V. F. Weisskopf, Phys. Rev. **D9**, 3471 (1974).

[16] K. Geiger, *In *Hwa, R.C. (ed.): Quark-gluon plasma, vol.2* 264-323.*

[17] J.D.Bjorken, Phys. Rev. **D27** (1983) 140.

[18] L. Van Hove, Phys. Lett. B **118** (1982) 138.

[19] L. D. Landau, Izv. Akad. Nauk SSSR Ser. Fiz. 17 (1953) 51;
Collected papaers, ed. D. Ter Haar (Pergamon, Oxford, 1965) p.569.

[20] K. Werner, [hep-ph/0009153].

[21] K. J. Eskola, in Nucl. Phys. **A590**, 383C (1995) [hep-ph/9503254].

[22] X. Wang and M. Gyulassy, Phys. Rev. **D44**, 3501 (1991).

[23] B. Andersson, G. Gustafson and B. Nilsson-Almqvist, Nucl. Phys. **B281**, 289 (1987).

[24] B. Nilsson-Almqvist and E. Stenlund, Comput. Phys. Commun. **43**, 387 (1987).

[25] H. Pi, Comput. Phys. Commun. **71** (1992) 173.

[26] M. Gyulassy and X. Wang, Comput. Phys. Commun. **83**, 307 (1994) [nucl-th/9502021].

[27] BRAHMS private communications with X.N.Wang.

[28] H. Sorge, Phys. Rev. **C52**, 3291 (1995) [nucl-th/9509007].

[29] S. A. Bass *et al.*, Prog. Part. Nucl. Phys. **41**, 225 (1998) [nucl-th/9803035].

[30] A.Wuosmaa for the PHOBOS Collaboration, $dN_{ch}/d\eta$ *from PHOBOS*, talk given at "Quark Matter 2001" conference. (January, 2001).

[31] A. Denisov for the PHENIX Collaboration, *Common Event Characterization in the RHIC Experiments*, talk given at "Quark Matter 2001" conference. (January, 2001).

[32] RHIC Design Manual. Available as a computer version at http://www.agsrhichome.bnl.gov/NT-share/rhicdm/index.html

[33] R.K.Bock, H.Grote, D.Notz, M.Regler, *Data analysis techniques for high-energy physics experiments*, Cambridge University Press, 1990.

[34] I.G.Bearden *et. al.* [BRAHMS collaboration], *The BRAHMS experiment at RHIC*, Nuclear Instruments and Methods. To be published.

[35] M.Murray, *Zero Degree Calorimetry for BRAHMS*, proposal, 1998.

[36] Grupen, C., *Particle Detectors*, Cambridge University Press, 1996.

[37] Jackson, J.D., *Classical Electrodynamics*, 2nd ed., Wiley, New York, 1975.

[38] *Photomultiplier Tubes and Assemblies*, Cat. No. TPMO0001E03, Hamamatsu Photonics K.K., 1994.

[39] Delaney, C.F.G. and Finch, E.G., *Radiation Detectors*, Clarendon Press, Oxford, 1992.

[40] Constant Fraction Discriminator Manual.

[41] Brookhaven National Laboratory Bulletin, **Vol. 54**. No 22 (June 23, 2000).Available as a computer version at http://www.pubaf.bnl.gov/bulletin/bb062300.pdf

[42] Y.Blyakhman, E.Jacobsen, A.Makeev, M.Murray, *TDC Calibrations*, BRAHMS Analysis Note, 1998.

[43] GEANT - Detector Description and Simulation Tool, Available as a computer version at
http://wwwinfo.cern.ch/asd/geant/

[44] D.H.Perkins, *Introduction ot High Energy Physics*, Addison-Wesley, 1987.

[45] C.Chasman, Private communications.

[46] D.E. Groom *et al*, The European Physical Journal **C15** (2000) 1, Available as a computer version at the PDG WWW pages:
http://pdg.lbl.gov/

[47] B.P.Roe, *Particle Physics at the New Millenium*, Springer, 1996.